TISSUE FORMATION AND REMODELING IN TISSUE ENGINEERED PULMONARY CONDUITS

by

Chad Edward Eckert

B.S. in Materials Science & Engineering, University of Pittsburgh, 2005

Submitted to the Graduate Faculty of

The Swanson School of Engineering in partial fulfillment

of the requirements for the degree of

Doctor of Philosophy

University of Pittsburgh

2011

UNIVERSITY OF PITTSBURGH

SWANSON SCHOOL OF ENGINEERING

This dissertation was presented

by

Chad Edward Eckert

It was defended on

May 10, 2011

and approved by

William R. Wagner, PhD, Professor, Department of Surgery

Anne M. Robertson, PhD, Associate Professor,

Department of Mechanical Engineering and Materials Science

Kacey G. Marra, PhD, Associate Professor, Department of Surgery

Frederick J. Schoen, MD, PhD, Professor, Department of Pathology, Brigham and Women's Hospital

John E. Mayer Jr., Professor, Department of Cardiology and Cardiovascular Surgery,

Children's Hospital Boston

Dissertation Director: Michael S. Sacks, PhD, John A. Swanson Endowed Chair in Bioengineering,

Department of Bioengineering, CEE, and MEMS

TISSUE FORMATION AND REMODELING IN TISSUE ENGINEERED PULMONARY CONDUITS

Chad Edward Eckert, PhD

University of Pittsburgh, 2011

Over the past decade, the tissue engineering paradigm has gained attention as a potential means to restore native tissue functionality. Although attractive, the wide variety of scaffold materials, cell sources, and mechanical conditioning regimes coupled with the paucity of structurally-based, finite deformation framework constitutive models found in the literature hinders the elucidation of extracellular matrix (ECM) formation and remodeling in engineered tissues. Therefore, the overall objective of this work is to develop structurally guided generalized finite deformation based constitutive models than can be used to gain an understanding of tissue formation and remodeling in tissue engineering applications. Further, it is the intent of this work to apply such an approach to investigate tissue formation and remodeling in tissue engineered pulmonary arteries.

In the first part of this work, a novel technique for acquiring and quantifying high resolution three dimensional structural data was used on bone-marrow stem cell-seeded polymeric scaffold composites, and it was shown that the continuous anisotropic scaffold phase transitioned to a highly discontinuous isotropic scaffold phase after twelve weeks in vivo. Next, structural constitutive models were developed based on the scaffold continuity. For continuous scaffold composites, scaffold-ECM interactions were included in the model as extensional and shearing terms, while it was shown that such effects were negligible in the discontinuous scaffold composites. A parameter estimation and model validation procedure was described using a tunable tissue-analog system of polyacrylamide (PAM) gel. It was found that the scaffold-ECM interaction due to fiber extension was highly non-linear, showing a reinforcing effect larger than from rule of mixtures predictions. Experimental validation with PAM gel supported the models. Finally, both models were used to investigate tissue formation and remodeling in in vivo engineered pulmonary arteries. At early timepoints (7 days), little change in ECM mechanical properties was observed. In later timepoints (42 to 140 days), the collagen effective modulus and collagen recruitment parameters changed substantially, suggesting collagen maturation via increased cross-linking and crimp organization. Ultimately, a methodical approach to understanding tissue formation and remodeling via structural constitutive models was presented and successfully applied to a clinically-relevant tissue engineering system.

TABLE OF CONTENTS

LIST OF TABLES

LIST OF FIGURES

PREFACE

Too often, I find myself focusing on an endpoint rather than the journey to an endpoint (a "state function" philosophy, to borrow from thermodynamics). Although this may be advantageous in some circumstances (it is a relief knowing the finish line is nearing during mile 25 of a marathon), I realize it may cheapen life's experiences by reducing lengths of time to a series of singular events. As I finish this chapter culminating six years of work, my wish is to reflect upon the journey and not the end. I have had some amazing experiences, and I have met some remarkable people during my studies. I have been blessed with opportunities to travel throughout the country and around the world, even living in another hemisphere for three months. I have been challenged beyond what I thought possible, but I have been supported and encouraged in unimaginable ways. I forged new lifetime relationships, deepened close friendships, and I met my best friend, my wife. I got to do some pretty neat research as well.

In an attempt to express gratitude towards each person who has had an impact on me, I could write a second volume to my dissertation that would in length rival some of Dickens' works. I borrow from Cicero, however, a relevant quote: "brevity is a great charm of eloquence." As such, I will try to balance the two.

Without Dr. Borovetz and Dr. Sacks, my journey would not have continued at the University of Pittsburgh. The former encouraged me to remain at Pitt, always greeting me with running tales ("I bet '_____' was out running at 5am in this weather…"), a firm handshake, and a warm smile. The latter, my adviser, opened a multitude of doors. I am thankful for Dr. Sacks' willingness to permit unfettered study, providing advice only when most needed. I was given the chance to explore a variety of topics, and I was given freedom in approaching problems. My research aptitude and salesmanship were strengthened under his guidance.

Working with other labs was essential to my work. I am appreciative of the support from Dr. Ian LeGrice and Dr. Bruce Smaill in Auckland, from Dr. Robert Padera, Dr. Frederick Schoen, and Dr. John Mayer in Boston, and Dr. Joe Gorman and Dr. Rob Gorman in Philadelphia. Danielle Gottlieb provided study specimens, research ideas, and a good ear to listen. Dane Gerneke provided expert guidance with imaging work, and him and his wife Bobby provided incredibly kind hospitality while in New Zealand. They are dear friends for life.

Friendships at Pitt (both within and outside of our lab) provided sanity, humor, and advice. I am deeply thankful for the friendships of Diana Gaitan, Bahar Fata, Silvia Wognum, Todd Courtney, David Schmidt, Chris Hobson, Chris Carruthers, Kate Lewis, Gilliane McShane, Rouzbeh Amini, Daniela Valdez-Jasso, Rong Fan, Erinn Joyce, John Stella, Brandon Mikulis, and Antonio D'Amore. I especially enjoyed the frequency conversations with John regarding the controlled anaerobic conversion of select enzymatically digested complex carbohydrates to ethanol in *Saccharomyces cerevisiae*.

I am indebted to the kindness of Anna Goldman, Beth Markocic, Lynn Ekis, Karen Connor, Lynette Spataro, and Glenn Peterson – so often they provided very tangible help in scheduling meetings, figuring out paperwork, and always seeming to know the right avenues to accomplish the tasks at hand. Josh Woolley provided great distractions as well as a solid perspective, and with his experiences with the Artificial Heart Program, many, many doors have been opened for me. I am grateful for his guidance with handling some of the demands of hospital night shifts and clinical care while pursuing a PhD. I can honestly say the experiences with the Artificial Heart Program have been some of the most rewarding at Pitt, and I am excited to continue this work upon graduation. Oni Obi and Stephen Magill constantly reminded me of my passions in science, and always found an excuse to toast to the "usual." Jimi Bloom and Mike Samella have been dear friends, and I enjoyed the nearly three years we were housemates. They provided exceptional (and much needed) distractions from work and have created a fair share of incriminating memories (and likely more in the future). Importantly, they always reminded me to enjoy the present. Friends from Hebron Church – Greg Anderson, Keith Balkey, Barrett Hendrickson, Rob Gaunt, Matt Bender, Dave Bleivik, Peter Formica, and Geoff Gehring to name of few – provided encouragement, laughter, and constant reminders of the true importance of life. Undoubtedly I have missed people, but my absent mindedness does not imply any lack of gratitude.

From ninth grade and on, Joe "Coach" Ionta has been a major blessing in my life. His mentorship and support have been constant, and I appreciate his presence, especially during these last six years. Whatever difficulties come, I know I can count on him (and turn to one of the many books he has given) to provide mentorship. I thank my "extended family" of Dad and Mom Goldblum, and Molly, Nick, and Ian, who accepted me into their families, shown hospitality when the need arose, and supported me over the past four years. My sisters Stephanie and Autumn have been a gift and have helped in so many practical ways (from taking Mattie for walks to reminding me to laugh). My parents have been the epitome of encouragement. They have been here every step of this process, and whether it has been late night emails or weekly lunches at Wendy's, I am reminded constantly of their love and support. I am thankful for their push in pursuing a PhD, for their wisdom, and for the sacrifices they made for me along the way.

Finally, my wife Marnie has been a true expression of agape love. She chose to walk along side me, but at times has found herself carrying me instead. If our meeting was the sole blessing to come from this chapter of life, I count it unequivocally successful and undeniably worthwhile. I especially look forward to the new adventures in store for us.

I end with two thoughts, preserved in their original language:

> Οὐ μόνον δέ, ἀλλὰ καὶ καυχώμεθα ἐν ταῖς θλίψεσιν, εἰδότες ʽότι ʽη θλῖψις ὑπομονὴν κατεργάζεται, ἡ δὲ ὑπομονὴ δοκιμήν, ἡ δὲ δοκιμὴ ἐλπἰδα. ἡ δὲ ἐλπὶς οὐ καταισχὐνει, ʽότι ἡ ἀγάπη τοῦ θεοῦ ἐκκέχυται ἐν ταῖς καρδίαις ἡμῶν διὰ πνεύματος ἁγίου τοῦ δοθέντος ἡμῖν.
>
> (προς Ρωμαίους, 5:3-4)

> ὁ δὲ θεός μου πληρώσει πᾶσαν χρείαν ὑμῶν κατὰ τὸ πλοῦτος αὐτοῦ ἐν δόξῃ ἐν Χριστῷ Ἰησοῦ. τῷ δὲ θεῷ καὶ πατρὶ ἡμῶν ἡ δόξα εἲς τοὺς αἰῶνας. ἀμήν.
>
> (προς Φιλίππησίους, 4:19-20)

NOMENCLATURE

Acronyms	Definition
BMSC	Bone marrow stem cell
EHVT	Engineered heart valve tissue
EV-SLCM	Extended volume scanning laser confocal microscope
NNW	Needle non-woven
PA	Pulmonary artery
PAM	Polyacrylamide
PGA	Poly glycolic acid
PLLA	Poly l-lactic acid
POI	Post-implant
PRI	Pre-implant
PV	Pulmonary valve
RVOT	Right ventricular outflow tract
SALS	Small angle light scattering
SFRC	Short fiber reinforced composite
TEC	Tissue engineered conduit
UTS	Ultimate tensile strength

Sub- and superscripts	Definition
avg	Average
c	Composite
eff	Effective
ens	Ensemble
SF	Scaffold fiber
FM	Fiber-matrix
M	Matrix
R	Orientation distribution

Symbols	Definition
$\mathbf{A}$	Orientation tensor
$\mathbf{C}$	Right Cauchy-Green strain tensor
d	Fiber diameter
d_1	Constant of exponential ensemble stress response
d_2	Exponential of exponential ensemble stress response
D	Fiber end-to-end distance
D_g	Gage length
D_{g0}	Initial gage length
$\mathbf{E}$	Green’s strain tensor
L_c	Critical fiber length
L_T	Total fiber length
$\mathbf{N}$	Fiber direction vector

P, $\mathbf{P}$	1st Piola-Kirchhoff stress (tensor)
s_1	Beta distribution shape parameter 1
s_2	Beta distribution shape parameter 2
S, $\mathbf{S}$	2nd Piola-Kirchhoff stress (tensor)
t, $\mathbf{t}$	Cauchy stress (tensor)
$\mathbf{v}$	Vector
α	Anisotropy index
β	Eigenvalue
ε	Strain
θ	Zenith angle
λ	Stretch
μ	Shear modulus
μ_R	Orientation distribution mean
σ	Stress
σ_R	Orientation distribution standard deviation
τ	Shear stress
φ	Azimuth angle
χ	Short fiber orientation factor
Ψ	Strain energy density function
$\boldsymbol{\varphi}$	Volume fraction
ω	Tortuosity
Ω	Probability function

1.0 INTRODUCTION

1.1 THE TISSUE ENGINEERING APPROACH

1.1.1 Overview of the tissue engineering approach

Described in 1993 by Langer and Vacanti, tissue engineering (TE) is an interdisciplinary field utilizing engineering principals and methods to develop biological substitutes to restore native tissue functionality [1]. In this approach, autologous cells are isolated and grown on specialized porous scaffolds in vitro to provide sufficient mechanical and biological integrity for function upon implantation (Figure 1.1). As the rapid deposition and subsequent organization of extracellular matrix (ECM) including collagen and elastin are crucial to this paradigm, cell sources displaying such characteristics are utilized, such as bone marrow-derived stem cells (BMSCs). Ideally, TE based constructs have minimal immunogenic responses since autologous cell sources are used and they retain the ability to grow and repair with adjacent native tissue. The coordinated mechanical interplay between the degrading scaffold material and the depositing ECM is essential to the success of tissue engineering.

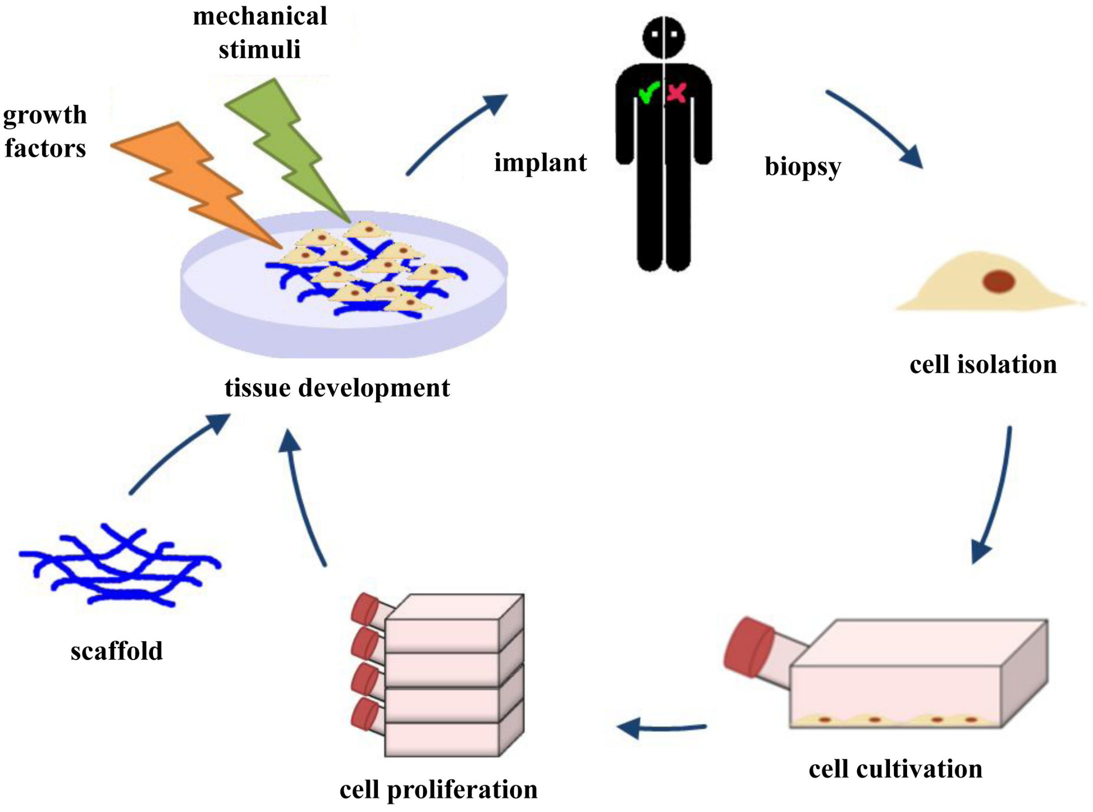

Figure 1.1. Overview of the tissue engineering approach. Adapted from HIA as per the Creative Commons Attribution 3.0 Unported license, under the GNU Free Documentation License. *Tissue Engineering*. 2010. **www.wikipedia.com**, April 2011.

At the present, a great deal of research surrounds ECM production and the scaffold selection, cell source, and in vitro culturing utilized with no clear penultimate identified. Indeed, particular systems targeted for therapeutic TE approaches likely will require an optimized selection of scaffold, cell, and conditioning, however, the variety of current permutations confounds efforts to evaluate the increasing body of literature surrounding TE. It is therefore essential to create a consistent platform to study TE and the quality of ECM formed by scaffold, cell, and conditioning selections in order to methodically investigate the isolated and synergistic effects of design choices.

1.1.2 Scaffold materials

A number of scaffold materials have been explored and utilized in TE applications. Decellurized native tissues have been explored for TE as they offer excellent structural similarities to the desired tissue structures, though concerns of long-term functionality due to strong detergents and decellurization agents raises questions [2-4]. Degradable synthetic scaffolds, such as those made from polymeric materials, represent some of the earliest materials used in TE [5, 6]. Such materials are attractive due their defined chemical and mechanical properties. Materials such as polyglycolic acid (PGA) have seen frequency use as they easily degrade in vivo, can be tailored for a number of different applications, and have a general acceptance in the medical community. In fact, PGA was used as the first synthetic absorbable suture material and since 1970 is still commonly used [6]. Other materials have seen popularity within tissue engineering such as polydioxanone, polyhydroxybutyrate, polycaprolactone, polyanhydrides, and polycyanoacrylates, though concerns over degradation byproducts has limited the use of some materials [6]. Recently, electrospun polyester urethane urea has gained attention due to its unique elastomeric properties that permit large deformations in vivo [7, 8]. Still, some of the most ubiquitous materials are PGA and copolymers with polylactic acid (PLLA) [9]. Often fabricated using needle nonwoven (NNW) processes, these scaffolds consist of crimped multifilament fibers [5]. Crimping imparts a characteristic waviness to the fiber structure. In the NNW process, fibers are mechanically brushed into a web exhibiting distinct preferred (PD) and cross-preferred (XD) directions. By punching an array of barbed needles through discretized points on the fiber webs, vertical loops are created which entangle surrounding scaffolds to create a highly porous but mechanically stable mesh [9-12].

1.1.3 Constitutive modeling of tissue formation within TE

To ultimately evaluate the mechanical quality of ECM formed within engineered tissues, means to distinguish ECM mechanical response components from scaffold mechanical response components within the composite material becomes essential. In relating the mechanical response of TE composites, two basic families of constitutive models exist: phenomenological models and structural models. In phenomenological models, experimental stress-strain data is fit to a form dictated by the overall mechanical response (i.e. linear, non-linear). As pioneered by Fung [13-17], these models often fit the data exceptionally well but provide little information in the underlying mechanistic reasons for the observed mechanical behavior. Especially in striving to elucidate tissue formation and remodeling, the lack of mechanistic insight outweighs the benefits of using such models. In structural models, microstructural tissue features dictate the form of the relationship and provide a mechanistic basis for the stress-strain response. Particularly in multi-parameter models, a structural basis permits the estimation and bounding of parameters based on independent experimental techniques and permits more reliable model relationships.

Though rigorous models for forming and remodeling tissue exist, many lack experimental validation and are not applicable to scaffold-ECM composites [18-22]. Significant improvements were made in recent work on polymeric degradable NNW scaffolds and forming tissues where Engelmayr and Sacks developed a general model for virgin scaffold material and extended it to the particular cell source utilized in engineered heart valve tissue [9, 23].

The first model proposed by Engelmayr and Sacks [9] focused on predicting the mechanical response of the NNW scaffolds in their virgin state. It relied on an understanding of the fiber microstructure and the interactions between fibers in flexure. This model was based on analytical solutions to two extreme cases of flexural fiber-fiber interactions first made by Freeston and Platt, that of “complete freedom” of relative fiber motion and “no freedom” of relative fiber motion. A number of assumptions were made in formulating the model, including:

1. Under small strains (<0.6%), constituent fibers are linear elastic, homogenous, and isotropic.
2. The representative volume element (RVE) boundaries are orthogonal to the applied stress direction, i.e. no shear in the scaffold (the shear stiffness has been reported to be ~2.5-fold higher than the elastic modulus for PGA, resulting in minimal shear deformations; additionally, the geometry of the flexure test ensured that the RVE boundaries were orthogonal to applied stresses).
3. Fiber diameter and scaffold thickness are small compared to the radius of curvature, i.e. small deformation.
4. Vertically oriented fibers do not contribute directly to the flexural rigidity.
5. Fiber effective stiffness is governed by fiber crimp (this effective crimp refers to the curved geometry spanning between rigid fiber-fiber bond points and not to the intrinsic crimp imparted during fabrication; Lee and Argon’s model was adapted for this assumption).

A novel finding from this model was the importance of fiber-fiber bond distance in NNW scaffolds. Through simulations it was shown that a decrease in fiber-fiber bond distances (i.e. closer attachments between fibers) resulted in an increase in the effective stiffness.

Moreover, this increase did not follow a traditional rule of mixtures, commonly defined as

$$Q_C = (1-\phi_F)Q_M + \phi_F Q_T \, , \tag{1.1}$$

where ϕ_F is the volume fraction of the scaffold fiber phase, and Q_C, Q_F, Q_M and are the respective property of interest in the composite, scaffold fiber, and matrix phases. Further, application of the model to previous in vitro data confirmed the simulation results, indicating that scaffold reinforcement was occurring due to tissue deposition. This necessitated the formulation of the meso-scale tissue-scaffold model using a form proposed by Niskanen [24] with additional assumptions:

6. Euler-Bernoulli bending occurs as supported by the linear moment-curvature behavior of the scaffold.
7. A transmural effective stiffness distribution exists in the composite.
8. The effective stiffness distribution is a linear function of the local ECM effective stiffness and the scaffold stiffness.
9. The local ECM stiffness is a function of the collagen specific stiffness, local collagen concentration, and bulk collagen concentration.
10. A coupling factor exists to describe the degree the ECM stiffness is influenced by scaffold attachment.

This model was capable of fitting the experimental flexure data and predicting ECM phase stiffness; further it showed important improvements to both collagen quality and quantity with mechanical stimulation.

Though adequate as first efforts, the models, however, are limited in a number of ways. Specifically, (a) the time evolution of the scaffold phase is not considered, (b) modeling of all tissue-scaffold interacts is difficult and the data is not easily obtainable, (c) PGA:PLLA scaffolds are not the penultimate but only a transition tool to understand tissue formation, (d) both models are restricted to flexural deformation and small strains, and (e) both models are not easily implanted into a finite element framework.

To this end, it is crucial to develop structural constitutive models that take into account the time-dependent microstructure of both tissue and scaffold phases. Importantly, these models must accommodate general large deformation modalities and be constructed in such a way to incorporate the potentially large scaffold-ECM interactions observed in previous work. As such models are based on quantifiable structural properties of its constituents, experimental techniques are necessary to provide sufficient insight to drive the model development.

1.1.4 Need for improved structural and mechanical insight

A variety of techniques currently exist to obtain three-dimensional structural information. In general, these techniques utilize a specific acquisition modality (magnetic resonance imaging, x-ray computed tomography, light microscopy) to obtain two-dimensional image planes and then use a variety of methods to stack sequential images planes to create a full three-dimensional volume [25]. Depending on the specific modality employed, a number of limitations exist that make the given technique difficult to use or introduce large error into the results. For example, in traditional three-dimensional imaging techniques using light microscopy, thin histological sections are cut from paraffin or ice–embedded samples, stained, and imaged using a light microscope. Samples often lack registration from one another, and though various fiducial marker systems and mathematical alignment processes exist, error still exists in the reconstruction process [25]. Additionally, cutting and mounting thin sections can introduce folding, bending, and tearing in the tissue, which can skew results. Cutting inherently removes material (and hence information) from the sample so that the reconstruction always consists of two-dimensional planes separated by gaps. In magnetic resonance imaging, x-ray computed tomography, and confocal modalities, finer out-of-plane resolutions can be obtained since scanning is based on focusing within the sample depth, but lower in-plane resolutions exist. The lack of cutting and mounting maintains serial registration between successive image planes, but the sample density can limit how deep into the tissue imaging can occur. Though in less-dense tissues such as brain tissue, depths exceeding 100 μm can be reached, denser materials, notably those of interest in mechanical modeling (such as bone and collagenous materials), can only be imaged down to 10 μm or less [25]. Delineation and segmentation of various tissue regions of interest is more difficult especially in magnetic resonance imaging, x-ray computed tomography modalities due to the lack of staining, so quantification of specific constituents cannot be performed to the same degree as in light microscopy techniques.

In much the same way, a variety of methods currently exist to obtain mechanical information of tissues. Commonly utilized, uniaxial testing is a relatively simple test greatly facilitated with the advent of commercially produced testing devices [26-28]. Though some qualitative information can be obtained, uniaxial testing, on its own, provides little useful information due to its non-physiological loading conditions. As a means to obtain more detailed and relevant information, Billiar and Sacks developed experimental methods to utilize a biaxial testing device to evaluate mechanical properties of native heart valve tissue [29, 30]. With this technique, planar tissues are loaded in a more physiological manner, and it permits the acquisition of a variety of sub-failure loading protocols to both better understand the functional response of tissues and to provide necessary mechanical data to more rigorously model such tissues. To date, however, little mechanical information can be found regarding TECs outside of some limited uniaxial experimentation [31]. Therefore, it is crucial to apply more advanced mechanical evaluation techniques, like biaxial tensile testing, to better assess the quality of TECs.

1.2 TISSUE ENGINEERING OF THE PULMONARY VALVED CONDUIT

1.2.1 Introduction

To investigate ECM formation and remodeling using improved structural models, tissue engineering of the pulmonary artery will be studied. Such a system provides reproducible in vivo tissue from a large animal. Further, previous work has shown success in implantation of TE constructs and has permitted the acquisition of tissue over a range of implant durations. Importantly, such a system has clinical applicability, providing a driving force for understanding how the mechanical quality of tissue changes with implant duration.

1.2.2 Anatomy of the heart

The human heart is an intricate four-chambered structure that serves to propel blood to both to the lungs for oxygenation and to the rest of the body to distribute nutrients and remove waste. The right and left ventricles, through a series of electrical impulses, contract, and two sets of heart valves coordinate opening and closing to regulate the direction of blood flow. A detailed illustration is provided in Figure 1.2. As supplied by the inferior and superior Vena Cava, the right atrium receives deoxygenated blood and moves it into the right ventricle. Upon filling and at the start of ventricular contraction, the tricuspid valve closes to prevent retrograde flow back to the atrium. The pulmonary valve opens when ventricular pressure exceeds that of the diastolic pressure in the pulmonary artery. Blood travels through the pulmonary artery to the lungs where it is oxygenated and then returns to the heart through the left atrium and into the left ventricle. Similar to the tricuspid valve, the mitral valve closes at the completion of ventricular filling, and contraction builds pressure to open the aortic valve and propel the blood through the systemic circulation. Amazingly, this complicated yet coordinated filling/ejection action happens in roughly one second, exceeding 2.5 billion cycles in an average lifespan.

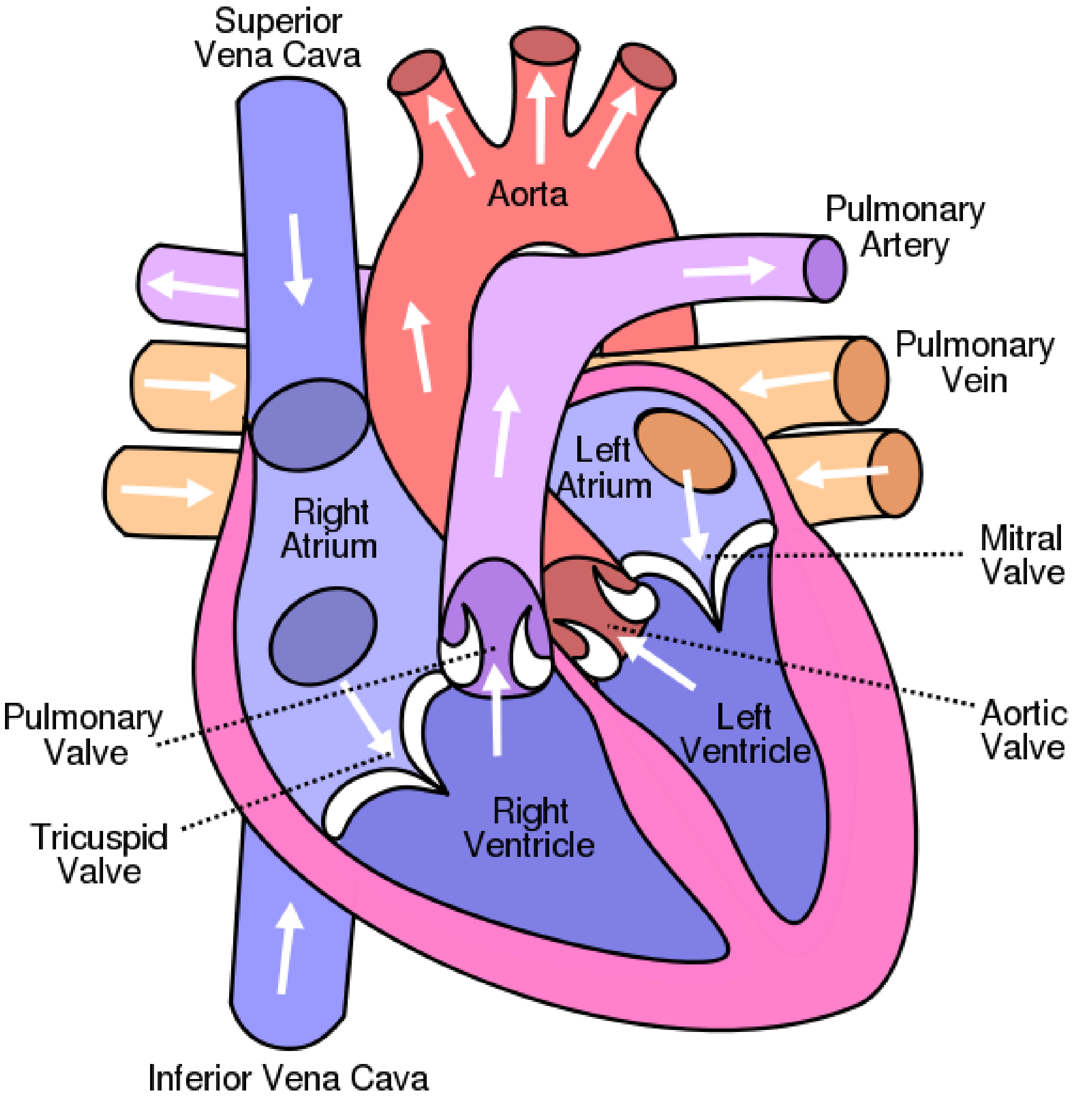

Figure 1.2. Anatomy of the human heart. Adapted from Pierce, Eric as per the Creative Commons Attribution ShareAlike 3.0 license, under the GNU Free Documentation License. *Pulmonary Artery*. 2006. **www.wikipedia.com**, April 2011.

1.2.3 Congenital defects affecting the pulmonary valved conduit

Though estimates vary, the incidence rate of congenital heart defects in annual live births in the United States is reported at 0.8%, equating to nearly 30,000 children born each year with such issues [32]. This number substantially increases when one considers worldwide birthrates. Of this estimate, slightly less than half of patients require surgical correction to establish normal anatomy and restore proper blood flow [33, 34]. Congenital defects can manifest in a variety of presentations including tetralogy of Fallot, hypoplastic left heart syndrome, tricuspic atresia, pulmonary stenosis, and pulmonary atresia (Figure 1.3), many of which result in malformations of the pulmonary artery. It should be noted that congenital heart defects remain as one of two largest causes of infant mortality in North American [34].

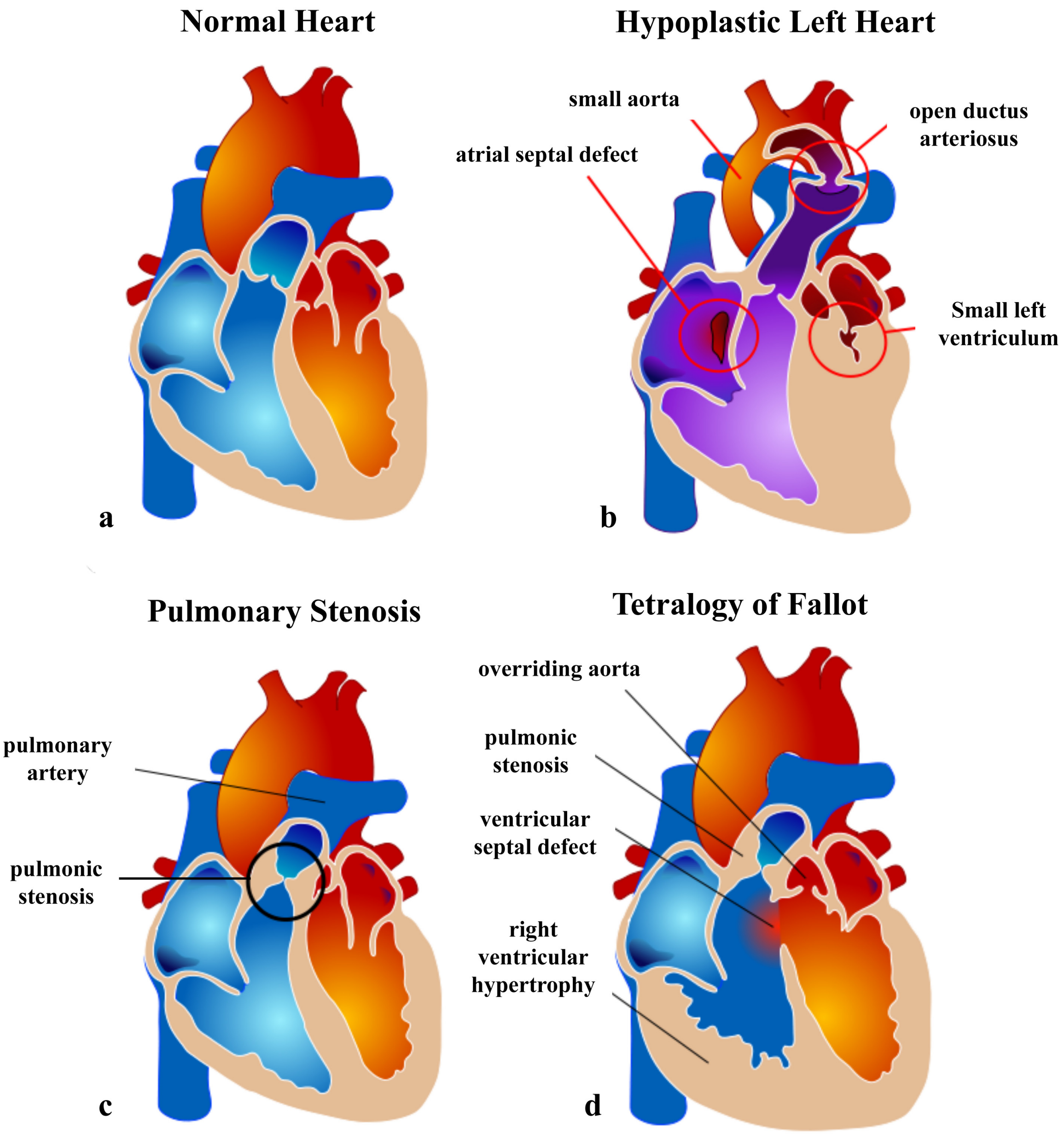

Figure 1.3. Normal heart with common congenital defects affecting pulmonary artery. Shown are (a) normal heart, (b) hypoplastic left ventricle, (c) pulmonary stenosis, and (d) tetralogy of Fallot. Adapted from Ruiz, Mariana as public domain. Hypoplastic Left Heart, Pulmonary Stenosis, and Tetralogy of Fallot. 2006. www.wikipedia.com, April 2011.

1.2.4 Surgical options and limitations

A number of procedures exist to surgically correct congenital heart defects, many of which require partial or full reconstruction of the pulmonary artery / right ventricular outflow tract (PA/RVOT) [35], such as the Rastelli, Ross, and Fontan procedures. Current clinical options for reconstruction of the RVOT include bioprosthetic, allogenic, and autogenic grafts, but these suffer from a number of limitations [35-37]. In the cases of bioprosthetic and allogenic grafts, these conduits are potentially thrombogenic, susceptible to infection, and may display calcification and restenosis [37-40]. Additionally, they are rendered inert and are thus unable to repair, remodel or somatically grow with the patient (requiring additional operations as the patient grows). The use of autogenic grafts, as in the Ross procedure, is more attractive because these grafts are living tissue from the patient, but they require an additional graft from the donor site (with the pulmonary artery being the donor site). It is clear that a clinical need exists to develop better conduit therapies for PA/RVOT reconstruction.

1.2.5 Current state of TE for PA/RVOT reconstruction

A discord exists between the number of publications focusing on improved surgical techniques for congenital heart defects requiring PA/RVOT reconstruction and the number of publications proposing new therapies, including those making use of tissue engineered conduits (TECs). Though a number of publications exist on tissue engineered arteries and smaller vessels, the challenges associated with replicating the “great vessels” (i.e. primary vessels to and from the heart, such as those requiring reconstruction as a result of congenital heart defects) have hindered similar progress. Within the paucity of published research on TECs, variation exists among cell types, scaffold materials, culturing techniques, and subsequent analysis, making efforts to understand the overall functional equivalency of TECs and the factors that prominently influence results less clear. Earlier work by Shinoka et al. [36] made use of nonwoven polyglycolic acid scaffolds seeded with endothelial/myofibroblastic cells isolated from either ovine jugular veins or carotid arteries. Though the work proved the feasibility of the TEC concept, results were limited to bulk assays (collagen, calcium, etc.), histology, and gross morphology and did little with understanding how tissue formed and remodeled towards physiological functionality. Leyh et al. [41] investigated the effects of acellular allogenic conduits versus cellularized allogenic conduits using decellularized ovine pulmonary arteries. Though the work showed improved conduit integrity with the cellularized group after six months of implantation, conclusions of ECM formation are questionable since the implanted conduits started as decellularized ECM scaffolds.

Both Isomatsu et al. and Shin'oka et al. [42, 43] investigated TECs implanted in human patients, showing reasonable success of the conduits up to 25 months post implant. Unfortunately, such studies provide little in detail regarding tissue formation/remodeling in the TECs since (fortunately) the implanted conduits did not require removal at the time of the studies' publications. Hoerstrup et al. [31] performed the most comprehensive long term in vivo animal study to date, investigating vascular endothelial cell-seeded nonwoven PGA scaffolds in sheep up to 100 months post implant. This work made use of some quantitative tissue analysis techniques such as collagen and glycosaminoglycan content but had limited biomechanical analysis techniques (uniaxial extension) that failed to capture physiological stress states. As in the other studies, little information beyond histological assessment is provided for tissue growth and remodeling. Though encouraging, most current TEC work is empirically based, limited in scope, and has not elucidated time course changes in structure and mechanical behavior necessary to properly evaluate tissue formation and remodeling.

1.3 OBJECTIVES

1.3.1 Research motivation

In a very general sense, the principle drive of this present work is to elucidate the long term in vivo remodeling processes in engineered cardiovascular tissues using constitutive models developed from first principles and based on quantifiable microstructural details. As such, the overall approach and development of a consistent, repeatable testing platform is essential to the success of this work. With a rigorously defined system in place, it will be possible to investigate the events of tissue formation and remodeling within a tissue engineering context and ultimately inform and direct the design of future engineered tissues. Therefore, central to this work is the hypothesis that structurally based constitutive models can provide necessary insights into the formation and remodeling of engineered tissues.

1.3.2 Outline and specific contributions of this work

Central to this entire research effort is not only to assess the influences of in vivo mechanical stimuli on tissue formation and remodeling on polymeric degradable scaffolds, but to develop a methodical approach to investigate this system and, importantly, to provide defined means to apply such an approach to other systems (based on anatomical tissue of interest, scaffold type, cell source, mechanical stimuli, etc.). With such a system developed, it will be easier to evaluate future changes and improvements to engineered tissues, beyond TECs.

This work commences by describing a means to evaluate the structure of engineered tissues in three-dimensions as driven by the lack of such detailed information (Aim 1). The motivation, as described in section 1.4, is born out of a need to understand how the scaffold phase of tissue engineered composites mechanically and structurally interacts with the tissue phase at various timepoints. As the initial condition, it is also essential to understand the three dimensional structure of scaffolds prior to any cell seeding or tissue accretion. Insight into how and when, if at all, degradation occurs is essential to evaluating the overall quality of tissues. Detailed morphology beyond what can be normally obtained through two dimensional histology is described as well as a brief study to reduce information gathering back to two dimensions with sectioning size, direction, and frequency guided by the full three dimensional data sets.

The work continues by developing the mathematical framework for two general large deformation models to estimate tissue mechanical properties from composite properties in scaffold fiber-ECM systems (Aim 2). This work, being guided by specific morphological insight from Aim 1, develops a platform using a tissue simulacre with experimentally determined mechanical properties embedded with either an intact continuous scaffold phase or a fragmented discontinuous scaffold phase to evaluate the overall composite effect and investigate how such scaffolds interact with a matrix of similar properties to native tissues. Biaxial tension, uniaxial extension, and pure shear experiments are performed on the simulacre tissue system to determine relevant mode parameters.

Finally, the work utilizes the models developed in Aim 2 on tissue engineered pulmonary conduits implanted in vivo over a range of duration in an effort to understand how ECM forms and remodels (Aim 3). The continuous fiber model is applied to mechanical data from TECs ranging from zero (cultured but not implanted) to seven days post implant in an ovine system.

Tissue mechanical properties are estimated using the model, illustrating how tissue forms on continuous intact scaffolds. The discontinuous model form is then applied to mechanical data from TECs ranging from 42 to 140 days post implant in an ovine system. Changes to the overall structure and mechanical response with implant time are described for TECs. The results of both will illustrate the substantial impact the intact scaffold has on the overall mechanical properties and how the initial scaffold architecture plays a major role in determining the formed tissue architecture.

1.3.3 Specific contributions

As a means to understand the in vivo tissue formation and remodeling events in engineered cardiovascular tissues, it is the overall intent that this work will provide important contributions to this end. Specifically, contributions of this current work will include:

1. A technique to quantify high-resolution three-dimensional structural details in engineered tissues to guide constitutive model development.

2. Structurally based finite deformation constitutive models to determine tissue properties of engineered constructs.

3. A repeatable experimental platform to assess tissue-scaffold interactions.

4. Insights into tissue formation and remodeling in the clinically relevant pulmonary valved conduit application.

2.0 THREE-DIMENSIONAL QUANTITATIVE MICROMORPHOLOGY OF PRE- AND POST-IMPLANTED ENGINEEREED HEART VALVE TISSUES

2.1 INTRODUCTION

Rigorous three-dimensional (3D) structural analyses and quantification of constituents of interest are a crucial component to assessing the functional equivalency of engineered tissues. Such information can provide guidance to the form of the constitutive relation and yield insight into how more simple structural analyses can be performed (i.e. two dimensional sectioning frequency, sectioning orientation, etc.). Current methods of 3D structural analyses are difficult to use or introduce large error into the results. For example, in traditional 3D imaging techniques using light microscopy, thin histological sections are cut from paraffin or ice–embedded samples, stained, and imaged using a light microscope. Successive samples often lack registration, introducing error in the reconstruction process [25]. Additionally, cutting and mounting of thin sections can introduce folding, bending, and tearing in the tissue that can skew results. In confocal modalities, finer out-of-plane resolutions can be obtained though at the expense of in-plane resolution. The lack of cutting and mounting sections maintains serial registration between image planes, but the sample density can limit how deep into the tissue imaging can occur, in some cases 10 μm or less [25].

In the present study a novel means to both acquire and analyze high resolution 3D structural data in engineered tissues was developed. Specifically, engineered heart valve tissue (EHVT) was investigated due to its availability for study and its similarity in fabrication (scaffold, cell seeded, and implant location) to TECs. As a result of the limitations of traditional 3D imaging techniques, an extended-volume scanning laser confocal microscope was utilized at the Bioengineering Institute at the University of Auckland, New Zealand [25, 44]. Non-seeded PGA:PLLA scaffold, pre-implant EHVT (PRI), and post-implant EHVT (POI) were investigated to elucidate structural changes during both the in vitro and in vivo phase. In addition, native ovine pulmonary valve (PV) was also evaluated as a means to test this approach for native tissues.

2.2 METHODS

2.2.1 Engineered tissue fabrication

For both PRI and POI, specimens, cell isolation, culturing, and seeding, along with scaffold preparation and implantation was performed as part of another study and has been described in detail [45]. Briefly, BMSCs were isolated from female Dorset sheep, cultured and expanded, and seeded at 0.5-1.7x 10^7 cells/cm^2 onto sheets of non-woven 50:50 PGA:PLLA scaffold fabricated into valved conduits. These seeded constructs (PRI tissue) were statically cultured for four weeks. For the POI tissues, these valve and conduit assemblies were implanted into the pulmonary artery of Dorsett sheep and then explanted at various timepoints. For this particular study, a specimen explanted after twelve weeks was used.

2.2.2 Extended-volume scanning laser confocal microscope

To acquire volumetric data, a novel microscopy rig at the University of Auckland was utilized, as shown in Figure 2.1. With this device, a conventional scanning laser confocal microscope was used to obtain high-resolution two-dimensional (2D) plane images with small steps through the z-direction (to obtain high-resolution cubic voxels of 1 μm^3 or less). A precision two-bladed diamond-tipped ultramill was employed to cut scanned volumes from the specimen and create optically smooth surfaces as previously described [25, 46]. Removing scanned volumes and scanning subsequent volumes permitted the acquisition of large volumetric data (over hundreds or thousands of microns) while maintaining a high resolution (micron or smaller) that resulted in high-resolution 3D images of large volumes.

Figure 2.1. EV-SLCM rig at the University of Auckland.

2.2.3 Specimen preparation

In the PRI and POI tissues, each leaflet was cut into three equal-sized radial strips, stored in paraformaldehyde, and shipped to the University of Auckland. Additionally, a native ovine PV leaflet excised during implant was stored and shipped in paraformaldehyde. Full thickness sections approximately 6 mm by 3 mm were cut from the central region of each full specimen. In total, a native PV, a four week in vitro PRI tissue, a twelve week in vivo POI tissue, and a non-seeded PGA:PLLA co-polymer non-woven scaffold were imaged using the EV-SLCM system. Additionally, 2D image scans were performed on non-seeded 100% PGA and pre-seeded 100% PLLA to guide image analysis procedures.

Prior to scanning, a number of processing techniques were required to properly prepare the samples, as detailed in previous work [25, 46]. Briefly, all specimens (except the non-seeded scaffold) were stored in 10% paraformaldehyde. Specimens were washed in PBS solution, stained with 0.15% picrosirius red for two days, and rinsed with Bouin's solution. After graded alcohol dehydration, specimens were embedded in resin for the native, PRI, and POI in Procure 812 resin (ProSciTech, Queensland, Australia) and dyed Spurrs resin (ProSciTech, Queensland, Australia) dyed for the non-seeded scaffold. Following a 24 hour bake at 60^{o}C, specimen blocks were mounted on aluminum plates using epoxy for imaging.

2.2.4 Specimen Imaging

Each specimen was imaged using previously published techniques, explained in detail in previous work [25, 46]. Briefly, a 500 by 500 μm field of view was imaged at 1 μm/pixel resolution in a particular image plane with 4x line scan averaging to reduce noise. Multiple adjacent images were captured (with 50% overlap) to provide a full image plane of approximately 1.0-1.5 mm^2. Both the overlap and line scan aided in reducing in-plane noise to less than 1 μm (personal communication with Mr. Dane Gerneke). A series of 1 μm deep 2D image planes were captured over a specific total depth; after imaging, 80% of the imaged volume was removed using the ultramill. Specimens were imaged again at 1 μm/pixel in-plane resolution with 1 μm 2D image plane steps, and this process was repeated until the total desired specimen depth was reached. A high-resolution translation stage (0.3 μm error per 600 mm total translation per direction) maintained serial registration during milling. To assess inter-and intra-specimen variability, three to four image planes spaced 100 μm apart were acquired at various locations on the same specimen (midpoint and end on PRI, tip, midpoint, and attachment point on POI) and on different specimens (two PRI, three POI) to qualitatively assess inter- and intra-specimen variability. After imaging, 2D images were processed prior to analysis to remove noise and background illumination irregularities, assembled into 2D planes using a cross-correlation technique, and stacked into continuous 3D volumes of x-y plane images as discussed in previous work [25, 46]. The entire process resulted in errors of approximately 1 μm in all three directions (personal communication, Mr. Dane Gerneke) in full-resolution data sets.

2.2.5 Scaffold Analysis

To quantify scaffold information, consecutive 2D image planes were imported into a custom MATLAB program. Scaffold constituents were segmented based on intensity thresholding and dilation/contraction operations. Preliminary scans showed that pre-seeded scaffold (PGA and PLLA) appears as dark regions. In the pre-implant and post-implant specimens, PGA appeared as dark geometrical regions while the PLLA appeared as bright geometrical sections, enabling unique labeling using built-in MATLAB commands. Using a previously developed algorithm

[47], labeled scaffold fiber cross sections were associated with the same scaffold fiber cross sections in successive image planes. The scaffold fibers were represented as a series of points in 3D by calculating the cross sections' centroids. 3D curve tracing was then applied to the centroid points to label the scaffold fiber trajectories, the labels were then mapped back to the 3D data sets. With this method, individual scaffold fibers were tracked despite scaffold fiber overlaps.

Centroid data for each scaffold fiber through each slice enabled the calculation of the number of scaffold fibers, the scaffold fiber end-to-end distance D, defined as

$$D = R\sqrt{\left(X_n - X_1\right)^2 + \left(Y_n - Y_1\right)^2 + \left(Z_n - Z_1\right)^2} \tag{1.1}$$

where R is a scaling factor (determined by image resolution and the resampling factor, n the total number of two dimensional sections, (X,Y,Z) the Cartesian coordinates of the scaffold fiber's centroid. From this information the true scaffold fiber length L_T was computed using

$$L_T = R\left[\sum_{n=1}^{M}\sqrt{\left(X_n - X_{n-1}\right)^2 + \left(Y_n - Y_{n-1}\right)^2 + \left(Z_n - Z_{n-1}\right)^2}\right] \qquad (1.2).$$

Using scaffold fiber end-to-end distance and true scaffold fiber length, the scaffold fiber tortuosity was defined as

$$\omega = \frac{L_T}{D} \qquad (1.3).$$

In addition, scaffold volume fraction, scaffold fiber diameter, and minimum scaffold fiber-fiber distances were computed.

As a means to quantify changes in the scaffold fiber orientation as a function of EHVT timepoint, an orientation tensor was computed for each sample [48-51]. In this, each vector $\mathbf{v}$ was normalized and converted to a spherical coordinate system based on

$$\mathbf{v}_1 = \sin\theta\cos\varphi \qquad (1.4),$$

$$\mathbf{v}_2 = \sin\theta\sin\varphi \tag{1.5}$$,

$$\mathbf{v}_3 = \cos\theta \tag{1.6}$$,

with θ and φ defined as zenith angle and azimuth angle, respectively. Since both scaffold fiber ends were not distinguishable from one another, $\mathbf{v} = -\mathbf{v}$, which limited the angles θ from ${}^{-\theta}\!/_{2}$ to ${}^{\theta}\!/_{2}$ and φ from ${}^{-\varphi}\!/_{2}$ to ${}^{\varphi}\!/_{2}$ A general description of the orientation state was determined by using a probability distribution function $\Omega(\mathbf{v})$, done by taking the dyadic products of the vector $\mathbf{v}$ and integrating over the range of θ and φ and weighting the product by $\Omega(\mathbf{v})$ where the probability of finding a scaffold fiber between θ_1 and $\theta_1 + d\theta$ and φ_1 and $\varphi_1 + d\varphi$ was given by

$$G\left(\theta_1 \le \theta \le \theta_1 + d\theta, \varphi_1 \le \varphi \le \varphi_1 + d\varphi\right) = \Omega\left(\theta_1, \varphi_1\right)\sin\theta_1 d\theta d\varphi \tag{1.7}$$.

Restrictions placed on this function limited the integration over orientation space to unity and force the function to be an even function; however, it was not practical to compute the distribution function, and so another approach was taken. In this approach, an orientation tensor was created by forming dyadic products of the vector $\mathbf{v}$ and integrating it over all directions and weighting the product with the distribution function and scaffold fiber length. This created a second order tensor as

$$\mathbf{A}_{ij} = \frac{\int_L \int_p v_i v_j L_T \Omega\left(\mathbf{v}, L_T\right) dv\, dL_T}{\int_L \int_p L_T \Omega\left(\mathbf{v}, L_T\right) dv\, dL_T} \tag{1.8}$$.

In a discrete system, the tensor components were calculated using a summation instead of integration

$$\mathbf{A}_{ij} = \frac{\sum\left(v_i v_j\right) L_{Tn} F\left(\theta_n\right)}{\sum L_{Tn} F\left(\theta_n\right)} \quad (1.9).$$

To account for the increased probability of scaffold fibers oriented normal to the sectioning plane intercepting the plane rather than scaffold fibers oriented parallel to the plane, a weighting function $F(\theta_n)$ was introduced [49-51] as

$$F(\theta_n) = \frac{1}{L_T \cos\left(\theta_n\right) + d \sin\left|\theta_n\right|} \quad (1.10).$$

In this form, d was defined as the scaffold fiber diameter.

Eigenvalues and the associated eigenvectors were computed for the orientation tensor, which represent overall scaffold fiber ensemble principal directions and given a sense of the general orientation of the scaffold fibers. Additionally, a spherical histogram was created with the principal directions to further illustrate the orientation distribution of the scaffold fibers. By performing a histogram binning operation over equal solid angles of the hemisphere (symmetry is preserved reducing the sphere to a hemisphere), the relative percentage of scaffold fibers passing through an equal area section of the unit hemisphere surface provided another quantitative measure of scaffold fiber orientation [52].

Since utilizing the EV-SLCM system to acquire full 3D data sets has been found to be impractical for large specimen database [46], it was prudent to determine the minimum number of 2D histological sections required to provide salient structural information in EHVT. This was performed using both metrics for the scaffold fibers and for the collagen. To evaluate the effects of sectioning frequency on scaffold fibers, the eigensolutions for a given data set were computed as a function of increased resampling rates in the milling direction. In this way, changes from the true full resolution orientation tensor eigensolutions could reveal the impact of reduced sectioning resolution and will help guide histological sectioning frequencies. Since the scaffold analysis files began with a 3 μm sectioning spacing, additional spacings of 5 μm, 10 μm, 25 μm, and 50 μm were used. As a means to evaluate changes in computed orientation, an anisotropy index was used defined as

$$\alpha_{ij} = 1 - \frac{\beta_j}{\beta_i} \quad i > j \tag{1.11}$$

where β are the eigenvalues of the fabric tensor [53]. In this index, values approaching unity indicate a strong anisotropic orientation, while values approaching zero indicate a strong isotropic orientation. By comparing this index between eigenvalues as a function of sectioning frequency, it is possible to investigate potential errors from increased sectioning spacing on perceived scaffold fiber orientation.

2.2.6 Collagen and cell quantification

For collagen and cell quantification, specimen image stacks were segmented using thresholding, region-growth gradient operators, and drawing tools in order to selectively mask/highlight constituents of interest. This permitted the computation of constituent area fractions in a section-by-section manner that could be summed to provide volumetric constituent densities. Collagen, bound to picrosirius red stain, appeared as high-intensity pixels, while cell nuclei appeared as morphometrically distinct objects with higher-intensity pixels (due to the absorption and fluorescence of paraformaldehyde). The background resin had a distinguishably lower intensity while constituents not bound to the picrosirius red stain had the lowest intensity. Occasionally, high densities of collagen produced high-intensity pixel regions, but they were morphometrically different from nuclei.

Full-specimen masks and collagen-specific masks were created and to compute collagen frequency of a given pixel region (this ensured collagen could not be erroneously segmented outside of the tissue boundary). To produce collagen distributions along a single direction, binary pixel intensity (0 for non-collagen, 1 for collagen) was summed along two directions to produce a plane-based area fraction; this was measured along each section of the third direction to show planar distributions (i.e. XY plane along Z direction). A similar technique was employed to provide insight into cell density based on the segmentation of nuclei. Since the imaging technique could only distinguish nuclei and not entire cell volumes, however, it was only able to provide a qualitative sense of cellular distribution within the specimen a not an accurate quantitative density measurement. As a means to count cells though, the same scaffold fiber tracking technique was employed based on cell nuclei. Since the z resolution was greater than the size of the nuclei, each nucleus appeared in multiple image planes. As such, a more-accurate cell count was obtained by using the same algorithm used to track scaffold fibers.

As in the scaffold fiber analysis, the effects of varied 2D sectioning frequency on measured collagen densities were investigated. In all three collagen-containing datasets (native PV, PRI, and POI), the full data set (1 μm spacing) was used as a reference, while spacings of 2 μm, 10 μm, 25 μm, and 50 μm were investigated in all three directions. Stacks of segmented images (either masked or outlined) were assembled into a single TIFF file using ImageJ (NIH, Bethesda, MD, USA). Single files were imported into VOXX (Indiana University Medical Center, Indianapolis, IN, USA), a freeware voxel-based volume rendering program.

All computed values were represented as mean +/- standard deviation. For the scaffold area fraction analysis, a 1-way ANOVA test was performed with a Dunn's post-hoc test used for pairwise comparisons (due to the failure of equal variance, a non-parametric Kruskal-Wallis

ANOVA test on ranks was used to compare groups). Statistical significance between groups was assumed when $p < 0.05$.

2.3 RESULTS

2.3.1 Native pulmonary valve collagen and cell analysis

3D reconstructions of collagen within the native leaflet (Figure 2.2) and collagen density profiles along each of the three directions (radial, circumferential, transmural) (Figure 2.3) were created from the image sets. Qualitatively, collagen varied transmurally showing variations from 70-90% (ventricularis) down to nearly 40% and back up to 95% (fibrosa); radial variation was 55-80% along the length of the leaflet, with a nearly steady collagen density of 70% along the circumferential direction. 2D histology (hematoxylin and eosin stain, 4x magnification) of the native PV showed similar qualitative trends (Figure 2.2). A reconstruction (Figure 2.2) displays the cell nuclear material from the full volume with relative density along all three directions (Figure 2.3). Slight variations seen in the transmural direction were evident, while a fairly constant (near 2%) density was seen in the circumferential direction. Additionally, a sub-volume was analyzed using the centroid tracking technique, finding 2, 363 unique objects throughout a 0.0101 mm^3 sub-volume, and yielding a cell density of 2.33 x 105 $cells/mm^3$.

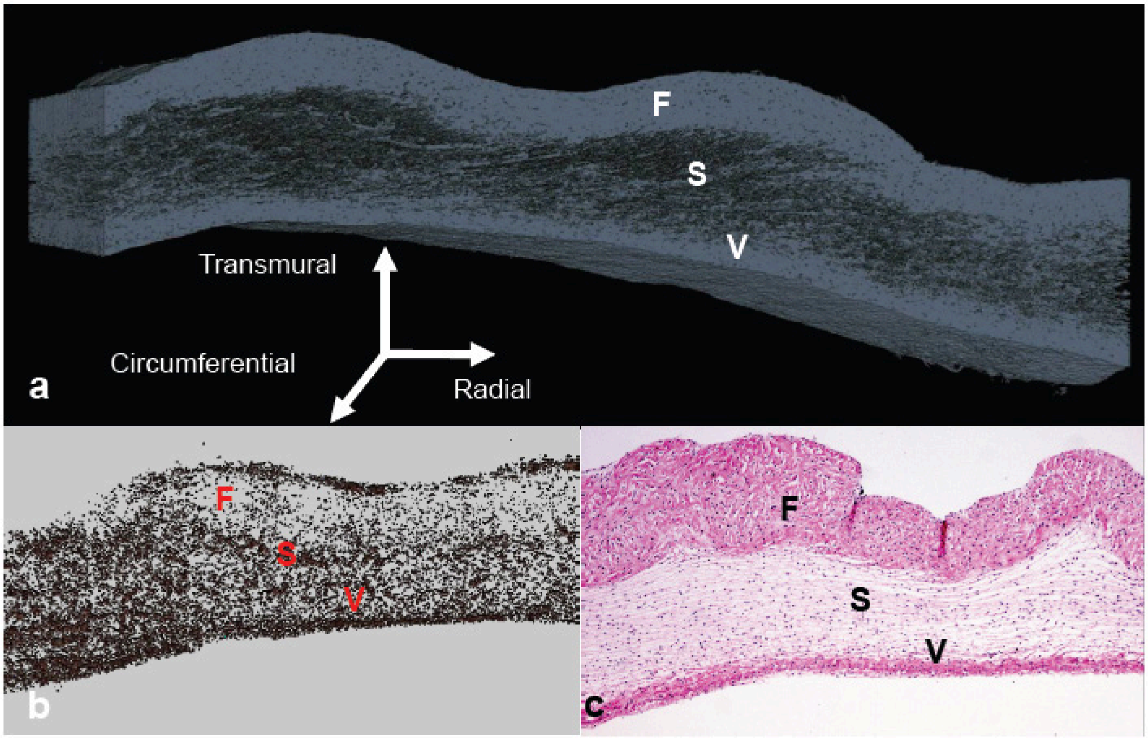

Figure 2.2. 3D reconstruction of the native PV. (a) Collagen and (b) cellular material; (c) traditional 2D H&E histology image of the native PV with 4x magnification. In all images, the fibrosa (F), spongiosa (S), and ventricularis (V) layers are labeled.

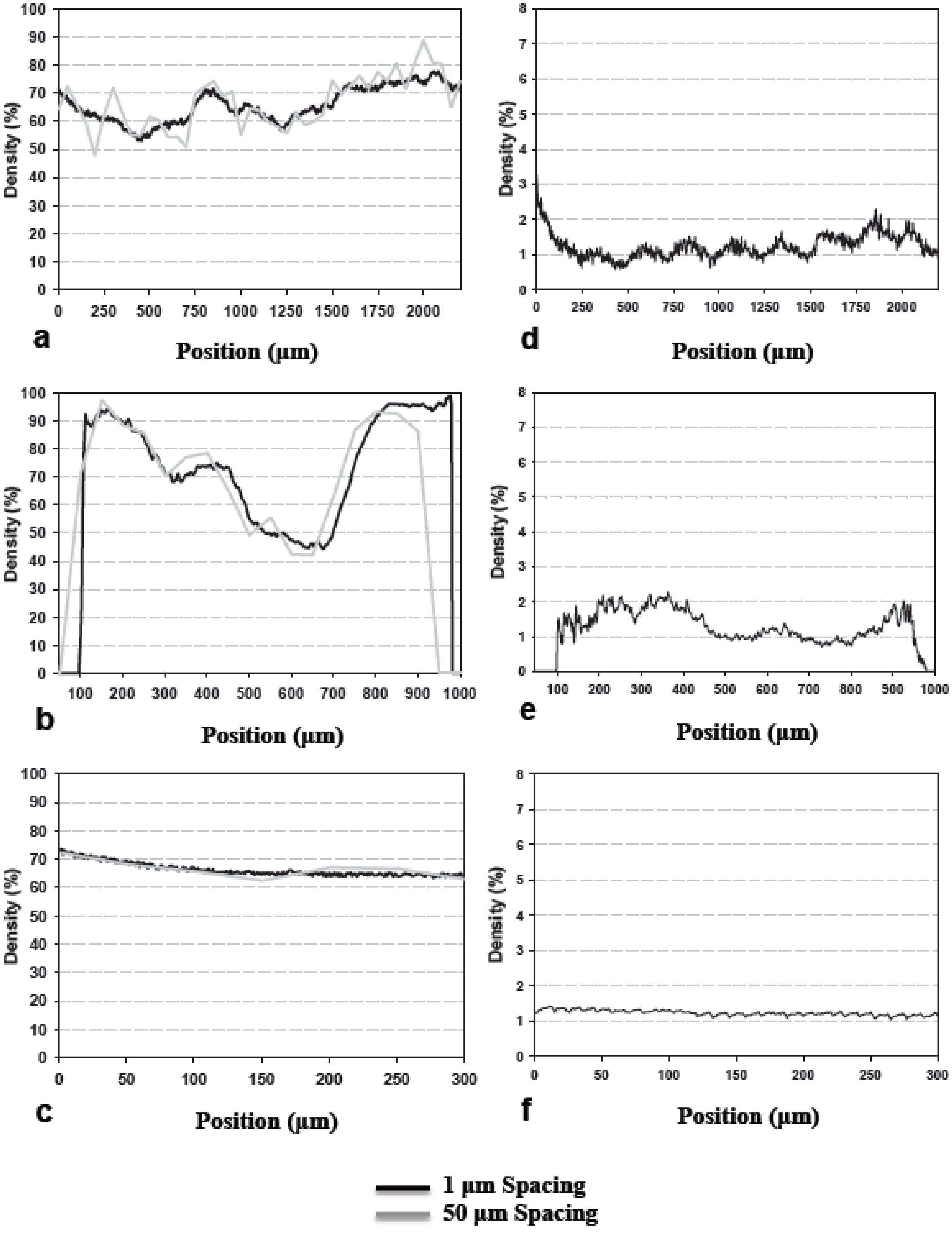

Figure 2.3. Collagen and cell density distributions in the native PV. Shown are (a) radial, (b) transmural, and (c) circumferential directions for collagen with varied sectioning spacing (from 1 µm to 50 µm), and (d) radial, (e) transmural, and (f) circumferential qualitative cell density distributions (based on cell nuclei measurements).

2.3.2 Pre-seeded scaffold analysis

In PGA:PLLA scaffold prior to seeding with cells, a total volume of 731 μm x 989 μm x 410 μm (0.296 mm^3) was sampled at a 1 μm/pixel resolution; 450 scaffold fibers were tracked. A two dimensional imaged section of the pre-seeded scaffold along with typical imaged sections of the PRI and POI are presented alongside histology, with individual scaffold fiber type listed (Figure 2.4). The scaffold fiber diameter histogram peaks within the co-polymer (Figure 2.5) aligned closely with separate PGA and PLLA scaffolds (not shown) with PGA having a mean scaffold fiber diameter of 14-18 μm and PLLA having a mean scaffold fiber diameter of 22-24 μm in the individual scaffold. Similar peaks of 14-18 μm (PGA) and 20-24 μm (PLLA) in the co-polymer illustrate the ability of the imaging/analysis technique to distinguish different scaffold fiber types based on morphology.

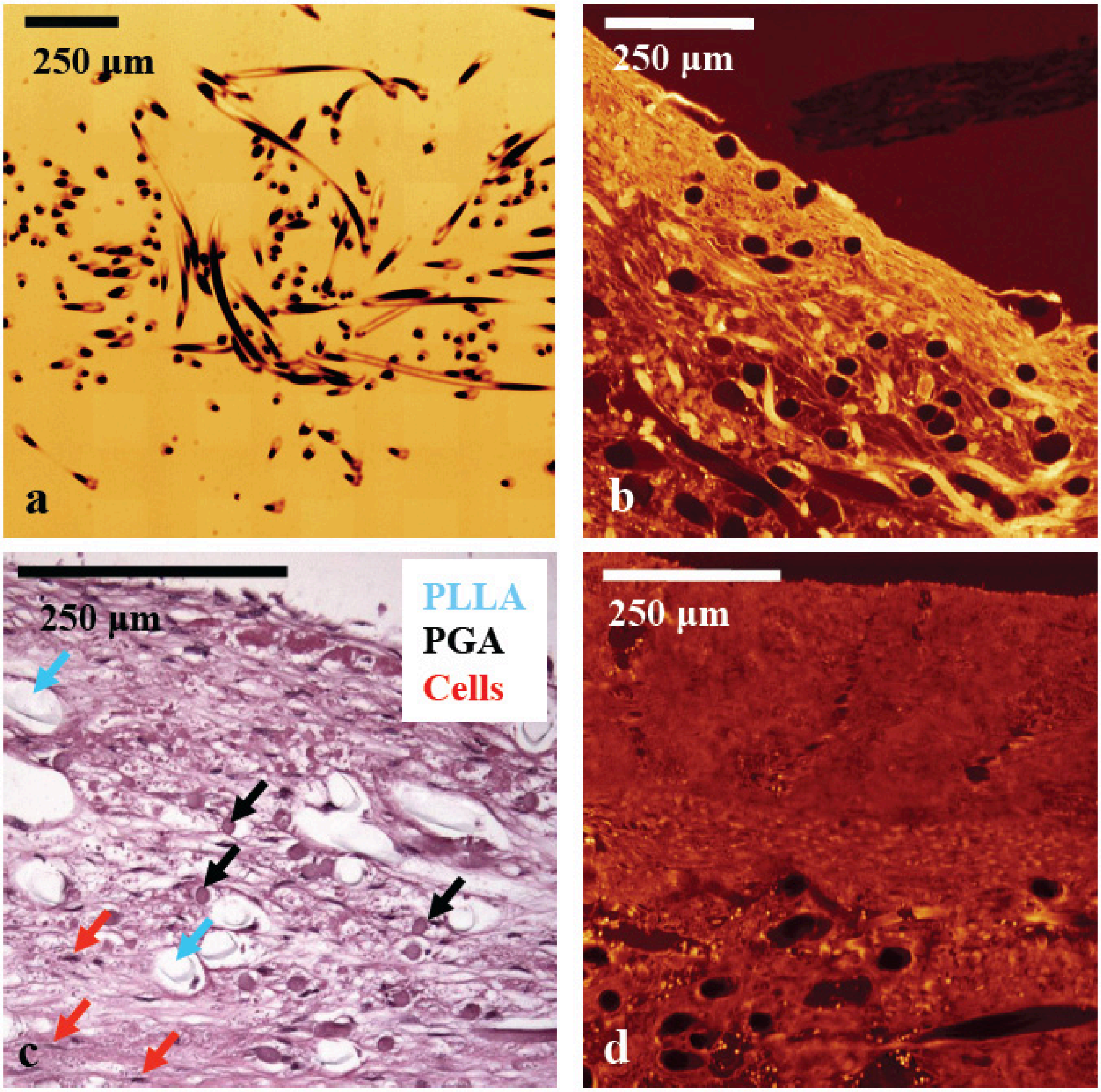

Figure 2.4. EV-SLCM imaging of pre-seeded scaffold, PRI, and POI, (a,b,d); (c) H&E staining of PRI timepoint specimen showing distinct PLLA and PGA fibers.

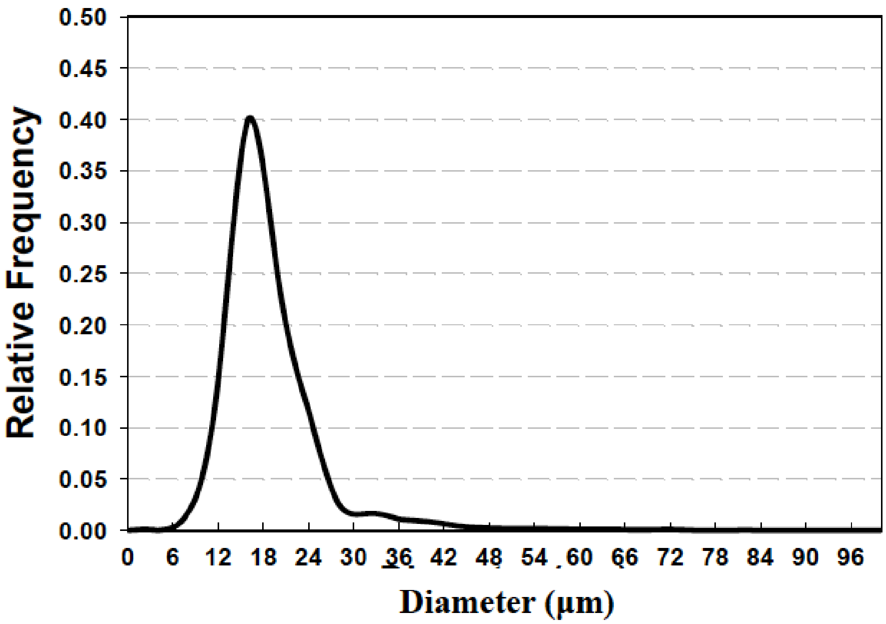

Figure 2.5. Fiber diameter histogram for the pre-seeded PGA:PLLA scaffold.

Scaffold fiber area fraction over the imaged area as a function of 2D section was computed (Figure 2.6) and showed some variability throughout the volume with a range of 5.17% to 9.43%, with a mean +/- standard deviation area fraction of 7.02 +/- 1.02%. A histogram of scaffold fiber tortuosity (Figure 2.7) revealed a substantial frequency peak at 1.05, with nearly all scaffold fibers having a tortuosity less than 1.20. Minimum scaffold fiber separation (Figure 2.8) showed a distinct peak at 10 µm with nearly all scaffold fibers within a 0-20 µm separation of one another. A length histogram was not produced for this data set because the analyzed volume compared to the fiber length was not large enough to prevent a relatively homogenous length distribution resulting from an artificial weighting (towards lower lengths) of length from the cross-preferred and out of plane fibers. Further, the 3D reconstructions illustrated the highly contiguous nature of the fibers.

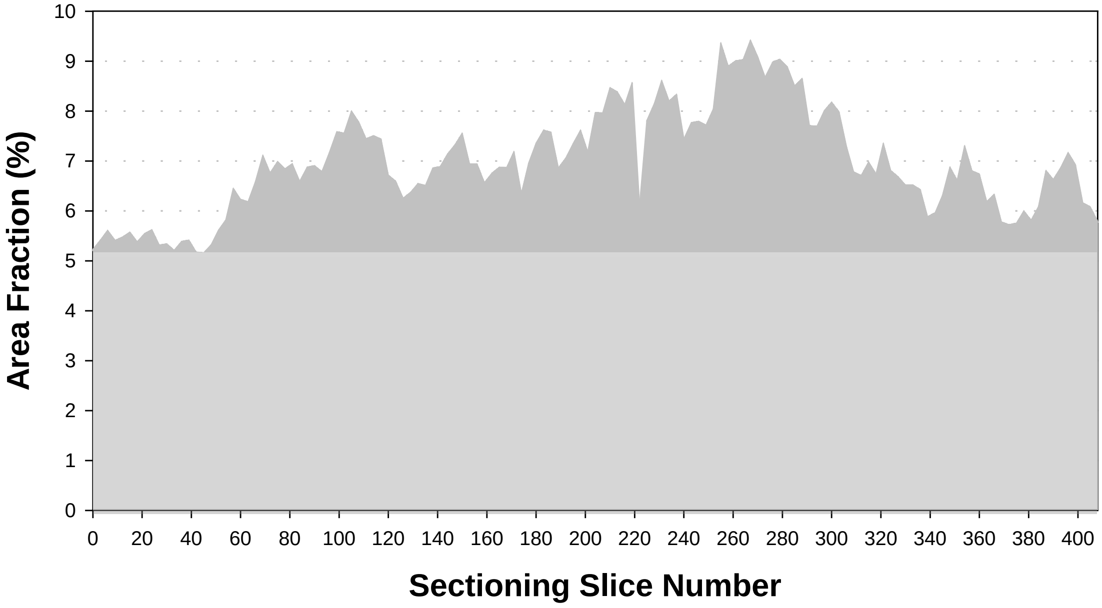

Figure 2.6. Pre-seeded scaffold area fraction as a function of 2D section slice.

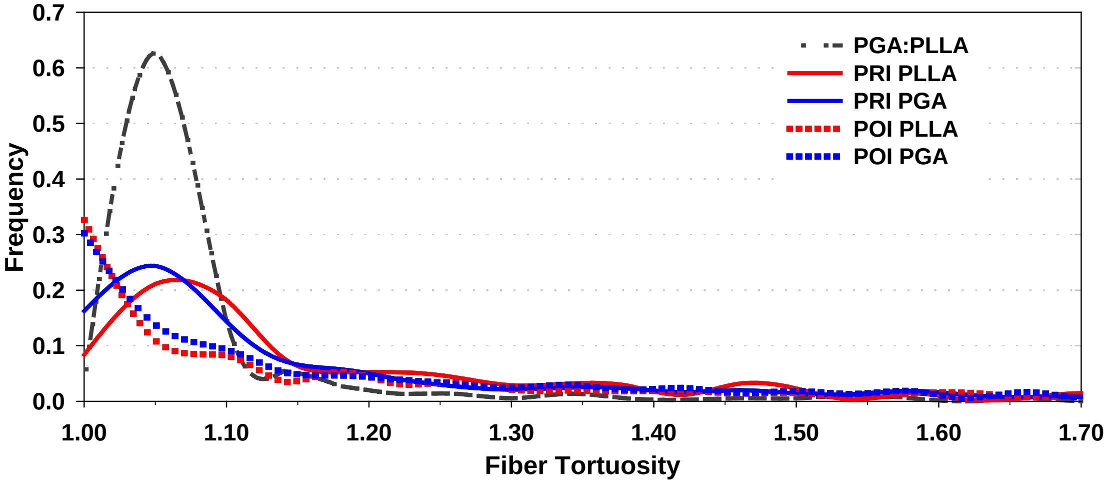

Figure 2.7. Tortuosity histogram for PGA and PLLA in pre-seeded, PRI, and POI specimens.

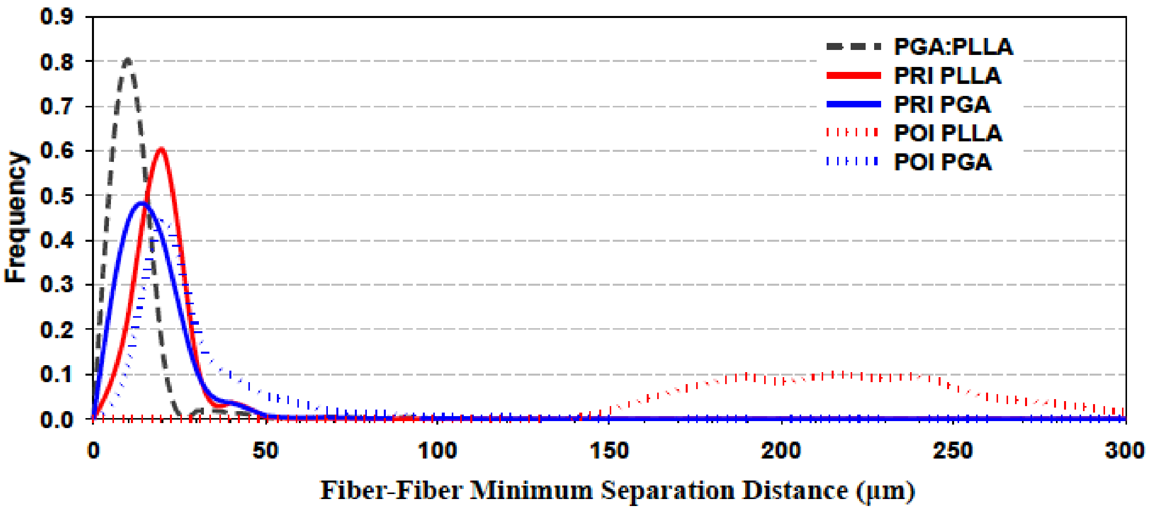

Figure 2.8. Fiber-fiber separation distance histogram for PGA and PLLA in pre-seeded, PRI, and POI specimens.

A reconstruction of the tracked scaffold fibers (Figure 2.9) and a spherical histogram was created (Figure 2.10) showing a strong preferred orientation (red arrow) in the spherical histogram and a noticeable secondary orientation (yellow arrow) orthogonal to the preferred orientation. Qualitatively, this was seen in the scaffold fiber reconstruction. Eigenvalues and associated eigenvectors for the pre-seeded fabric tensor (Table 2.1) corroborated the strong preferred and cross-preferred directions within the scaffold.

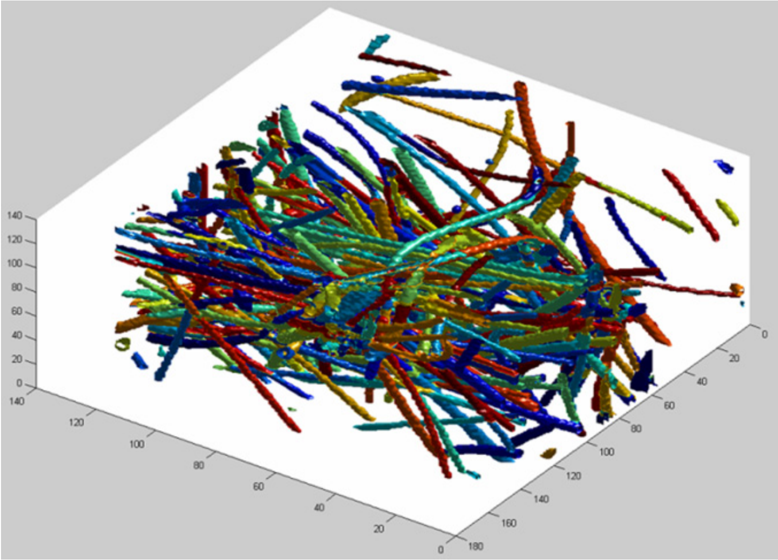

Figure 2.9. 3D reconstructions of pre-seeded PGA:PLLA.

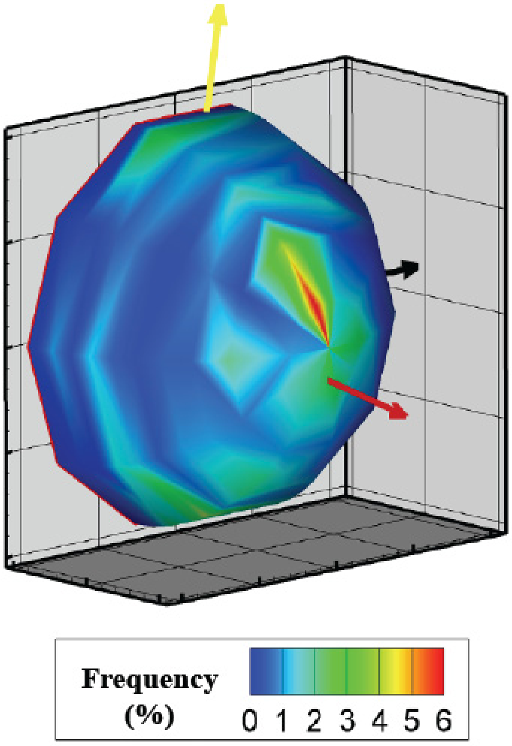

Figure 2.10. Spherical histograms of fiber orientation in the pre-seeded specimen. The red arrow indicates the major principal component (preferred direction) and the black arrow indicates the minor principal component. The yellow arrow indicates the cross-preferred direction.

Table 2.1. Eigenvalues and respective eigenvectors for pre-seeded PGA:PLLA scaffolds as a function of increased sectioning spacing.

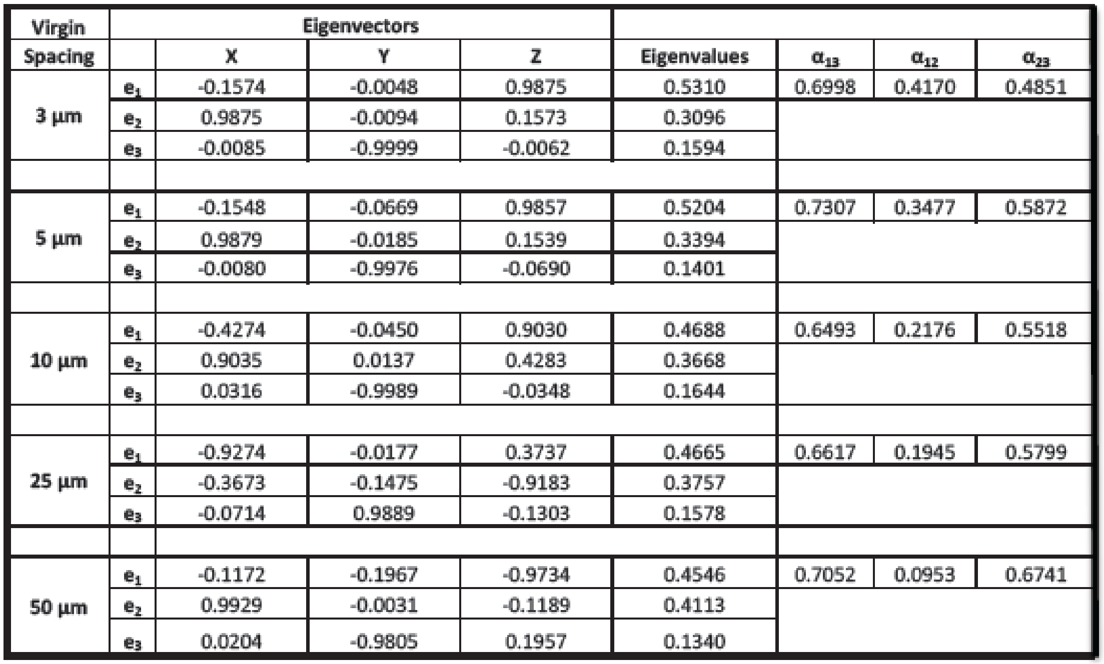

Virgin	Eigenvectors							
Spacing		X	Y	Z	Eigenvalues	α_{13}	α_{12}	α_{23}
3 μm	e_1	-0.1574	-0.0048	0.9875	0.5310	0.6998	0.4170	0.4851
	e_2	0.9875	-0.0094	0.1573	0.3096			
	e_3	-0.0085	-0.9999	-0.0062	0.1594			
5 μm	e_1	-0.1548	-0.0669	0.9857	0.5204	0.7307	0.3477	0.5872
	e_2	0.9879	-0.0185	0.1539	0.3394			
	e_3	-0.0080	-0.9976	-0.0690	0.1401			
10 μm	e_1	-0.4274	-0.0450	0.9030	0.4688	0.6493	0.2176	0.5518
	e_2	0.9035	0.0137	0.4283	0.3668			
	e_3	0.0316	-0.9989	-0.0348	0.1644			
25 μm	e_1	-0.9274	-0.0177	0.3737	0.4665	0.6617	0.1945	0.5799
	e_2	-0.3673	-0.1475	-0.9183	0.3757			
	e_3	-0.0714	0.9889	-0.1303	0.1578			
50 μm	e_1	-0.1172	-0.1967	-0.9734	0.4546	0.7052	0.0953	0.6741
	e_2	0.9929	-0.0031	-0.1189	0.4113			
	e_3	0.0204	-0.9805	0.1957	0.1340			

2.3.3 Pre- and post-implant scaffold analysis

In the PRI and POI specimens, volumes of 731 μm x 989 μm x 339 μm (0.245 mm^3) and 731 μm x 989 μm x 304 μm (0.220 mm^3), respectively, were acquired and analyzed in individual specimens. Qualitatively, specimens showed minimum variation with respect to constituents of interest at different locations with the same specimen and among different specimens. In the full volumes, a total of 1,853 PGA scaffold fibers and 464 PLLA scaffold fibers were identified and tracked in the PRI, and a total of 1,673 PGA scaffold fibers and 2,257 PLLA scaffold fibers were identified and tracked in the POI. Length histograms (Figure 2.11) for both scaffold fiber populations showed a trend towards smaller fibers (both PGA and PLLA) from PRI to POI specimens: PGA and PLLA fibers initially (PRI) demonstrated broad distributions (0-200 µm) and moved to tighter distributions (0-150 µm) in the POI specimen.

Tortuosity showed similar trends between the two groups (Figure 2.7). PGA and PLLA peaks were both shifted (towards 1.00) and larger (increased frequency) in the POI tissue compared to the PRI tissue, suggesting overall straighter fibers in the POI. Minimum scaffold fiber separation histograms were generated for both PRI and POI tissues (Figure 2.8), providing a sense of collagen infiltration between scaffold fibers. In the histogram, it can be seen that PLLA had a peak at 20 µm while PGA had a frequency peak at 10 µm for the PRI tissue; both distributions were broader than the pre-seeded scaffold fiber histogram peak. In the POI tissue, PGA had a peak at 20 µm, and PLLA had an exceptionally broad distribution peak between 190 µm and 240 µm.

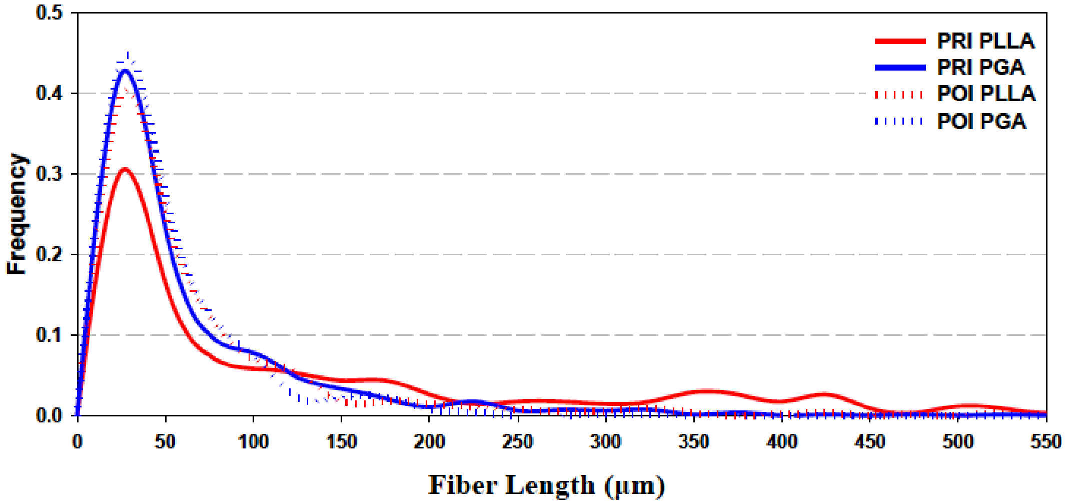

Figure 2.11. Fiber length histograms for PGA and PLLA in PRI and POI specimens.

To verify unique identification of both scaffold fiber populations and to quantify potential bulk erosion, scaffold fiber diameter was investigated. Histograms (Figure 2.12) demonstrated a distinct peak at 12-14 μm for PGA and a broader peak at 28-32 μm for PLLA in the PRI tissue, suggesting unique identification of both scaffold fiber types. In the POI specimen, a distinct peak was seen at 12 μm for PGA and double peaks were seen at 24 μm and 40 μm for the PLLA. Since, as described above, preliminary histology revealed tissue shrinkage around PLLA scaffold fibers, it was necessary to estimate scaffold fiber diameter at both PRI and POI time points to more accurately reflect tissue shrinkage in the scaffold area fraction; the broader diameter histogram peaks and double peak in the POI confirmed shrinkage. It was found that PLLA had a mean +/- standard deviation scaffold fiber diameter of 28.4 μm +/- 3.40 μm at the PRI time point (16 scaffold fibers) and a mean +/- standard deviation scaffold fiber diameter of 30.3 μm +/- 3.84 μm at the POI time point (15 scaffold fibers). With this information, the discrepancies in the diameter histogram for PLLA could be corrected, yielding mean +/- standard deviation area fractions of 3.33% +/- 0.56% (PGA), 6.26% +/- 0.54% (PLLA), and 9.59% +/- 0.54% (PGA:PLLA) in the PRI and mean area fractions of 1.42% +/- 0.79% (PGA), 4.61% +/- 0.79% (PLLA), and 6.03% +/- 1.18% (PGA:PLLA) in the POI (Figure 2.13). In all cases, mean area fractions were significantly different from one another.

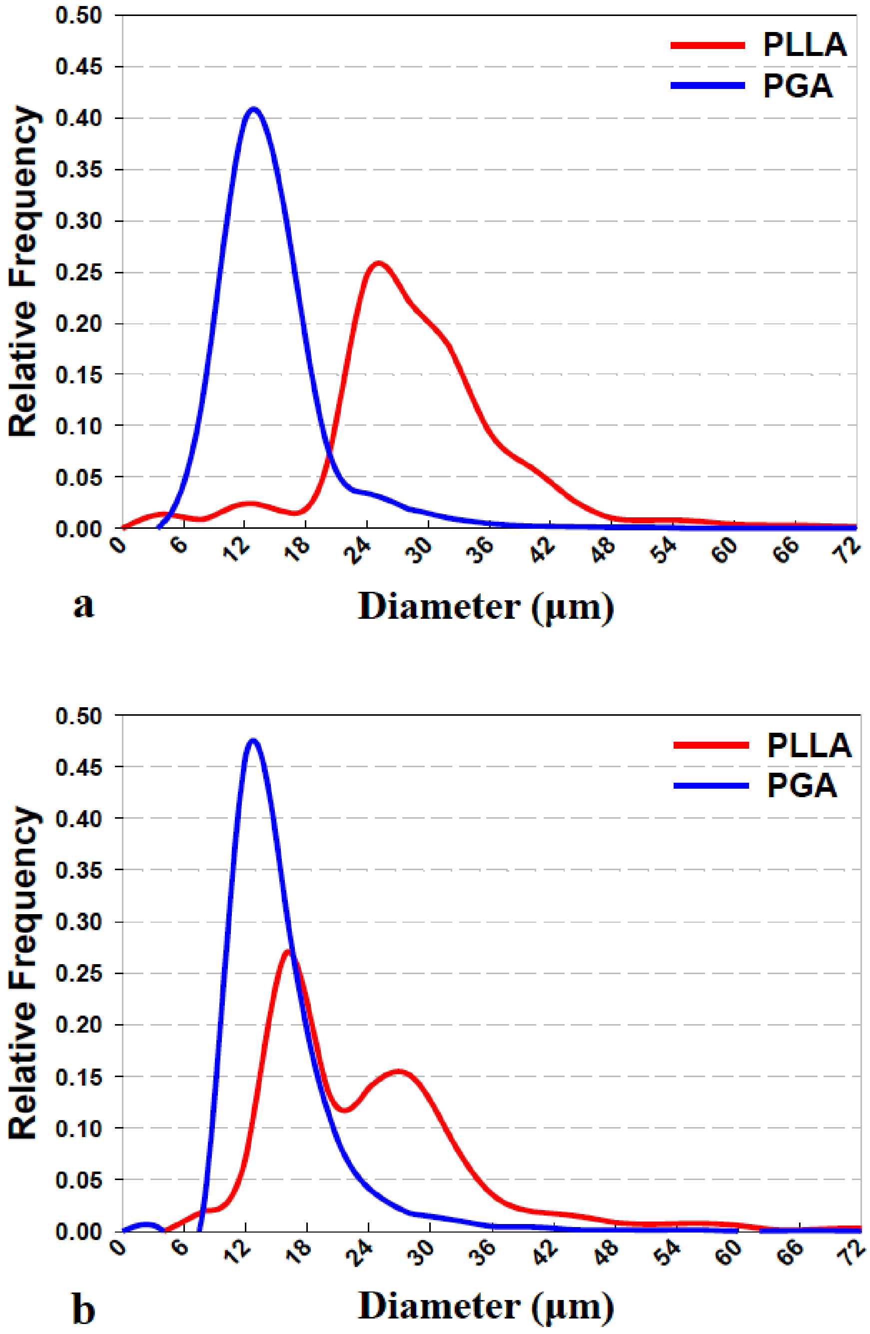

Figure 2.12. Fiber diameter histograms of PGA and PLLA in (a) PRI and (b) POI specimens.

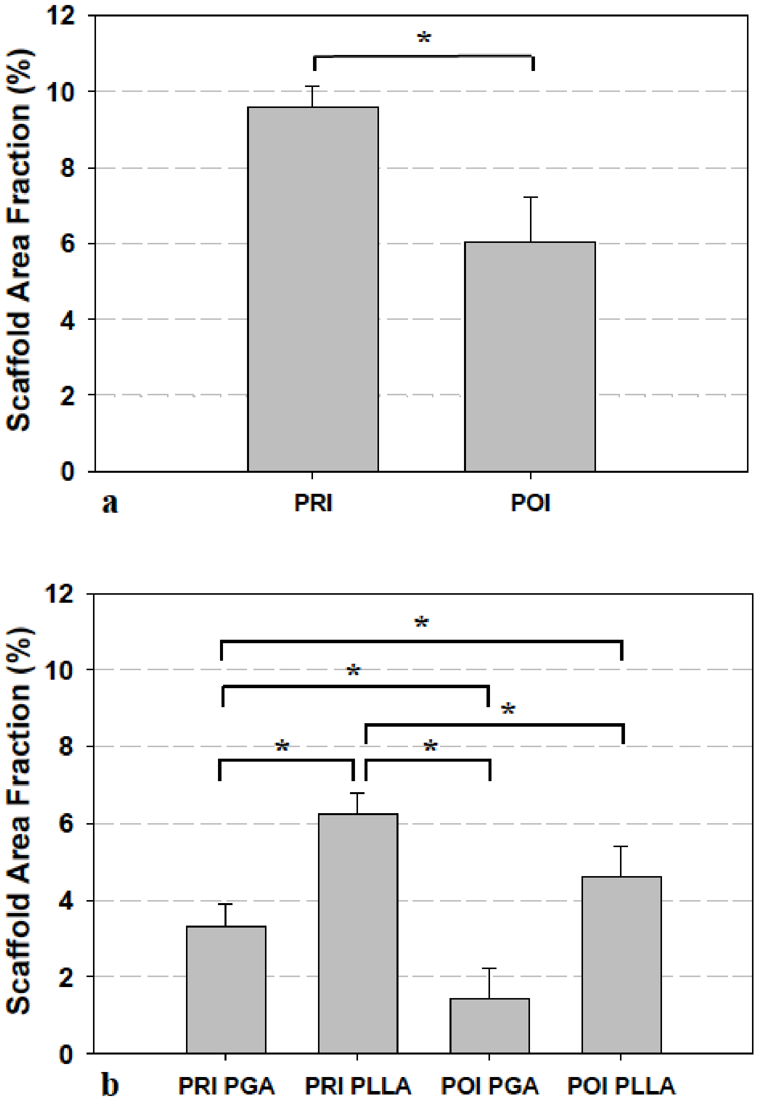

Figure 2.13. Corrected scaffold area fractions for total fibers and separated PGA/PLLA fibers for both PRI and POI specimens. (a) total fibers shown; (b) separated fibers shown. Asterisks indicate statistically significant differences where $p<0.05$.

In the reconstructions of both the PGA and PLLA scaffold fibers in the PRI (Figure 2.14), partial fragmentation was seen in the PGA scaffold fibers but was slightly masked in the PLLA scaffold fiber reconstruction due to tissue-shrinkage around the scaffold fibers. In both scaffold fiber populations, however, the spherical histogram revealed preferred (red arrow) and cross-preferred (yellow arrow) scaffold fiber orientations, though the lower population densities surrounding the directional arrows suggest less distinct orientations than in the pre-seeded specimen. The eigenvalues and respective eigenvectors for both scaffold fiber populations showed similar results (Table 2.2). Decreased anisotropy was seen in the POI spherical histogram (Figure 2.15) as the distribution of scaffold fiber orientations became more random. Eigenvalues and respective eigenvectors for both scaffold fiber populations in the POI specimen reinforced the observations (Table 2.3). Additionally, significant fragmentation was seen in the reconstructions.

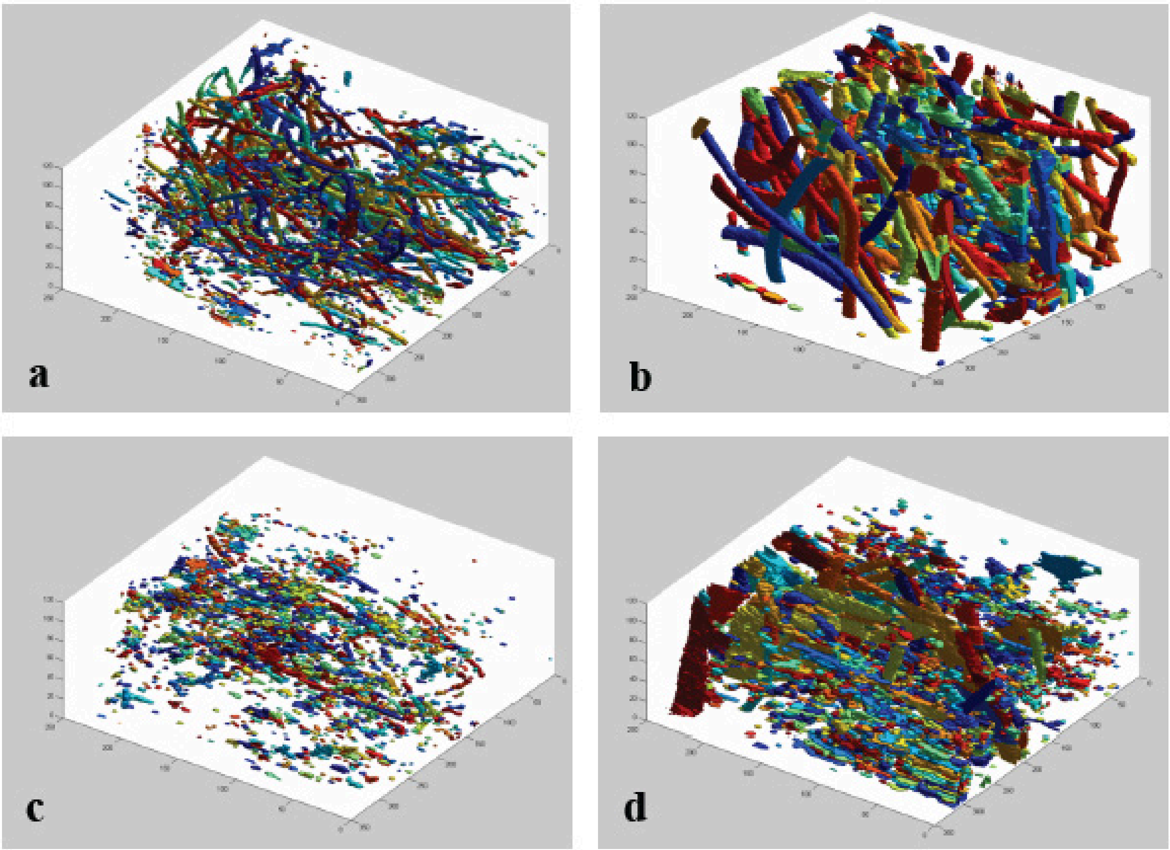

Figure 2.14. 3D reconstructions of PGA and PLLA in PRI and POI. (a) PGA in PRI, (b) PLLA in PRI, (c) PGA in POI, and (d) PLLA in POI.

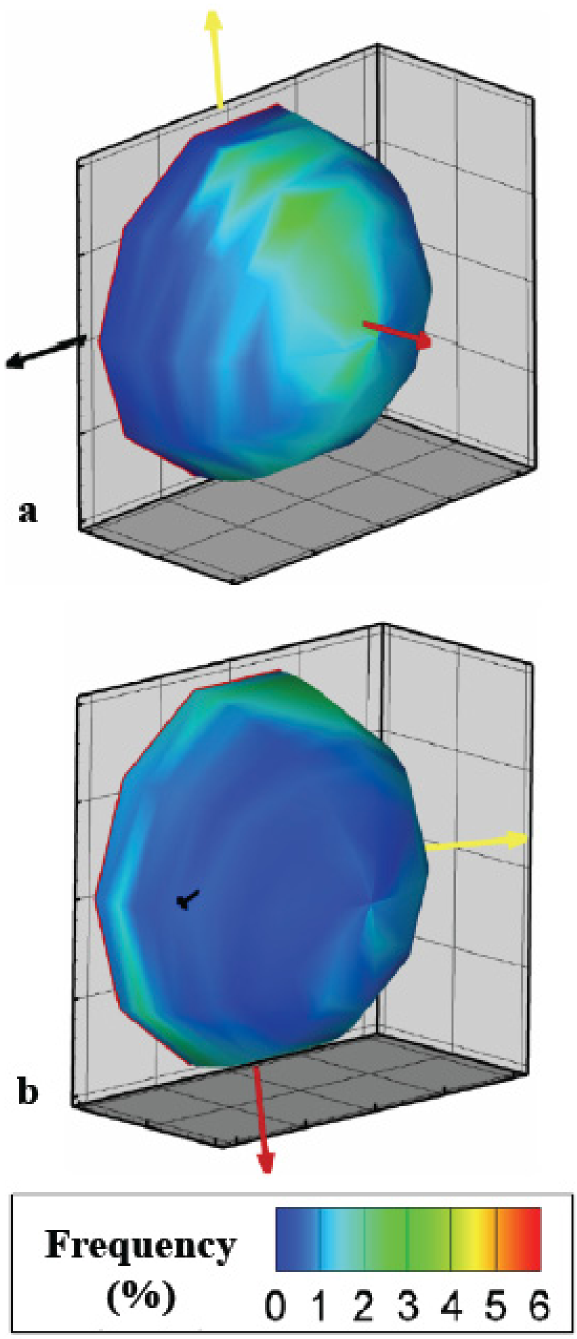

Figure 2.15. Spherical histograms of fiber orientation in the PRI and POI specimens. (a) PRI and (b) POI. The red arrow indicates the major principal component (preferred direction) and the black arrow indicates the minor principal component. The yellow arrow indicates the cross-preferred direction.

Table 2.2. Eigenvalues and respective eigenvectors for PRI specimens as a function of increased sectioning spacing.

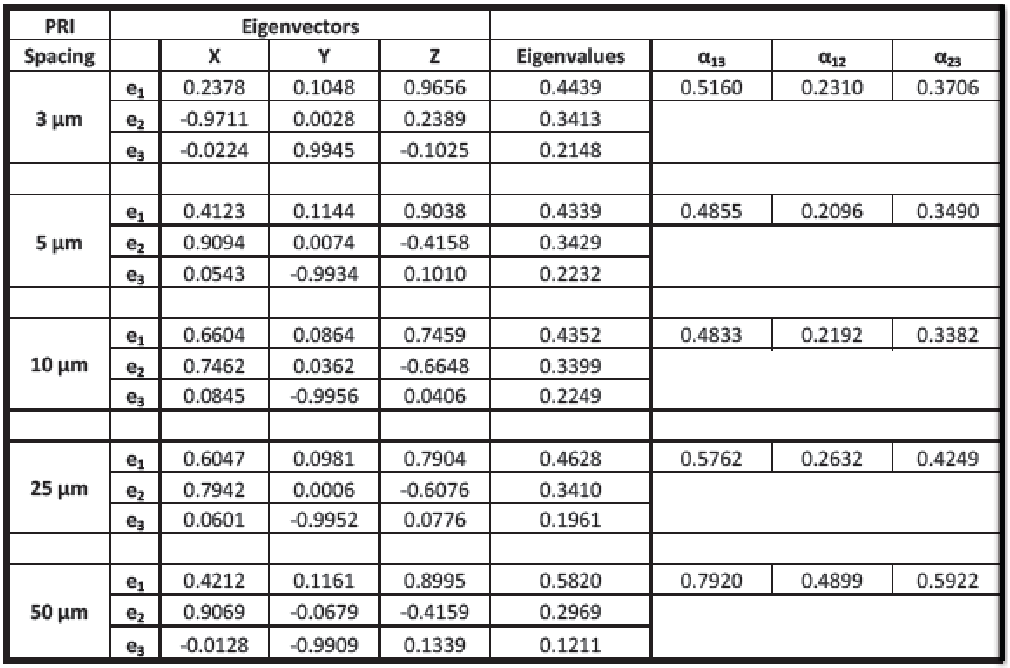

PRI	Eigenvectors							
Spacing		X	Y	Z	Eigenvalues	α_{13}	α_{12}	α_{23}
3 µm	e_1	0.2378	0.1048	0.9656	0.4439	0.5160	0.2310	0.3706
	e_2	-0.9711	0.0028	0.2389	0.3413			
	e_3	-0.0224	0.9945	-0.1025	0.2148			
5 µm	e_1	0.4123	0.1144	0.9038	0.4339	0.4855	0.2096	0.3490
	e_2	0.9094	0.0074	-0.4158	0.3429			
	e_3	0.0543	-0.9934	0.1010	0.2232			
10 µm	e_1	0.6604	0.0864	0.7459	0.4352	0.4833	0.2192	0.3382
	e_2	0.7462	0.0362	-0.6648	0.3399			
	e_3	0.0845	-0.9956	0.0406	0.2249			
25 µm	e_1	0.6047	0.0981	0.7904	0.4628	0.5762	0.2632	0.4249
	e_2	0.7942	0.0006	-0.6076	0.3410			
	e_3	0.0601	-0.9952	0.0776	0.1961			
50 µm	e_1	0.4212	0.1161	0.8995	0.5820	0.7920	0.4899	0.5922
	e_2	0.9069	-0.0679	-0.4159	0.2969			
	e_3	-0.0128	-0.9909	0.1339	0.1211			

Table 2.3. Eigenvalues and respective eigenvectors for POI specimens as a function of increased sectioning spacing.

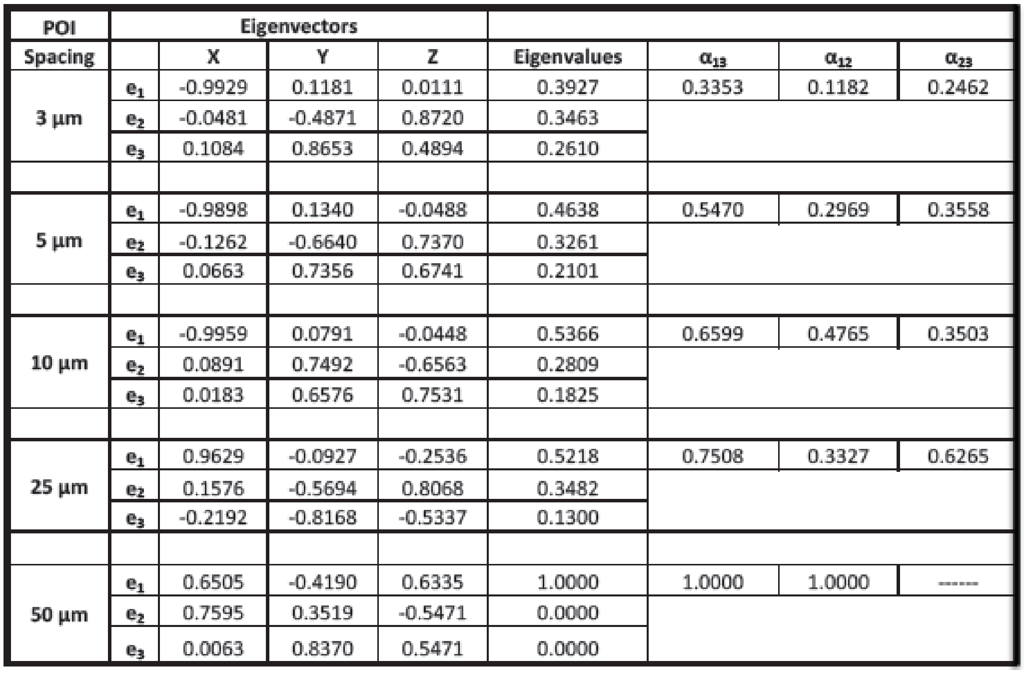

POI	Eigenvectors							
Spacing		X	Y	Z	Eigenvalues	α_{13}	α_{12}	α_{23}
3 µm	e_1	-0.9929	0.1181	0.0111	0.3927	0.3353	0.1182	0.2462
	e_2	-0.0481	-0.4871	0.8720	0.3463			
	e_3	0.1084	0.8653	0.4894	0.2610			
5 µm	e_1	-0.9898	0.1340	-0.0488	0.4638	0.5470	0.2969	0.3558
	e_2	-0.1262	-0.6640	0.7370	0.3261			
	e_3	0.0663	0.7356	0.6741	0.2101			
10 µm	e_1	-0.9959	0.0791	-0.0448	0.5366	0.6599	0.4765	0.3503
	e_2	0.0891	0.7492	-0.6563	0.2809			
	e_3	0.0183	0.6576	0.7531	0.1825			
25 µm	e_1	0.9629	-0.0927	-0.2536	0.5218	0.7508	0.3327	0.6265
	e_2	0.1576	-0.5694	0.8068	0.3482			
	e_3	-0.2192	-0.8168	-0.5337	0.1300			
50 µm	e_1	0.6505	-0.4190	0.6335	1.0000	1.0000	1.0000	------
	e_2	0.7595	0.3519	-0.5471	0.0000			
	e_3	0.0063	0.8370	0.5471	0.0000			

2.3.4 Pre- and post-implant collagen and cell analysis

In the PRI and POI tissues (Figure 2.16), collagen was segmented from the tissues, and 3D reconstructions were created. In the PRI, density profiles along each of the three directions (same as in the native PV) were generated (Figure 2.17). As in the native PV, collagen showed substantial qualitative variability with position in the transmural direction, ranging from 46.0% (central region) to 97.7% (edge regions) and much less variability in the radial (67.8% to 79.0%) and the circumferential (72.7% to 76.3%) directions. In the POI tissue, collagen density profiles in each of the three directions showed similar variability to the PRI tissue in the radial direction (65.9% to 76.1%) and slightly more variability in the circumferential direction (66.9% to 75.2%); in the transmural direction, collagen density varied from 51.2% (central regions) to 94.6% (edge regions), similar to that in the PRI tissue. Cell nuclei could not be segmented from the image data in the PRI and POI tissue due to the strong fluorescence of collagen and scaffold.

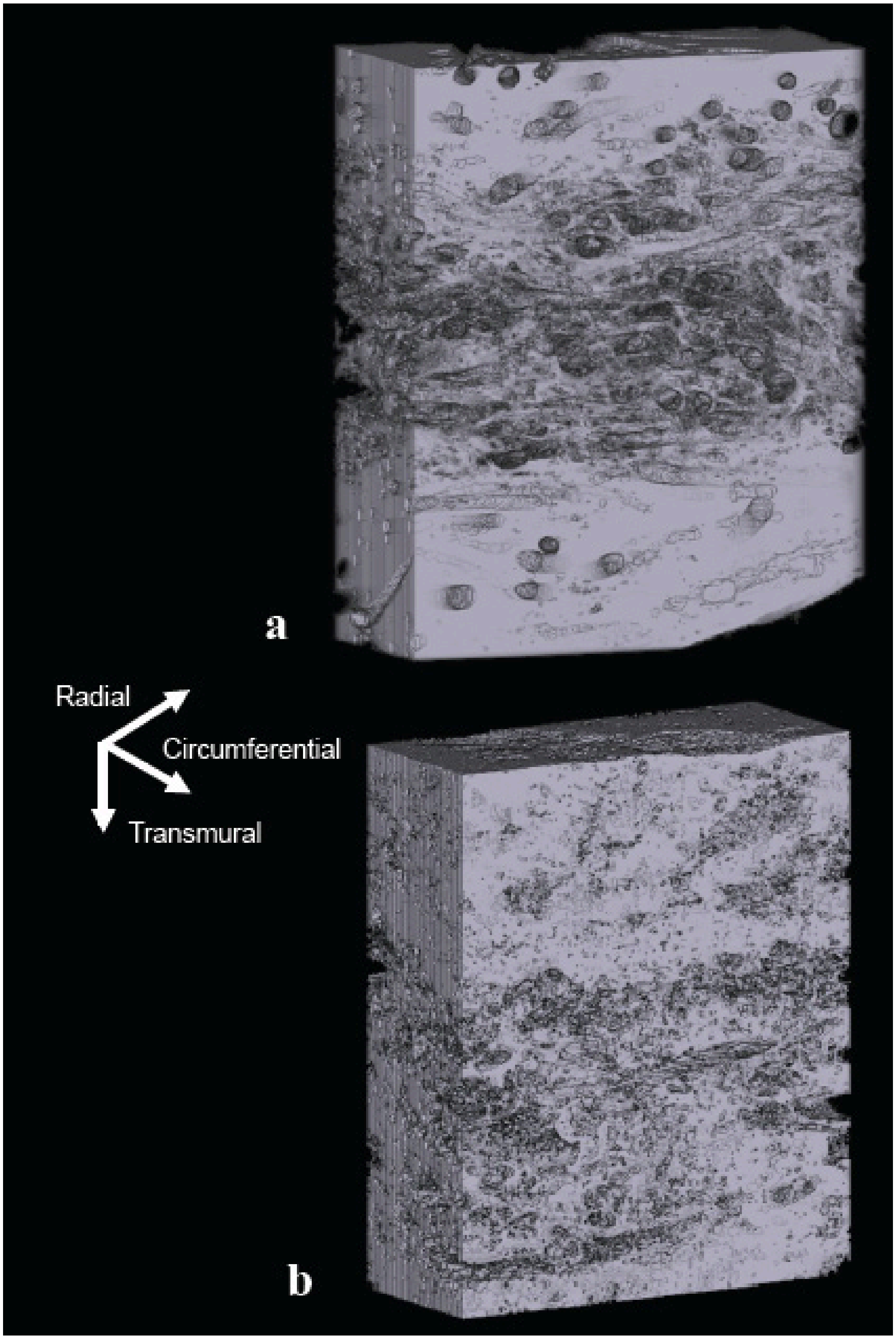

Figure 2.16. 3D reconstructions of collagen in PRI and POI specimens. (a) PRI, (b) POI.

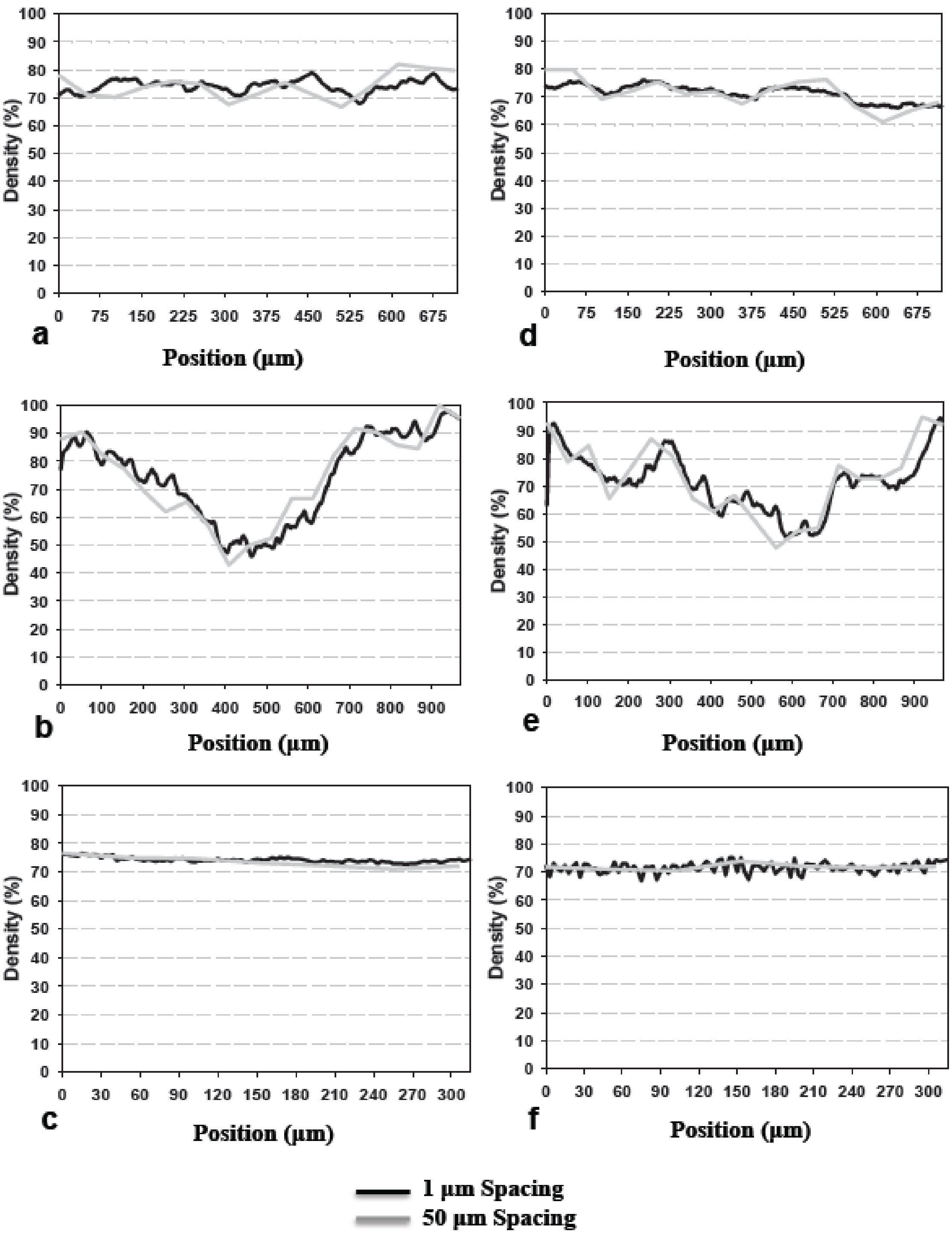

Figure 2.17. Collagen density distributions for PRI and POI. Shown for (a) radial, (b) transmural, (c) and circumferential directions in PRI and (d) radial, (e) transmural, and (f) circumferential directions for POI. Additional plotted lines represent increased sectioning spacing.

2.3.5 Sectioning frequency analysis

Though difficult to quantify specific changes, qualitatively, it was seen that the various layer-specific collagen features evident in the transmural direction of the native PV full data set were preserved through the different sectioning frequencies; minor position-specific collagen densities were also preserved though increased sectioning frequency in the radial direction (Figure 2.3). In the circumferential direction, the mean +/- standard deviation of collagen was found to be 65.9% +/- 2.25% (full), 65.9% +/- 2.27% (2 μm spacing), 65.9% +/- 2.42% (10 μm spacing), 66.1% +/- 2.97% (25 μm spacing), and 66.5% +/- 3.33% (50 μm spacing), indicating little change as a result of sectioning spacing differences in the native PV.

As in the native PV, the PRI and POI tissues demonstrated preservation of similar features in both the radial and transmural directions (Figure 2.17). For the PRI in the circumferential direction, little change was seen in collagen density, with values of 74.2% +/- 0.84% (full 3 μm spacing), 74.1% +/- 0.83% (6 μm spacing), 74.2% +/- 0.91% (9 μm spacing), 73.9% +/- 1.54% (24 μm spacing), and 73.5% +/- 1.95% (51 μm spacing). In the POI circumferential direction, mean +/- standard deviation was nearly constant throughout the sectioning frequency study, with values of 71.8% +/- 1.95% (full 3 μm spacing), 71.9% +/- 1.78% (6 μm spacing), 71.9% +/- 1.88% (9 μm spacing), 71.5% +/- 2.21% (24 μm spacing), and 71.8% +/- 1.07% (51 μm spacing).

The effects of sectioning frequency on the fabric tensor eigenvalues were investigated (Table 2.1, Table 2.2, Table 2.3). In the pre-seeded full data set, α_{13} increased from 0.6998 to 0.7307 when sectioning spacing changed from 3 μm to 5 μm but showed a decrease to 0.7052 up to 50 μm spacing. In a different manner, α_{12} decreased with increased sectioning spacing from 0.4170 (3 μm) to 0.0953 (50 μm); α_{23} showed an increase with increased sectioning spacing from 0.4851 (3 μm) to 0.6741 (50 μm). In the PRI tissue, the scaffold trended differently than the pre-seeded specimen. It was observed that α_{13} steadily increased from 0.5160 (3 μm) to 0.7920 (50 μm), α_{12} remained near 0.2310 (3 μm) for increased sectioning spacing until it jumped to 0.4899 at 50 μm, and α_{23} showed an initial decrease from 0.3706 (3 μm) until 25 μm, where it increased to 0.4249 and ultimately reached 0.5922 at 50 μm (Table 2.2). Finally, the POI tissue showed more pronounced changes with increased sectioning spacing. A substantial increase of α_{13} from 0.3353 (3 μm) to 0.7508 (25 μm) was seen (Table 2.3) before the analysis algorithm was unable to compute unique eigenvectors in e2 and e3 at 50 μm section spacing. Both α_{12} and α_{23} ultimately increased from 0.1182 and 0.2462 respectively (3 μm) to 0.3327 and 0.6265 respectively before approaching indeterminate values at 50 μm section spacing.

2.4 DISCUSSION

A novel imaging methodology and custom morphological software were utilized to obtain high-resolution 3D structural information of EHVT over a large volume. To date, this study represents the most comprehensive large-volume high-resolution structural information of EHVT and is the first known study using long-term in vivo specimens. It is the intent that this structural information serve as the basis for a new structural constitutive model of EHVT better formulated to investigate the mechanical properties of the forming and remodeling tissue phase.

2.4.1 Scaffold fiber architecture

Several important changes in PGA:PLLA non-woven scaffold were revealed in the present study. Importantly, scaffold fibers remained as two morphologically identifiable populations through the PRI and POI specimens, permitting quantification of properties of both the scaffold co-polymer as a whole and individual scaffold fiber types. In the pre-seeded PGA:PLLA scaffold, a continuous scaffold fiber network was clearly evident. The highly skewed and sharply-peaked tortuosity histogram indicates these scaffold fibers are fairly straight with a substantial peak at 1.05, corroborating our previously published values of 1.05-1.10 [9]. Throughout the tissue volume, scaffold area fractions ranged from 5-9%, with a total volume fraction of 7.02%. From the scaffold fiber-fiber separation distance histogram, scaffold fibers are at a minimum within a typical scaffold fiber diameter of each other (peak at 25 μm). Finally, both preferred and cross-preferred orientations exist as previous work confirms [9].

This present work suggests substantial scaffold fiber architectural changes as a function of longer-term implant time. Both scaffold fiber populations show a shift towards lower scaffold fiber lengths which can be explained by scaffold fiber fragmentation through both hydrolysis and, in later in vivo timepoints, macrophage enzymatic degradation processes [23]. With scaffold volume fractions changing from 9.59% (PRI) to 6.03% (POI), scaffold mass is lost over the implant time. Additionally, specific volume fractions of PGA and PLLA scaffold fibers in the POI indicate a similar degradation of both populations (the difference between PRI and POI scaffold fiber volume fractions was similar for both scaffold fiber types). It is interesting to note that despite differences in degradation times (PGA is faster than PLLA [54]) both populations remain discernable at the POI timepoint. Potentially, scaffold fibers could be protected from increased degradation by ECM encapsulation, though further experimentation would be required to prove this hypothesis. Though previous in vitro work has indicated that PGA degrades rapidly during culturing [25, 46], this current work suggests that PGA behaves differently in the presence of PLLA or in an in vivo environment and suggests that both scaffold types should be considered in future modeling efforts of in vivo tissues.

The scaffold fibers undergo a substantial transformation from a slightly tortuous, continuous network (pre-seeded) to a straight, shorter (semi-continuous) network (PRI), ultimately transforming to an exceptionally straight, short fiber scaffold-tissue composite (POI), as indicated by the shifts in the tortuosity histograms observed with POI scaffold fibers having strong near 1.00 and PRI scaffold fibers having tighter distributions at 1.00 and 1.05. Interestingly, the increase in PRI and POI scaffold fiber-fiber separation distances in PGA and PLLA compared to pre-seeded scaffold and the additional increase in scaffold fiber-fiber separation distance between PRI and POI indicates that the scaffold fibers have the potential to interact more independently of one another. Of particular note is the substantially larger minimum separation distance in the POI PLLA scaffold fibers; initially being separated by only 10 μm, PLLA takes on a broader separation distribution in the PRI timepoint with a peak at 20 μm and further separates by nearly an order of magnitude. PGA, however, seems to remain fairly compact, beginning at 10 μm (pre-seeded) and showing a broadened peak at 10 μm (PRI) and a further-broadened peak at 20 μm (POI) extending up to 50 μm. As shown by Engelmayr and Sacks [9], the interbond distance has a profound impact on the overall mechanical properties, exhibiting a non-linear increase in effective stiffness with reduced interbond distance. This current work suggests that the interbond distance remains fairly consistent for PGA from pre-seeded to PRI, with only a slight increase in the POI, while PLLA shows a slight increase from the pre-seeded state to PRI, but with a substantial increase in the POI. Therefore, the interbond distance's effect on the effective stiffness may remain relevant for both scaffold phases in the PRI specimen but only relevant for PGA in the POI specimen.

The qualitative change in scaffold fiber orientation histograms from an aligned network with defined preferred and cross-preferred directions (pre-seeded) to a more isotropic distribution (PRI and POI) implies that the fragmentation, increased scaffold fiber separation, and degradation sufficiently disrupt the original scaffold network to greatly change scaffold fiber alignment. In all, it is apparent that the scaffold undergoes substantial changes from its initial state through the in vitro phase and further changes after implantation.

2.4.2 Collagen and cell content

As the major tissue structural component of EHVT, the importance of collagen in forming tissues dictates the success of the overall implant. As shown by Engelmayr [23], knowledge of collagen densities and distributions is foundational to appropriately modeling such tissue composites, notably when these distributions are heterogeneous and position-dependent. In the native PV, the layer-specific differences known to exist in these valves were illustrated using EV-SLCM and the developed analysis techniques [28]. Further, a mean collagen area fraction of 65.9% was found, corroborating well with previously published data on valve collagen content [55]. Cells were tracked and counted for the native PV; over the analyzed sub volume, 2,363 cells were identified, yielding a cell density of 2.33 x10^5 cells/mm^3 and corroborating with previously published data [56]. Distributions of cell nuclei (qualitative assessment of cell density) varied slightly in the transmural and radial directions though remained constant in the circumferential direction. This intuitively makes sense with the collagen distribution, as matching layer-specific cellular distributions could impact layer-specific collagen content.

Published data on layer-specific valvular interstitial cell densities qualitatively reflects our findings of transmural cellular densities, with the fibrosa and ventricularis layers showing larger (two to three times larger) cellular densities than the spongiosa layer [57].

In both of the PRI and POI tissues, the mean collagen density in the circumferential direction (least section-to-section variability) was larger than in the native PV (65.9%), with PRI (74.2%) slightly larger than POI (71.5%). Qualitatively, this pattern follows that which was previously observed by Hoerstrup et al. [58] where EHVT in vitro tissue showed an increase in collagen content over native valve collagen content and a decrease after in vivo implantation for an extended period of time. One possible reason for the difference between native PV and the EHVT is the presence of non-staining constituents in the native PV such as elastin and glycosaminoglycans (GAGs). It is well known that native valvular tissue contains these constituents in addition to collagen, and though studies have shown the ability to produce such constituents in EHVT [58], densities may be lower than in native PV. Despite their potential presence in the EHVT, it may be at lesser amounts compared to the native PV. It is interesting to note that the POI scaffold phase decreased compared to the PRI scaffold phase, though collagen density showed a decrease between the groups. A plausible explanation could be that as the POI tissue experienced physiological forces compared to the PRI tissue, mechanical stimulation could have influenced the difference in constituent density, though further histological studies specifically investigating elastin and GAGs could help support this. Finally, we noted that variations between PRI and POI tissue collagen density distributions are evident. In the PRI tissue, collagen density varied from 46.0% to 97.7%, while the POI tissue varied from 51.2% to 94.6%. This implies that collagen may move towards a move homogenous distribution with extended in vivo physiological conditions (as opposed to short in vitro static conditions as in the

PRI tissue). Previously, Engelmayr and Sacks [23] highlighted the importance of flexural mechanical stimulation on forming more homogenous transmural collagen distributions, which are consistent with the current results.

2.4.3 Sectioning frequency

Though the EV-SLCM technique provides novel high-resolution 3D structural information, its widespread use is not practical due to the large acquisition time for even a reasonably sized volume. Sands et al. have previously estimated the acquisition time of a 3 mm^3 volume to be nearly an entire twenty-four hour period [46]. It is possible however to use the full resolution information to determine the minimum sectioning frequency necessary to obtain salient structural information. In this study, the effects of sectioning frequency on scaffold fiber orientation (through the fabric tensor) and on collagen distribution were investigated by varying the number of 2D image planes used in the analyses. In the scaffold fiber analysis, the anisotropy index was introduced as a means to evaluate changes in computed scaffold fiber orientation. Since each of the full-resolution data sets (pre-seeded, PRI, POI) showed distinct specific scaffold fiber orientations (ranging from highly anisotropic to isotropic), the point at which sectioning frequency began to significantly alter scaffold fiber orientation could represent the minimum sectioning frequency for that particular tissue.

In the pre-seeded specimen, a preferred orientation existed up to 50 μm section spacing, though the distinction between directions began to disappear by 10 μm section spacing. Though at first glance this appears detrimental to future structural-based modeling efforts, the PRI tissue shows much less change as a function of sectioning spacing: in these tissues, a preferred direction exists (though not as strongly in the pre-seeded specimen) while a cross-preferred direction is not as evident, but even up to 25 μm section spacing, this structural configuration remains. At 50 μm section spacing, this appears to break down as increased anisotropy is introduced in the scaffold fiber population.

In the POI specimen, increased section spacing introduces more anisotropy to an initially fairly isotropic system. At the initial section spacing of 3 μm, all three anisotropy indices are small and similar to one another indicating an isotropic orientation. By 10 μm section spacing, the indices of two directions increases, implying a false anisotropy. A potential cause is the limited scaffold fiber length; sectioning the volume at spacings larger than the scaffold fiber length itself could prevent inaccurate computations of the fabric tensor. At 50 μm, this is evident as only one unique eigenvalue could be computed. One potential solution involves sectioning with the majority of scaffold fibers parallel to the sectioning plane, though this may decrease the number of scaffold fibers that can be captured in a single section. A better solution may involve using the full-resolution information to guide structural assumptions; since scaffold at the POI timepoint exist as randomly-distributed, short, straight scaffold fibers, efforts to utilize the structural information can be greatly simplified. The structural information necessary for PRI timepoint tissues may not be relevant at this later timepoint, suggesting that only basic volume-fraction information may be sufficient.

In the native PV, the tissue circumferential direction provided the least variation in collagen density on a section-by-section basis. Keeping the radial and transmural directions in plane with respect to the sections could preserve the greatest amount of position-specific collagen density information. A mean collagen area fraction of 65.9% was computed for the full data set (1 μm spacing). Increasing sectioning spacing up to 25 μm had only a 0.2% change in mean collagen area fraction; increasing sectioning spacing to 50 μm resulting in a 0.6%

difference. By maintaining full-resolution sections in plane with the radial and transmural directions, the collagen distribution could be maintained with minor variations in overall collagen content up to 50 μm of sectioning spacing (in the circumferential direction).

Important for future EHVT structural analyses, the variability in the circumferential direction in both PRI and POI tissues varied little with sectioning frequency, as in the native PV. Mean collagen densities of 74.2% (PRI) and 71.8% (POI) changed to 73.9% (PRI) and 71.5% (POI) at 24 μm sectioning spacing and to 73.5% (PRI) and 71.8% (POI) at 51 μm sectioning spacing. It is evident that even at 51 μm sectioning spacing both data sets showed minimal variation in mean collagen densities compared to respective full resolution data sets. Though the features in the other two directions (notably the transmural direction) showed distinct position-specific variability in collagen density, increasing sectioning frequency had minimal impact on the overall qualitative density distributions. Sectioning in the circumferential direction will provide sufficiently similar collagen density profiles up to 50 μm and should be used for future structural studies.

2.4.4 Implications for modeling ECM formation

In order to evaluate the mechanical quality of formed tissue, it is essential to predict the ECM phase mechanical properties from the overall composite response. Previous modeling efforts in our laboratory have resulted in a descriptive mechanical model for intact needle non-woven scaffolds that predicted pre-seeded scaffold stiffness [9]. When applied to tissue-scaffold composites using the rule of mixtures, however, the model was not able to account for the observed large increases in stiffness; composite stiffness values were much lower than what the model predicted. As a result, a new model was proposed based on a measured collagen distribution and a scaffold-ECM coupling factor [23]. Though sufficient as first effort, the meso-scale composite model relies heavily on an empirically determined coupling factor. Additionally, these models assume static scaffold conditions, i.e. scaffold fibers that morphologically remain the same throughout tissue accretion and subsequent remodeling. The current work indicated that the scaffold undergoes substantial modification, primarily by fragmentation and orientation changes, throughout in vitro and in vivo phases. Specifically, scaffold fibers that initially formed a fairly compact and continuous network in a preferred orientation showed substantial degradation and take on a more isotropic, discontinuous, and spread architecture. Interestingly, both PLLA and PGA remained in the PRI and POI specimens. Further, in comparing the in vitro and in vivo phases, it appears that collagen becomes more homogenously distributed throughout the volume after implantation. These morphological changes must be considered in the next-generation modeling efforts to more accurately estimate the mechanical properties of forming and remodeling EHVTs and TECs.

2.4.5 Further applications

The imaging technique presented in this work is an extension of previous work conducted at the University of Auckland [25, 46]. Of particular interest is the means to utilize the acquired high-resolution 3D information and quantitatively analyze to yield particular morphological metrics of interest. Such imaging and analysis techniques have value both latitudinally within EHVT efforts and longitudinally within general tissue morphological studies. These techniques could be applied to any collagenous tissue where relative distributions are of interest. Similarly, the techniques presented could be used to quantify scaffold structures at a variety of different states (i.e. non-seeded, in vitro culturing, etc.).

2.4.6 Limitations

Overall, use of the EV-SLCM system eliminated many of the errors introduced by traditional imaging techniques, and its use for engineered tissue scaffolds has not been previously published. Therefore, the lack of prior published data may bring into question the validity of the experimental results. We feel, however, that the close corroboration of morphological parameters (tortuosity, volume fraction, and diameter) determined from this work to those parameters previously published using alternative techniques strengthens our results. Additionally, the use of isolated pre-seeded PGA and pre-seeded PLLA show the ability of our techniques to distinguish both scaffold fiber populations. Histological support for correct scaffold fiber identification has been essential to this work and helps confirm our segmentation techniques for the PRI and POI specimens.

Additionally, it should be noted that this study was intended to provide information on ECM formation in the bulk sense. As a result, quantifying individual collagen fibers and cells were not part of the study design. However, with the completion of this current study, important experimental details such as imaging resolution and staining protocol have been established to permit the future quantification of these metrics. Moreover, future studies into quantifying individual collagen fibers and cellular densities are been planned.

The inability of the automated segmentation techniques to consistently identify PLLA boundaries from the voids created through tissue shrinkage also introduced some error, though we feel this error relates primarily to scaffold fiber diameter and resultant area fraction computations rather than centroid measurement and resultant length, tortuosity, and orientation. We feel that the correlation of average PLLA scaffold fiber diameter measured from histology to that of the segmented PLLA scaffold fiber diameter provided an adequate means to correct tissue shrinkage-effects on segmentation. Finally, due to the time intensive nature of the technique we were only able to study a limited number of specimens. However, conventional histological images [45] supported a good degree of consistency in the POI specimens, so that the current results should be representative.

2.5 SUMMARY

The present study provides novel insight into the time evolution of 3D structure of EHVT at the in vitro and in vivo phases and will help guide the development of improved constitutive models to estimate the tissue mechanical response from similar tissue-scaffold composites such as TECs. It is evident that both the scaffold fiber phase and the collagen phase of the tissue-scaffold composites undergo substantial structural changes from a pre-seeded scaffold state to a post-explant state. Specifically, the scaffold fibers changed from a slightly tortuous, fairly continuous, and oriented population (PRI) to a straight, short, randomly oriented population (POI) with PGA and PLLA scaffold fiber populations both existing in the PRI and POI specimens. The collagen density was observed to approach a slightly more homogenous transmural distribution in the POI compared to the PRI. Additionally, it was shown that future 2D histological studies would benefit most from transmural sectioning with spacings no greater than 25 μm for scaffold morphology and 50 μm for collagen density.

3.0 DEVELOPMENT OF GENERALIZED LARGE DEFORMATION STRUCTURAL CONSITUTIVE MODELS FOR FORMING AND REMODELING TISSUE IN SCAFFOLD-ECM COMPOSITES

3.1 INTRODUCTION

In order to evaluate the mechanical quality of formed tissue, it is essential to predict the ECM phase mechanical properties from the overall composite response. Without a proper formulation, it is impossible to know, in a quantitative sense, to what degree the measured mechanical response is influenced by the remaining scaffold component. Previous modeling efforts [9, 23] have resulted in a descriptive mechanical model for intact needle non-woven (NNW) scaffolds undergoing flexure that predicted virgin scaffold stiffness for engineered heart valve tissues. When applied to tissue-scaffold composites using the rule of mixtures, however, the model was not able to account for the observed increases in stiffness of the composite and substantially underestimated the predicted composite stiffness compared to the experimentally measured values. As a result, a new model was proposed based on a measured collagen distribution and a scaffold-ECM coupling factor [23]. Though sufficient as first efforts, both models are restricted to small deformations, and the meso-scale composite model relies heavily on an empirically determined coupling factor to account for observed scaffold-ECM interactions. Structural insight, as shown in chapter 2, suggests that upon completion of a three-week in vitro culturing period, the scaffold undergoes change with indications of reduced volume fraction. Further, after extended in vivo durations, the scaffold becomes highly fragmented and discontinuous. Both previous model formulations do not account for such scaffold changes and may ultimately underestimate tissue properties.

In this work, the aim is to develop two structural mathematical models, distinguished by continuity of the scaffold phase, to separate the constituent mechanical contributions and enable estimation of tissue mechanical properties. A theoretical basis with key assumptions will be provided for each model form. As it is important that these models can be applied to other scaffold systems, it is necessary that the framework be as general as possible to provide the greatest degree of flexibility and applicability.

3.2 MATHEMATICAL MODELING PRELIMINARIES

3.2.1 The need for finite nonlinear elasticity

In a general sense, constitutive equations are functional relationships between stress components and other field functions such as strain and temperature in a material [59]. The use of such relationships is to approximate the observed real behavior of materials under particular conditions. Within the biological/bioengineering literature, the highly nonlinear, pseudoelastic, and anisotropic nature of soft tissues under normal physiological conditions has been well established for a variety of tissue types [60]. Additionally, it has been observed that such tissues are not limited to small deformations but experience large deformations during normal function. As such, the simplification of traditional infinitesimal linear strain theory in constitutive model formulation is not appropriate for these tissues. Since the goal of tissue engineering is to restore native functionality of tissues via engineered constructs, it is worthwhile to develop models that can accommodate such tissue responses. In the following sections, descriptions of stress and strain in this body of work will be defined, and the theoretical basis for the overall model framework will be provided.

3.2.2 Stress and strain relations

Since nomenclature often varies when dealing with material properties, it is necessary to establish consistent terminology to be used through the entirety of this work when describing stress and strain. For consistency in this dissertation, all scalars are represented by lowercase Latin letters (a), vectors as lowercase bold Latin letters (**a**), and tensors as uppercase bold Latin letters (**A**). Subscript indices will denote Cartesian components of the vector or tensor.

If a vector **x** represents the position of a point P in a starting (reference) configuration and $\mathbf{x}'$ the position of that same material point in the deformed configuration, the deformation gradient tensor **F** can be used to describe the transformation of a line segment $\mathrm{d}\mathbf{x}$ to $\mathrm{d}\mathbf{x}'$ as $\mathrm{d}\mathbf{x}' = \mathbf{F}\mathrm{d}\mathbf{x}$ or as $\mathbf{F} = \nabla\mathbf{x}$ where ∇ denotes the partial derivative of the vector **x**. Note that the determinant of the deformation gradient represents a change in an infinitesimal volume element as $\mathrm{J} = \det(\mathbf{F})$.

Since **F** contains rigid body motions, alternative deformation-based measures of strain are often utilized. The Right Cauchy-Green tensor **C**, the Left Cauchy-Green tensor **B**, and the Green-Lagrange (or Green’s strain) tensor **E** are defined as

$$\mathbf{C} = \mathbf{F}^{\mathrm{T}}\mathbf{F}, \tag{3.1}$$

$$\mathbf{B} = \mathbf{F}\mathbf{F}^{\mathrm{T}}, \tag{3.2}$$

$$\mathbf{E} = \tfrac{1}{2}\left(\mathbf{C} - \mathbf{I}\right), \tag{3.3}$$

where **I** is the identity tensor.

In continuum mechanics, stress is responsible for the deformation of bodies. When describing stress, the forces acting on a surface can be related to the surface normal **n** as the traction vector **t**. The Cauchy stress tensor $\boldsymbol{\sigma}$ can then be defined as relating the normal vector **n** to the traction vector **t** acting on a body's surfaces and defined in the deformed configuration. As $\mathbf{t} = \boldsymbol{\sigma}\mathbf{n}$. Alternatively, the Lagrangian or 1st Piola-Kirchhoff stress tensor **P** can be defined in the reference configuration and is related to the Cauchy stress tensor as $\mathbf{P} = \mathrm{J}\mathbf{F}^{-1}\boldsymbol{\sigma}$. The first Piola-Kirchhoff tensor is not symmetric, so another stress measure, the second Piola-Kirchhoff stress tensor **S** is often used in computational mechanics due to its symmetry. It can be related to the Cauchy stress tensor as $\mathbf{S} = \mathrm{J}\mathbf{F}^{-1}\boldsymbol{\sigma}\mathbf{F}^{-\mathrm{T}}$. The relation between these three stress measurements can be summarized as

$$\mathbf{P} = \mathrm{J}\mathbf{F}^{-1}\boldsymbol{\sigma} = \mathrm{J}\mathbf{F}^{-\mathrm{T}}, \tag{3.4}$$

$$\mathbf{S} = \mathrm{J}\mathbf{F}^{-1}\boldsymbol{\sigma}\mathbf{F}^{-\mathrm{T}}, \tag{3.5}$$

$$\mathbf{P} = \mathbf{F}\mathbf{S} = \mathbf{S}\mathbf{F}^{-\mathrm{T}}, \tag{3.6}$$

$$\mathbf{S} = \mathbf{F}^{-1}\mathbf{P} = \mathbf{P}\mathbf{F}^{-\mathrm{T}}. \tag{3.7}$$

3.2.3 Internal work

Assuming purely mechanical contributions (i.e. no contributions from chemical or thermal sources), it is possible to determine the internal work done by the stresses as

$$\mathrm{dW}_{\mathrm{int}} = \int_{\mathrm{v}} \mathrm{tr}\left(\boldsymbol{\sigma}^{\mathrm{T}}\partial\mathbf{d}\right)\mathrm{dv}, \tag{3.8}$$

where the tensor operator tr denotes the trace and **d** is the rate of deformation tensor which is the symmetric part of the velocity gradient tensor **L** defined as

$$\mathbf{L} = \dot{\mathbf{F}}\mathbf{F}^{-1}, \tag{3.9}$$

with $\dot{\mathbf{F}} = \partial \mathbf{F} / \partial t$ where t is time. For completeness, it should be noted that the Green's strain tensor $\dot{\mathbf{E}}$ can be related to **d** as

$$\mathbf{d} = \mathbf{F}^{-T}\dot{\mathbf{E}}\mathbf{F}^{-1}. \tag{3.10}$$

Rearranging eq. (3.8) based on eq. (3.4) or eq. (3.6) and eq. (3.10), it is possible to define the internal work based on the first Piola-Kirchhoff stress and rate of deformation gradient as

$$W_{int} = \mathrm{tr}\left(\mathbf{P}^{T}\dot{\mathbf{F}}\right), \tag{3.11}$$

or the second Piola-Kirchhoff stress and rate of Green's strain tensor as

$$W_{int} = \mathrm{tr}\left(\mathbf{S}^{T}\dot{\mathbf{E}}\right). \tag{3.12}$$

It should be noted that both **P** and $\dot{\mathbf{F}}$ and **S** and $\dot{\mathbf{E}}$ are known as work conjugates.

3.2.4 Hyperelasticity

In constitutive models for materials displaying nonlinear finite deformations, a hyperelastic approach is often taken. Whereas constitutive relations in elastic materials are generally only a function of the current state of deformations, constitutive relations in hyperelastic materials are dependent on the initial and final configures and are said to be path-independent [59]. As a result, a relationship describing the work done by the stresses from an initial to final configuration can be established known as a *stored strain energy function* or *elastic potential* Ψ per unit undeformed volume. This relationship is based on work conjugate pairs, as described in eq. (3.11) and eq. (3.12). In the case of first Piola-Kirchhoff stress, this takes the form

$$\dot{\Psi} = \mathrm{tr}\left(\mathbf{P}^{T}\dot{\mathbf{F}}\right). \tag{3.13}$$

Rearranging yields the relationship

$$\mathbf{P} = \frac{\partial \Psi\left(\mathbf{F}\right)}{\partial \mathbf{F}}\ . \tag{3.14}$$

It should be noted that rotation does not contribute to the strain energy and thus only depends on the stretch component and so $\Psi\left(\mathbf{F}\right) = \Psi\left(\mathbf{C}\right)$. Thus, eq. (3.13) can further be expressed as a function of **C** as

$$\dot{\Psi} = \mathrm{tr}\left(\left(\frac{\partial \Psi}{\partial \mathbf{C}}\right)^{\mathrm{T}} \dot{\mathbf{C}}\right), \tag{3.15}$$

based on eq.(3.1) and using eq. (3.3) to arrive at $\tfrac{1}{2}\dot{\mathbf{C}} = \dot{\mathbf{E}}$. Since it has been shown that **S** and $\dot{\mathbf{E}}$ are work conjugates, eq. (3.15) can be expressed as

$$\dot{\Psi} = \mathrm{tr}\left(\tfrac{1}{2}\mathbf{S}^{\mathrm{T}}\dot{\mathbf{C}}\right), \tag{3.16}$$

which leads to eq. (3.14) being changed to

$$\mathbf{S} = 2\frac{\partial \Psi}{\partial \mathbf{C}} = \frac{\partial \Psi}{\partial \mathbf{E}}\ . \tag{3.17}$$

Hence, the strain energy function can be expressed in terms of second Piola-Kirchhoff stress and the Green’s strain tensor.

Due to the large amount of water found in soft tissues, the constraint of incompressibility ($J = 1$) is often imposed [60]; this results in an additional term in the strain energy relationship, yielding

$$\mathbf{S} = \frac{\partial \boldsymbol{\Psi}}{\partial \mathbf{E}} - p\mathbf{C}^{-1}, \tag{3.18}$$

where p is the Lagrange multiplier that enforces incompressibility.

Often, strain energy functions are formulated in terms of principal invariants so that the relationship between Ψ and **C** or **E** is independent of the initial axes. In this current work, five invariants are used, defined as

$$\mathrm{I}_1 = \mathrm{tr}(\mathbf{C}),\ \mathrm{I}_2 = \tfrac{1}{2}\left[\left\{\mathrm{tr}(\mathbf{C})\right\}^2 - \mathrm{tr}(\mathbf{C}^2)\right],\ \mathrm{I}_3 = \det(\mathbf{C})$$

$$\mathrm{I}_4 = \mathbf{a}_0\mathbf{C}\mathbf{a}_0, \text{ and } \mathrm{I}_5 = \mathbf{a}_0\mathrm{C}^2\mathbf{a}_0. \tag{3.19}$$

3.3 THEORETICAL FRAMEWORK OF CONTINUOUS SCAFFOLD MODEL

3.3.1 Previous continuous scaffold modeling efforts

As stated in chapter 1, previous modeling efforts for continuous NNW scaffolds have been presented by Engelmayr and Sacks [9, 23]. In the first model, flexural mode deformations were considered, and the model successfully predicted mechanical properties of PGA, PLLA, and PGA:PLLA blended scaffolds within an infinitesimal strain context. This study showed that depositions on the scaffold increased the stiffness through increased fiber-fiber bond points and that this increase did not follow a simple rule of mixtures [9]. As a next step, an extension of this model combined the individual flexural rigidities of ECM and virgin scaffold along with a coupling factor to describe the flexural rigidity of tissue-scaffold composites [9, 23]. An important finding in this work was that mechanical stimulation increased both the mass of collagen produced as well as the intrinsic stiffness of the collagen (collagen quality). Although the scaffold component of the model was based on its microstructure, changes to the scaffold with implant duration were not considered (i.e. changes to volume fraction or continuity). Mechanical evaluation of the tissue phase was limited to an instantaneous linear elastic modulus value based on Euler-Bernoulli beam bending and lacked applicability to a large deformation context. Additionally, the model was limited to flexure-based deformations and could not be generalized for use with other deformation modalities (such as biaxial tension or dilation).

3.3.2 Assumptions in proposed continuous scaffold model

The NNW and meso-scale tissue-scaffold models provided an important base to describe scaffold mechanical properties and to predict ECM mechanical properties; however, restriction to a small deformations severely limits the application of the models to potential larger strain in the NNW and future scaffold materials exhibiting increased compliance (i.e. poly(ester urethane) urea (PEUU)). Additionally, the time course effects of scaffold modification such as fragmentation and orientation changes are not accommodated in either model formulation. Based on these limitations and the structural analyses described in chapter 2, a new model is proposed with these assumptions:

I. The strain energies of the scaffold, ECM, and scaffold-ECM interactions are additive.
II. A measurable amount of scaffold will degrade with time, but the overall continuity of the scaffold phase will remain intact.
III. The scaffold remains intimate with the ECM phase.
IV. The ECM phase can be modeled as an incompressible isotropic neo-Hookean material at the early implant timepoints since scaffold anisotropy likely dominates.
V. Scaffold-ECM interactions manifest as shearing and extensional effects between the scaffold embedded in the ECM.
VI. Scaffold-ECM interactions are additive and thus can be separated.
VII. Composites may undergo large deformations.

3.3.3 A strain energy based constitutive model for continuous scaffold-ECM composites

Since previous work on PGA:PLLA scaffold-ECM composites revealed a reinforcing effect of ECM on the scaffold not explained by the rule of mixtures, a modified form of the rule of mixtures is used with volume-fraction weighted strain energy contributions from the ECM (matrix, M), scaffold fiber (SF), and scaffold fiber-ECM interactions (FM) as

$$\Psi = \phi_{SF}\left(\Psi_{SF} + \Psi_{FM}\right) + \phi_{M}\Psi_{M} \qquad (3.21).$$

In this formulation, the matrix volume fraction is related to the fiber volume fraction as $\phi_M = \left(1 - \phi_{SF}\right)$. With this approach, reinforcing effects can be incorporated into the full model form. A simplified scaffold geometry is assumed based on a previous structural analysis [9] where scaffold was shown to exist as undulated (crimped) fibers with a preferred and cross-preferred direction. In the scaffold, these fibers were shown to have a uniform crimp and diameter. Additionally, fiber-fiber interactions were shown to occur at fiber cross-over points, reinforcing the overall scaffold. The accretion of matrix on the scaffold was shown to effectively decrease the fiber-fiber cross-over distance, resulting in a reinforcing effect in the scaffold.

In the current model, initial pilot equibiaxial stretch experiments using virgin PGA:PLLA scaffold showed a linear response between P-λ. Using equibiaxial stretch experiments creates a condition where fiber rotations are non-existent and only extensional stretch in the fibers occur; the total stress is the sum of both axes' stretch ($P_{fiber} = P_{11}+P_{22}$) with stretch defined by either axis ($\lambda_{11} = \lambda_{22}$). These results indicate that the effective response of the fibers in a given orientation is linear as shown in Figure 3.1. Further, using the crimp parameters determined from scanning electron microscope imaging from the work of Engelmayr, the stretch required to fully uncrimp fibers is estimated at 1.051, exceeding the stretch in the pilot equibiaxial stretch experiments and suggesting a purely uncrimping effect in the fibers. Therefore, in this current work, it is assumed that the scaffold fibers exhibit a linear relationship between first Piola-Kirchhoff stress and stretch and that they are only able to bear load during tensile loading (and not compression).

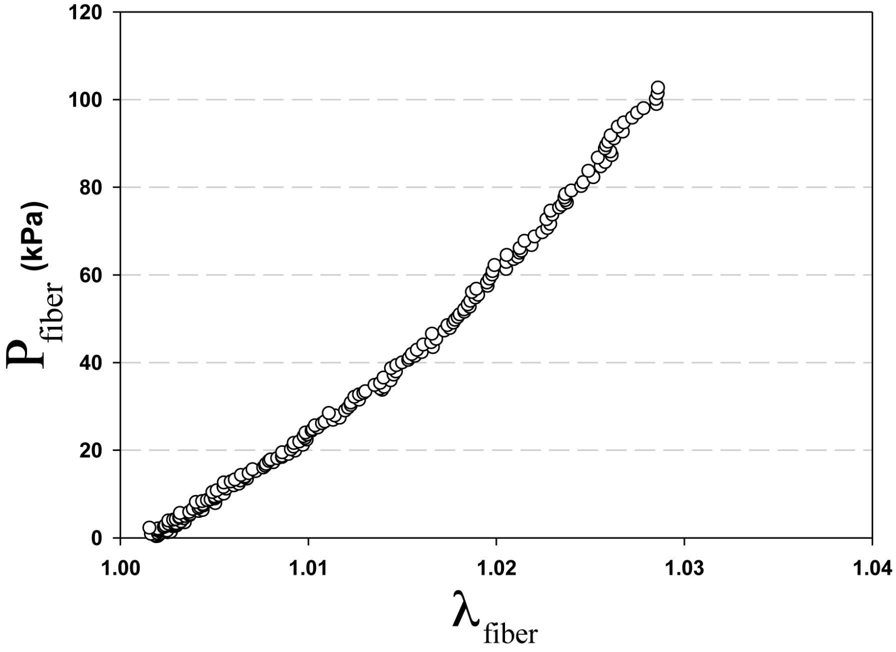

Figure 3.1. Equibiaxial stretch data for ensemble of scaffold fibers. Note the strong linearity.

An effective fiber modulus, K_{scaf} can be used to describe the stress response of both an individual collection of fibers and the fiber-fiber interactions for a given fiber orientation as.

$$P_{fiber} = K_{scaf}\left[\lambda_{fiber}(\theta) - 1\right], \tag{3.22}$$

where λ_{fiber} is the fiber ensemble stretch at a given angle θ defined as

$$\lambda_{fiber}(\theta) = \sqrt{\mathbf{N}(\theta)^{T}\mathbf{C}\mathbf{N}(\theta)}, \tag{3.23}$$

with $\mathbf{N}(\theta)$ as the fiber ensemble direction vector and **C** as the right Cauchy-Green strain tensor. Accretion of matrix on the scaffold is accounted for by making K_{scaf} a function of the matrix shear modulus μ as $K_{scaf} = f(\mu)$. Figure 3.2 shows a pictorial representation of the fiber and fiber-fiber interaction effects and how it manifests in the **P**-λ response.

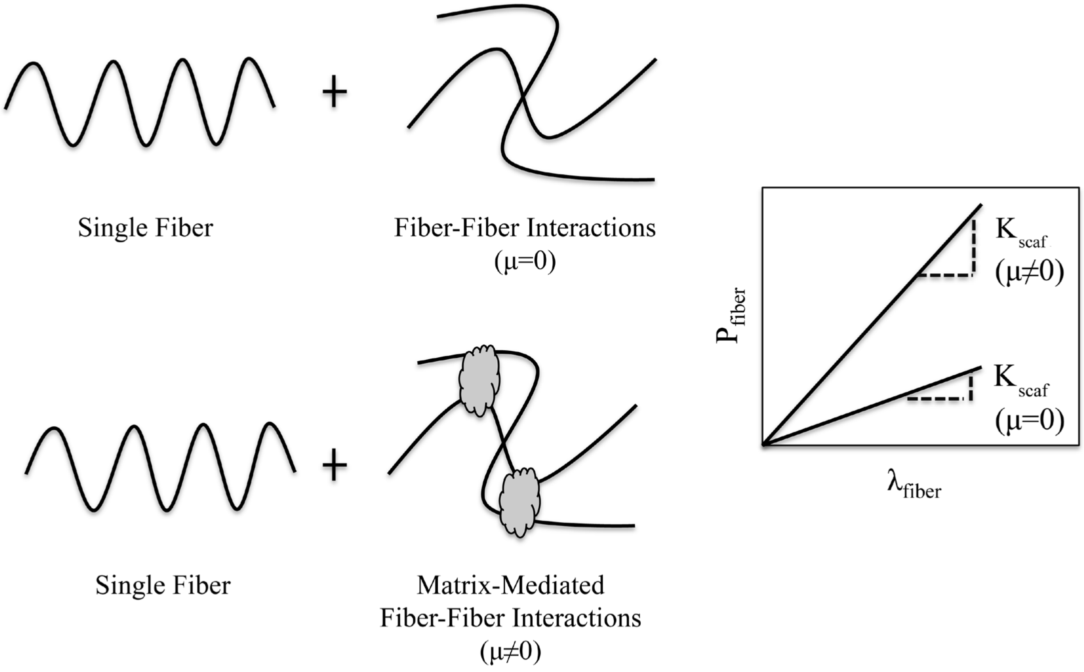

Figure 3.2. Representation of single fiber and fiber-fiber interactions with and without matrix accretion and how the stress response is influenced. Though single fiber effects may be non-linear, the combined single fiber and fiber-fiber interactions result in a linear response at the scaffold level.

Summing all scaffold fiber collections (described by a statistical distribution) over the full 180 degree orientation range yields the entire scaffold response as

$$\Psi_{SF} = \frac{K_{scaf}(\mu)}{2} \int_{-\pi/2}^{\pi/2} R\left(\theta, \mu_R, \sigma_R\right)\left[\lambda_{fiber}(\theta) - 1\right]^2 d\theta \tag{3.24}$$

or in terms of 1st Piola-Kirchhoff stress as

$$\mathbf{P}_{SF} = \int_{-\pi/2}^{\pi/2} R\left(\theta, \mu_R, \sigma_R\right)\left[\lambda_{fiber}(\theta) - 1\right] d\theta, \tag{3.25}$$

where $R\left(\boldsymbol{\theta}, \boldsymbol{\mu}_R, \boldsymbol{\sigma}_R\right)$ is defined as a scaled beta distribution

$$R(\theta, \mu_R, \sigma_R) = \frac{\beta\left(y, \gamma, \delta\right)}{\pi}. \tag{3.26}$$

The angle y and shape parameters $\boldsymbol{\gamma}$ and $\boldsymbol{\delta}$ are given as

$$y = \frac{\theta + \frac{\pi}{2} - \zeta}{\pi}, \quad \gamma = \frac{\mu_R^2 - \mu_R^3 - \sigma_R^2 \mu_R}{\sigma_R^2}, \text{ and } \delta = \gamma \frac{1 - \mu_R}{\mu_R} \tag{3.27}$$

where ζ is an offset to the angle, and μ_R and σ_R are the mean and standard deviation.

As previous work showed the dominating mechanical properties of the scaffold compared to forming tissue, the tissue phase is assumed to take a neo-Hookean model form as

$$\Psi_M = \frac{\mu}{2}\left(I_1 - 3\right) \tag{3.28}$$

which can be expressed in terms of **P** using eq. (3.14) as

$$\mathbf{P}_M = \mathbf{F}^{-1}\left(\mu \mathbf{B} - p\mathbf{I}\right), \tag{3.29}$$

where μ is the shear modulus (note the difference in subscript compared to the orientation distribution mean) and B is the left Cauchy-Green strain tensor. Under planar biaxial testing where $S_{13}=S_{23}=S_{33}=0$, p can be solved for directly as $p=B_{33}$. This simplified the characterization of the tissue mechanical properties to one parameter (shear modulus) while accommodating a generalized large deformation mode. Scaffold-ECM interactions were described in two manners; first, the effects of the ECM on the scaffold during extension of a scaffold fiber group of same orientation was considered by using the effective fiber modulus K_{scaf} as previously described. In this approach, the direct effects of increased ECM shear modulus on scaffold properties could be incorporated into the overall stress-stretch response of the scaffold phase. Second, a scaffold-ECM shearing term was added to the model to account for such interaction effects from scaffold fibers rotating (and thus creating shear) within the ECM matrix. With this interaction, it was assumed that fibers and the surrounding matrix were perfectly bonded. From a geometrical description, a differential area element $\mathrm{d}\Gamma_0$ can be described with an initial scaffold fiber orientation vector $\mathbf{a}_0$ as its normal $\mathbf{n}_0 = \mathbf{a}_0$ as shown in Figure 3.3. Following a deformation, Nanson's relation can be used to compute the normal **n** of the deformed differential area element $\mathrm{d}\Gamma$:

$$\mathbf{n}\mathrm{d}\Gamma = J\mathbf{n}_0\mathbf{F}^{-1}\mathrm{d}\Gamma_0 . \tag{3.30}$$

Rearranging and simplifying yields

$$\mathbf{n} = \frac{1}{\left|\mathbf{n}_0\mathbf{F}^{-1}\right|}\mathbf{n}_0\mathbf{F}^{-1} = \frac{1}{\left|\mathbf{a}_0\mathbf{F}^{-1}\right|}\mathbf{a}_0\mathbf{F}^{-1}, \tag{3.31}$$

where $\left| \quad \right|$ indicates the norm of the vector.

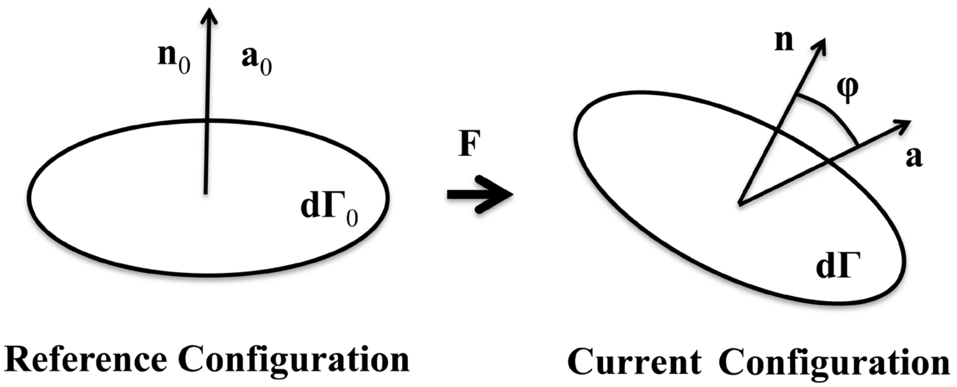

Figure 3.3. Geometric description of fiber-matrix shearing interaction.

The denominator of eq. (3.31) can be expressed as

$$\left|\mathbf{a}_0\mathbf{F}^{-1}\right| = \sqrt{\mathbf{a}_0\mathbf{F}^{-1}\mathbf{F}^{-\mathrm{T}}\mathbf{a}_0} = \sqrt{\mathbf{a}_0\mathbf{C}^{-1}\mathbf{a}_0}\,. \tag{3.32}$$

With knowledge of the deformation gradient tensor **F**, it is possible to compute the deformed fiber direction vector **a** as

$$\mathbf{a} = \frac{1}{\lambda_{\mathrm{fib}}}\mathbf{F}\mathbf{a}_0\,. \tag{3.33}$$

Thus, shearing between the fiber and matrix can be represented by φ (Figure 3.3) as

$$\cos(\varphi) = \mathbf{n}\cdot\mathbf{a} = \frac{1}{\left|\mathbf{a}_0\mathbf{F}^{-1}\right|}\frac{1}{\lambda_{\mathrm{fib}}}\mathbf{a}_0\mathbf{F}^{-1}\mathbf{F}\mathbf{a}_0 = \sqrt{\frac{1}{(\mathbf{a}_0\mathrm{C}^{-1}\mathbf{a}_0)}\frac{1}{\mathrm{I}_4}}\,. \tag{3.34}$$

Calling on the Cayley-Hamilton theory (a second order tensor **C** satisfies its own characteristic equation),

$$\mathrm{C}^3 - \mathrm{I}_1\mathrm{C}^2 + \mathrm{I}_2\mathrm{C} - \mathrm{I}_3\mathbf{I} = 0\,, \tag{3.35}$$

and multiplying by $\mathbf{C}^{-1}$ and simplifying to yield

$$\mathbf{C}^{-1}=\frac{1}{I_3}(\mathbf{C}^2-I_1\mathbf{C}+I_2\mathbf{I}),\tag{3.36}$$

allows for direction substitution into eq. (3.34) for $\mathbf{C}^{-1}$ as

$$\cos(\varphi)=\mathbf{n}\cdot\mathbf{a}=\sqrt{\frac{I_3}{(I_5-I_1I_4+I_2)I_4}}\,.\tag{3.37}$$

This can be further simplified to

$$\tan^2(\varphi)=\frac{1}{\cos^2(\varphi)}-1=\frac{I_4}{I_3}(I_5-I_1I_4+I_2)-1\ .\tag{3.38}$$

Finally, eq. (3.38) can be defined in terms of a new invariant $\chi=\tan^2(\varphi)$ so that the total scaffold fiber-matrix interaction strain energy can be expressed as

$$\Psi_{FM}=\frac{K_{FM}(\mu)}{2}\chi^2\tag{3.39}$$

where K_{FM} is a scaffold shearing modulus and is a function of the matrix shear modulus. In the combined form, the full strain energy function for the composite can be expressed as

$$\Psi=\phi_{SF}\left[\frac{K_{scaf}(\mu)}{2}\int_{-\pi/2}^{\pi/2}R\left(\theta,\mu_R,\sigma_R\right)\left[\lambda_{fiber}(\theta)-1\right]^2d\theta+\frac{K_{FM}(\mu)}{2}\chi^2\right]+\phi_M\left[\frac{\mu}{2}\left(I_1-3\right)-p\mathbf{I}\right]\tag{3.40}$$

or in terms of 1st Piola-Kirchhoff stress as

$$\mathbf{P}=\phi_{SF}\left[K_{scaf}(\mu)\int_{-\pi/2}^{\pi/2}R\left(\theta,\mu_R,\sigma_R\right)\left[\lambda_{fiber}(\theta)-1\right]d\theta+K_{FM}(\mu)\chi\right]+\phi_M\left[\mathbf{F}^{-1}\left(\mu\mathbf{B}-B_{33}\right)\right].\tag{3.41}$$

3.4 THEORETICAL FRAMEWORK FOR LONG IMPLANT TIMEPOINT CONSTITUTIVE MODEL

3.4.1 Previous discontinuous scaffold fiber constitutive modeling efforts

Though a good deal of experimental work exists in the literature surrounding engineered tissues (especially those based on nonwoven degradable polymeric scaffolds), very few works consider possible contributions from remaining scaffold phases and none attempt to account for such a phase [31, 33, 61-67] especially in long implant durations (LID). Often, investigators dismiss the potential role scaffold may play in the overall mechanical response of in vitro or in vivo scaffold-ECM composites cultured/implanted for more than three weeks, citing the fast degradation of constituents, most noticeably PGA. Evidence from section 2.3.2 suggests that though fragmented, the scaffold phase is still present in TEHV and TEC out to 140 days. A cursory investigation of published histology images from other research groups suggest similar observations can be made, transcending cell type, scaffold composition, or culturing conditions [61, 62].

A few issues arise, however, when one makes such assumptions without thoroughly investigating the validity of such claims. The body of literature surrounding polymeric scaffold degradation is quite large, with an equally large variation in results. For example, Gogolewski et al. [68] reported degradation of in vivo PGA sutures within four months, while Li and Mak [69] reported faster times of one month. Earlier work by Andriano et al. [70] suggested times as long as six to twelve months. Degradation has not been investigated in PLLA as much as in PGA, but most research notes longer degradation times [71]. It is thought that copolymer formulations of PGA and PLLA (as used in this study) help slow the degradation, by not only mixing a slower degrading constituent (PLLA) into the scaffold, but also because PLLA behaves more hydrophobic than PGA, limiting water absorption by roughly 2% [72, 73] and slowing hydrolysis (the driving force for degradation). Most noticeable, a clear distinction is not made in these studies between absence of physical continuity and absence of mechanical contribution. Though in an intuitive sense it is clear that fragmentation in suturing materials would have a substantial impact on the mechanical strength (simply because sutures rely on intact continuous scaffold fibers), such ideas cannot be translated to scaffolds with tissue ingrowth.

If one investigates the rich literature surrounding short fiber reinforced composites (SFRC), the effects of discontinuous fiber phases on the overall mechanical response of composites can be profound. Though the origins of SFRCs cannot be easily be traced to a particular point in time (such use has been observed throughout different cultures, especially in reinforcing pottery and bricks), the rigorous study of SFRCs became prominent in the latter half of the twentieth century, specifically with the advent of synthetic polymers and improved glass manufacturing techniques [74]. Cox in 1952 [75], first described a means to account for changes to the mechanical properties in composites when discontinuous fibers are used in place of continuous fibers. As the need for improved material performance at reduced manufacturing cost / increased ease of manufacturing rose during the 1970's and 1980's, much research was performed on investigating how length, geometry, orientation, and composition of short fibers influenced the overall mechanical properties [74, 76-78]. Such work gives insight into the potential role that degraded (short fiber) scaffolds can play in the overall mechanical response of engineered tissues. It is therefore prudent to reassess common assumptions made in evaluating these composites, work with specific quantitative information (as provided by such techniques in chapter 2), and arrive at new, more rigorously defined assumptions for modeling efforts guided by both theory and experiment. Finally, in keeping with focus in this body of work, it is important to utilize a mathematical model developed for soft tissues to evaluate the mechanical and structural quality of engineered tissues at increased implant durations.

3.4.2 Use of the rule of mixtures in discontinuous scaffold fiber constitutive models

Though previous work could not directly make use of the rule of mixtures in modeling of continuous scaffold-ECM composites without adding interaction terms, the rule of mixtures may be applicable to discontinuous scaffold phases at longer implant durations. Therefore, the theoretical framework described in this section looks to common means of estimating scaffold fiber-embedded composite properties using the rule of mixtures. A brief discussion on the assumptions of the rule of mixtures will be provided, as well as the ramifications for SFRCs. New considerations specific to SFRCs will follow and be applied to the TEC system of interest based on experimental mechanical data and structural information.

3.4.3 Assumptions when using rule of mixtures

As a traditional means to estimate mechanical properties of scaffold fiber-embedded composites, the rule of mixtures has a number of important assumptions that may lose applicability when dealing with short scaffold fiber composites. Specifically, the rule of mixtures as often applied asserts:

1. Scaffold fibers are present as a uniform distribution within the matrix.
2. Scaffold fibers are continuous with large aspect ratios.
3. Perfect bonding exists between the scaffold fibers and matrix.
4. The composite is without voids.
5. Scaffold fibers have a single known orientation with the matrix.

6. Loads are applied parallel or perpendicular to the scaffold fiber direction.
7. Scaffold fiber strain and matrix strain are equal (isostrain condition).
8. Scaffold fiber-fiber interactions are negligible.

From this non-exhaustive list, the overall driving assumption is that tensile strain along the axial direction in the composite is uniform resulting in the applied load being distributed between the matrix and scaffold fiber phases [76]. Though a range of other assumptions may exist, the stated list provides the most relevant and impacting of the assumptions as pertaining to extending the theory to SFRCs.

3.4.4 Important considerations in SFRCs

Within SFRCs, scaffold fibers are discontinuous and of significantly short lengths than in continuous scaffold fiber theory. This results in differences existing between the strain in the scaffold fiber and matrix near the scaffold fiber ends and, as a result, the isostrain condition no longer being valid. Shear forces, therefore, play a driving role in stressing scaffold fibers in tension; this transferring of stress allows the applied load to be dispersed amongst the short scaffold fibers [76]. Critical the transferring of load is the relationship between the scaffold fiber, matrix, and interface mechanical properties to the geometry of the scaffold fiber to ensure shear stresses can fully develop and transmit loads to the scaffold fibers. Cox proposed the concept of critical length L_c that specifically relates scaffold fiber diameter d and length L to relevant matrix/fiber properties as:

$$L_c = \frac{d\sigma_F^{UTS}}{2\tau} . \tag{3.42}$$

Here, σ_F^{UTS} denotes the tensile strength of the scaffold fiber and τ represents the lesser of the matrix shear strength or the scaffold fiber-matrix interface shear strength [81]. It can be seen that as the difference between the scaffold fiber and matrix properties diverge, the need exists for the scaffold fiber length to increase so that load can be transferred to it through shear stress. Either the matrix shear strength or the interface shear strength is the limiting factor in this process. Bowyer and Bader [82] then extended this idea to look at critical length as a function of composite strain ε_c (note that in the context of this work the strains are for small deformation theory and are not directly applicable to a large deformation framework. It will be shown, however, that this is irrelevant for these systems) as:

$$L_c = \frac{dE_F\varepsilon_F}{2\tau_{FM}}, \tag{3.43}$$

where E_F is the scaffold fiber linear elastic modulus and τ_{FM} is the scaffold fiber-matrix interface shear stress. Bowyer and Bader [82] then proceed to show that at scaffold fiber lengths less than the critical length for a given composite strain, the average stress carried by the scaffold fibers is simply a linear function of aspect ratio (L/d) and matrix shear stress as:

$$\tilde{\sigma} = \frac{L\tau_{FM}}{d}, \tag{3.44}$$

and not nearly as large as the maximum stress transfer amount.

It is possible then to use eq. (3.42) to estimate the smallest critical length in the TEC experimental work. From previous modeling efforts of PGA:PLLA scaffolds by Engelmayr and Sacks [9], mean scaffold fiber diameter and linear elastic modulus value (uniaxial experiments) are known as 18 μm and 18,480 MPa respectively. With uniaxial failure strength estimates of TECs from Hoerstrup et al. [31], τ_{FM} can be estimated as 3.5 MPa. From these values, a critical length of 2,300 μm can be estimated. Compared to measured length values from section 2.3.3, this is roughly 23 times larger than measured values of 100 μm. It should be noted that overestimating τ_{FM} would serve to decrease the critical length and that if actual matrix shear stress values were lower, critical length values would be larger. These estimates also assume that the matrix will fail prior to interface failure which is likely unrealistic. With these conservative estimates in mind, true values of the critical length are probably much larger, increasing disparity with actual scaffold fiber lengths (and thus further reducing reinforcing ability). Therefore, eq. (3.42) can be applied to describe how stress is being carried by the scaffold fiber phase in an ideal situation.

These considerations do not account for randomly oriented scaffold fibers or volume fraction of the scaffold phase. Though research in SFRC scaffold fiber alignment is quite broad [78, 81, 83-89], the work is limited to empirical relations to experimental data, as no direct calculation exists. Two models are prominent in the literature: the laminate model, based on multiple stacked laminates of single-oriented scaffold fibers, and the aggregate model, based on an average set of mechanical properties applied to zones with various alignments in the composite. Though slightly more sophisticated, the aggregate model has not been successfully applied to many systems and is limited in application to a few mechanical properties [90-92], while the laminate model has been used more extensively and with better success [93-95]. Lavengood and Goettler [96] in an oft-cited work experimentally verified an approximate penalty value χ_1 of 0.2 to the scaffold fiber modulus based on a random three-dimensional orientation. This was intended to account for scaffold fibers not aligned (or not fully aligned) with the load application direction.

If one considers these three factors – scaffold fiber lengths drastically less than the critical length, volume fraction considerations, and scaffold fiber orientations, the total stress carried by the short scaffold fiber phase can be estimated as:

$$\tilde{\sigma}_F = \chi_1 \phi_F \frac{L\tau_{FM}}{d} \quad . \tag{3.45}$$

Unfortunately, obtaining knowledge of the interface shear stress is an exceptionally challenging issue and one without many practical solutions in literature. Further compounding such information is the unique system of study – in vivo tissue on polymeric scaffolds. Therefore, experimental information is required to assess if any (if at all) reinforcing ability exists in these systems using a tissue simulacre as described in chapter 4. Additionally, if histological evidence can support initial indications that the scaffold fiber-matrix interface is poor and disconnected, then the ability of shear stresses to develop between the two phases in non-existent and the effects of the short scaffold fibers can be ignored.

3.4.5 A strain energy based constitutive model for LID scaffold-ECM composites

As previously described for soft tissues by Sacks [79] and modified by Wognum [80], for a pseudoelastic, hyperelastic material response, the total strain energy can be assumed to be a linear function of volume-fraction weighted strain energy contributions of the scaffold fiber and matrix phases:

$$\Psi = \phi_{SF}\Psi_{SF} + \phi_M \Psi_M , \tag{3.46}$$

where Ψ_{SF} is the fiber strain energy and Ψ_M is the matrix strain energy. This is similar to eq. 3.21 without the interaction term present. If the strain energy is formulated as a function of green's strain tensor **E**, then a relation between **E** and Ψ yields the 2nd Piola-Kirchhoff stress tensor **S** as shown in eq. 3.19. Similar to the continuous model, a planar 2D testing configuration is used which results in p$\mathbf{C}^{-1}$ being negated. The relationship between **S** and **E** can further be expanded to

$$\mathbf{S}(\mathbf{E}) = \phi_{SF}\mathbf{S}_{SF}(\mathbf{E}) + \phi_{M}\mathbf{S}_{M}(\mathbf{E}) \tag{3.47}$$

based on eq. (3.17) $\mathbf{S} = 2\frac{\partial \boldsymbol{\Psi}}{\partial \mathbf{C}} = \frac{\partial \boldsymbol{\Psi}}{\partial \mathbf{E}}$. From the previous section on SFRCs, it will be assumed that the short scaffold fibers do not contribute to the overall mechanical response thus eliminating the S_{SF} term. For collagenous soft tissues, the tissue (matrix) phase structural constitutive model can be formulated with the following assumptions:

1. The tissue can be idealized as a network of collagen fibers of various structures embedded within a compliant ground matrix.
2. The net tissue response is the sum of the individual fiber responses, so fiber-fiber interactions are ignored.
3. Fiber forces are much larger than hydrostatic forces generated by the ground matrix and are assumed to induce incompressibility at a tissue level.
4. The ground matrix includes contributions from non-load bearing constituents.
5. Collagen fibers are intrinsically crimped and straighten with increased stretch. The load required to straighten a collagen fiber is negligible to the load transmitted to the stretched fiber once straight. Fibers are linear elastic after straightened.

As collagen is considered the major load-bearing structure arranged in ensembles, thus allowing $\mathbf{S}_M(\mathbf{E})$ to be expressed as:

$$\mathbf{S}_M(\mathbf{E}) = \int_{-\pi/2}^{\pi/2} R\left(\theta, \mu_R, \sigma_R\right) S_{col}^{ens}\left[E^{ens}(\theta)\right] \mathbf{N} \otimes \mathbf{N} d\theta \tag{3.48),}$$

where $S^{ens}\left[E^{ens}(\theta)\right]$ is the effective stress-strain response of a collagen ensemble (ens) , E^{ens} is the uniaxial ensemble green's strain tensor of a collagen ensemble, and $R\left(\theta, \mu_R, \sigma_R\right)$ is the orientation distribution of all load-bearing collagen ensembles in the tissue. Thus, the total matrix response is a sum of all collagen ensemble contributions across a full 180 degree orientation. Here, the ensemble strain E^{ens} is computed as:

$$E^{ens}(\theta) = \mathbf{N}(\theta)^T \mathbf{E} \mathbf{N}(\theta), \tag{3.49}$$

where $\mathbf{N}(\theta)$ is a unit vector in the direction of a single collagen ensemble in the reference configuration as in eq. (3.23). As a structural term, the collagen ensemble orientation distribution can be described as a modified beta distribution as described by eq. (3.26) defined over the interval $\theta \in \left[-\pi/2, \pi/2\right]$ and scaled to $y \in \left[0,1\right]$. As in eq. (3.27) and eq. (3.28), two shape parameters are defined based on the mean μ_R and standard deviation σ_R values. Note that this is a similar form as used in the continuous model form to describe the scaffold fiber orientation, except that the function scaling is different between the two.

Modeling of the collagen stress-strain response is based on the experimentally verified and measured appearance of crimp in collagen fibers. Once straightened, the fibers follow a linear relationship between **P** and λ (stretch) of the fiber, as shown from X-ray diffraction experiments. As such, this relation can be described as

$$P_{col\_fib} = \eta\left(\lambda - \lambda_s\right), \tag{3.50}$$

where the fiber stretch λ is defined as $\lambda = {}^{\partial l}\!/\!{}_{\partial l_0}$, λ_s is the stretch required to remove crimp, and η is the collagen fiber modulus. This can be reformulated in terms of **S** and **E** using $\lambda = \sqrt{1+2E}$ resulting in

$$S_{col\_fib} = \eta\left(1-\frac{\sqrt{1+2E_s}}{\sqrt{1+2E}}\right), \tag{3.51}$$

where E_s is the strain required to remove crimp. If multiple ensembles of fibers are present with various levels of crimp, a non-linear response can be observed as an increasing number of ensembles are activated (or begin to transmit load) as the tissue is stretched.

Figure 3.4 shows the effects of linear single fibers with various amounts of crimp creating ensemble level and tissue level non-linear stress responses.

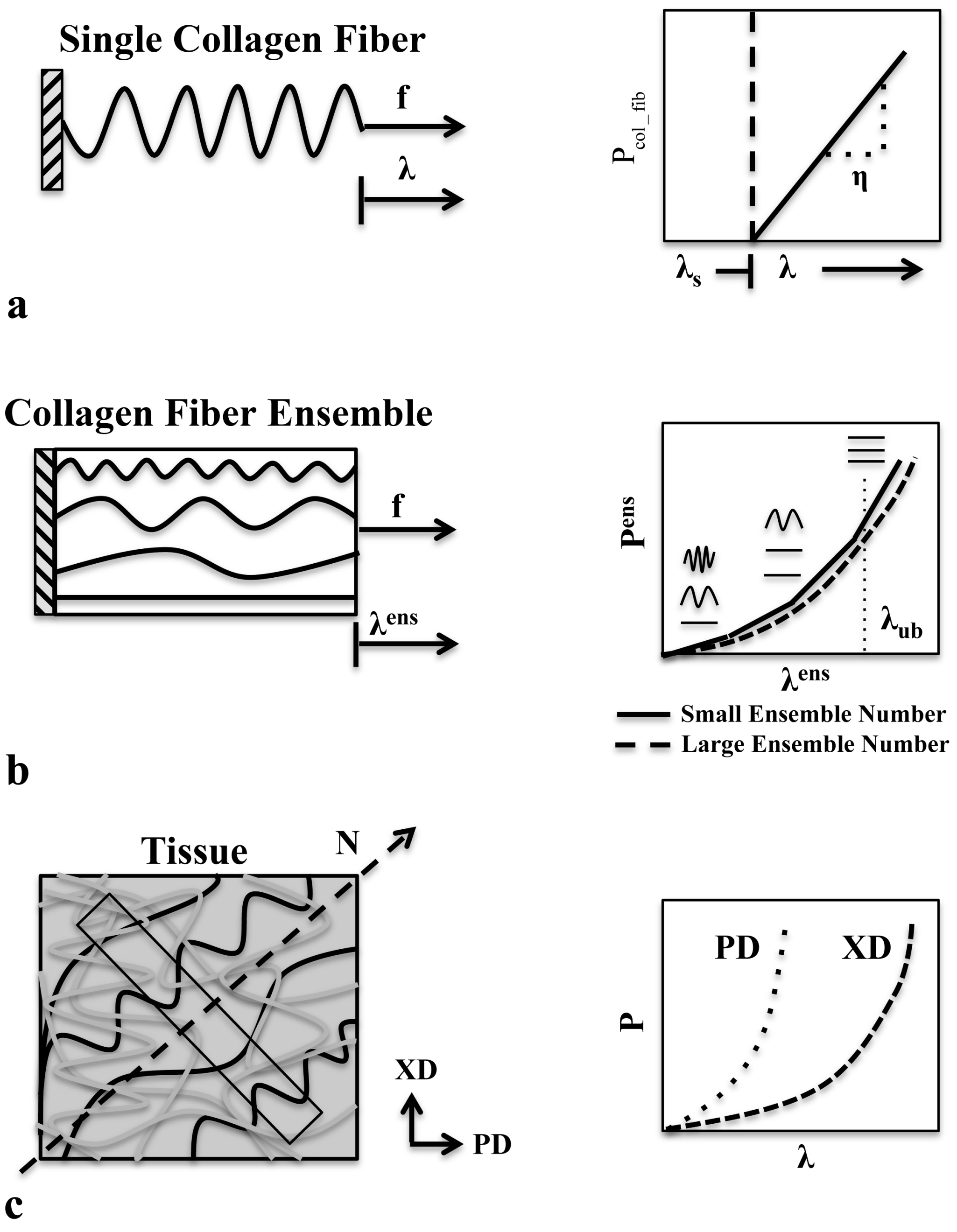

Figure 3.4. Collagen fiber recruitment in the discontinuous scaffold constitutive model. (a) Stress response of a single fiber is linear in P-λ, but when fibers of various crimp amounts exist (b), a non-linear stress response is observed. The tissue level response (c) shows anisotropy due to a collagen fiber orientation distribution as well as non-linearity due to fiber recruitment.

A stochastic approach can be taken where a recruitment distribution $D(x)$ is used to describe the fraction of fibers realizing a fully straightened state at a given stretch, defined over lower stretch bounds (stretch where recruitment begins) and upper stretch bounds (stretch where all fibers are uncrimped). With this, the combined ensemble **S-E** relationship can be expressed as

$$S_{col}^{ens} = \phi_{col} \int_0^{E^{ens}} D(x) S_{col\_fib}(x)\,dx = \eta\phi_{col} \int_0^{E^{ens}} D(x) \left[1 - \frac{\sqrt{1+2x}}{\sqrt{1+2E^{ens}}} \right] dx, \tag{3.52}$$

where $D(x)$ is defined as a beta distribution function $\beta(y)$ mapped to the interval $[E_{lb}, E_{ub}]$ and with a mean μ and standard deviation σ as

$$D(E,\mu,\sigma) = \begin{cases} \dfrac{\beta(y, s_1, s_2)}{E_{ub} - E_{lb}} & E_{lb} \le E \le E_{ub} \\ 0 & \text{otherwise} \end{cases} \tag{3.53}$$

with s_1 and s_2 as

$$s_1 = \frac{\mu^2 - \mu^3 - \mu\sigma^2}{\sigma^2} \text{ and } s_2 = \frac{\mu^2}{\sigma^2} s_1. \tag{3.54}$$

Note that $K_{eff} = \eta\phi_{col}$ since η represents the stiffness of a single fiber and K_{eff} represents the effective stiffness of all fibers in an ensemble. Summing over all possible fiber orientations yields the form

$$\mathbf{S}_M(\mathbf{E}) = \int_{-\pi/2}^{\pi/2} R(\theta, \mu_R, \sigma_R) \left\{ K_{eff} \int_0^{E^{ens}} D(x) \left[1 - \frac{\sqrt{1+2x}}{\sqrt{1+2E^{ens}}} \right] dx \right\} \mathbf{N} \otimes \mathbf{N}\, d\theta. \tag{3.55}$$

This formulation of the entire composite constitutive relationship allows for the development of a function to describe the short scaffold fiber response of the fragmented scaffold. To move towards this, it is first necessary to understand how such scaffold fibers respond to load application in a composite.

3.4.6 Full form of the LID scaffold fiber constitutive model

Based on the assumptions of negligible strain energy contributions of the LID scaffold fiber phase determined in the previous sections, it is possible to formulate the final form of the constitutive model for discontinuous scaffold-ECM composites. Using eq. (3.46) and assuming $\mathbf{S}_F(\mathbf{E})=0$, the component form of the constitutive relation can be written as:

$$S_{11}=\phi_M K_{eff}\int_{-\pi/2}^{\pi/2} R(\theta,\mu_R,\sigma_R)\left\{\int_0^{E^{ens}} D(x)\left[1-\frac{\sqrt{1+2x}}{\sqrt{1+2E^{ens}}}\right]dx\right\}\cos^2(\theta)\,d\theta, \tag{3.56}$$

$$S_{12}=\phi_M K_{eff}\int_{-\pi/2}^{\pi/2} R(\theta,\mu_R,\sigma_R)\left\{\int_0^{E^{ens}} D(x)\left[1-\frac{\sqrt{1+2x}}{\sqrt{1+2E^{ens}}}\right]dx\right\}\cos(\theta)\sin(\theta)\,d\theta, \tag{3.57}$$

$$S_{22}=\phi_M K_{eff}\int_{-\pi/2}^{\pi/2} R(\theta,\mu_R,\sigma_R)\left\{\int_0^{E^{ens}} D(x)\left[1-\frac{\sqrt{1+2x}}{\sqrt{1+2E^{ens}}}\right]dx\right\}\sin^2(\theta)\,d\theta. \tag{3.58}$$

It should be noted that although the scaffold fiber phase does not mechanically contribute to the strain energy, it does have volume, which reduces the overall volume fraction of the matrix phase. Therefore, though not actively contributing, the fiber phase does passively contribute and hence should be considered if only to reduce the matrix volume fraction.

3.5 CONCLUSION

In this chapter, the theoretical framework is developed for generalized non-linear finite deformation constitutive relations in two different scaffold-ECM composites. In this first of such models, a continuous scaffold phase is assumed based on a linear scaffold fiber $\mathbf{P}-\lambda$ relation. With scaffold fibers exhibiting a quantifiable orientation distribution, a summation of all fiber response across a full 180 degree angle range provides the complete scaffold response. Previous modeling efforts illustrate the needed to account for substantial reinforcing effects resulting from the scaffold phase. A mathematical model is presented which contains strain energy contributions from the tissue (matrix), scaffold fiber, and scaffold-tissue interaction. Scaffold interactions are further separated as originating either from extensional or shear effects. Since the scaffold phase likely dominates the mechanical response as these early tissue timepoints, a neo-hookean tissue relationship is assumed.

In the second model, a mathematical relationship is presented for long implant durations (discontinuous scaffold fibers) scaffold-tissue composites. A review of short fiber composite literature is provided, and it is shown from estimated material properties that the discontinuous scaffold fiber phase likely does not actively contribute to the strain energy. Therefore, it is assumed that all effects are due to the tissue phase. A strain energy relation is presented for the tissue phase based on a stochastic distribution of collagen fibers with varied degrees of crimp and orientation. Though linear in $\mathbf{P}-\lambda$, the combined effects of crimp and fiber orientation permit nonlinearity and anisotropy in the model. Finally, a reduction in tissue volume fraction is assumed based on the presence of the scaffold phase, though the scaffold phase does not contribute directly to the overall mechanical response.

4.0 MODEL PARAMETER ESTIMATION AND VALIDATION

4.1 INTRODUCTION

Important to any constitutive model, validation and parameter estimation provide the means to assess the applicability of a particular formulation and ultimately use it, with a certain degree of confidence, to a system of interest. These necessary steps are often difficult when modeling soft tissues, as the selection of tissue analogs is limited. In this chapter, a tissue analog system with tunable material properties is discussed, and a means to incorporate continuous and discontinuous scaffold phases is presented. Both scaffold phases are used to create scaffold-tissue analog composites over a range of matrix mechanical properties. Mechanical testing is performed, and the relevant parameters from the models developed in chapter 3 (specifically the scaffold-tissue interaction terms) are determined. Finally, the predictive capabilities of the models are assessed.

4.2 METHODS

4.2.1 Development of a tunable tissue analog

In order to investigate the coupled and decoupled effects of individual phases in the scaffold-tissue composites, it was necessary to employ a tissue analog with tunable mechanical properties within the range of native tissue. This approach permitted quantifying the interaction (coupling) between both phases by first gaining insight into the contributions from decoupled constituents. As such, we utilized polyacrylamide gel (PAM gel) as described in previous work in our lab [23]. With this system, we were able to vary the concentration of acrylamide/bis prior to polymerization to change the modulus. Previous studies showed the system capable of producing phantoms with elastic moduli within the range of 30 to 800 kPa. To make 10 ml of PAM gel, a 30% solution of 37:5 acrylamide/bis (Bio-Rad Laboratories, Hercules, CA) and deionized water of appropriate quantities (Table 4.1) were mixed with 2500 µL of 1.5M Tris/HCl buffer (Bio-Rad) and 100 µL of 10% sodium dodecyl sulfate (SDS) (Bio-Rad) as per the manufacturer's instructions. Fresh 10% ammonium persulfate (APS) (SIGMA, Sigma-Aldrich Co., St. Louis, MO) was mixed, and 50 µL was added to the solution along with 5 µL of tetramethyleethylenediamine (TEMED) (Bio-Rad). The solution was gently mixed and cast between a 1 mm glass spacer plate and a cover plate in a Bio-Rad SDS-PAGE gel assembly system. In these ECM phantoms, 1 ml of 1-butanol (SIGMA) was mixed with 4.5 ml of deionized water, and approximately 100-200 µL was carefully pipetted on top of the cast PAM gel liquid to provide an anaerobic seal. After forty minutes, the plates were removed from the gel assembly system and separated. Specimens were cut from the gel sheet and stored in cold deionized water until tested.

Table 4.1. Volume measurements for acrylamide/bis and deionized water to obtain specific PAM gel monomer concentrations. All values are for 10ml total volume. The symbol 'X' denotes if uniaxial or biaxial testing was performed.

Monomer Concentration	DI H20 (µl)	Acryl/Bis (µl)	Uniaxial Testing	Biaxial Testing
5.00%	5680	1670	X	X
7.50%	4850	2500	X	X
10.00%	4015	3335	X	X
11.25%	3590	3760	X	X
12.50%	3180	4170	X	X
17.50%	1520	5830	X	X
19.10%	985	6365	X	---
20.70%	450	6900	X	X
22.00%	0	7350	X	---

4.2.2 Determination of PAM gel mechanical properties

To evaluate the effect of the matrix phase on the PGA:PLLA scaffold, the mechanical properties of the matrix alone (PAM gel) were first studied. Because biaxial mechanical testing could not easily be performed due to specimen attachment difficulties, both uniaxial extension and pure shear experiments were performed to determine the shear modulus of the PAM gel for varied monomer concentrations. For each PAM gel concentration of interest, a total of ten specimens (five each for uniaxial extension and pure shear) were cut from approximately 15 x 15 cm sheets. To perform uniaxial extension experiments, specimens 4.5 mm wide and 10 mm long were cut, while specimens 20 mm wide and 2 mm long were cut for pure shear experiments. Thickness measurements were taken at six points on each specimen and averaged. Using the MTS Triton 2500 testing device (MTS Systems Corporation, Eden Prairie, MN), specimens were loaded between sandpaper-coated grips on the device. A small preload of 0.05 N was applied to the specimens to provide a uniform starting point for all specimens. The gage length (distance between grips) was recorded. Testing was performed to a strain of 30% based on gage length.

Using a custom-written Mathcad program (Parametric Technology Corporation), paired data sets (uniaxial extension and pure shear) taken from adjacent locations from the PAM gel sheet were fit together to compute shear modulus using a Neo-Hookean model (note this is formulated in terms of stress and stretch in one direction):

$$P_{11}^{\mathrm{uniax}} = \mu\left(\lambda_1 - \frac{1}{\lambda_1^2}\right) \qquad (4.1),$$

$$P_{11}^{\mathrm{shear}} = \mu\left(\lambda_1 - \frac{1}{\lambda_1^3}\right) \qquad (4.2),$$

where eq. (4.1) is for uniaxial extension, eq. (4.2) is for pure shear, μ is the shear modulus, λ_1 is the stretch, and P_{11} is the first Piola-Kirchhoff stress (note this is formulated in terms of stress and stretch in one direction). In all cases, fitting produced an $R^2 > .90$. With this, a response curve of measured shear modulus as a function of increasing PAM gel monomer concentration could be determined.

4.2.3 Application of tunable system for constitutive structural models in scaffold fiber composites

Crucial to the validation and parameter estimation of the constitutive models described in chapter 3, it was necessary to embed both intact (continuous) and fragmented (discontinuous) PGA:PLLA scaffold in PAM gel. Preliminary feasibility studies and previously published work [23] verified that the continuous scaffold could absorb the PAM gel and form a cohesive matrix. Manually fragmented scaffold was also mixed with and embedded with the PAM gel without any difficulty.

To fabricate the continuous scaffold-ECM composites, squares of PGA:PLLA co-polymer scaffold (Concordia Medical, Warwick, RI) were cut to 15x15 mm. These scaffold segments were coated with liquid PAM gel to fully absorb into the scaffold. PAM gel-infused scaffold was then slid between the glass plates and surrounded by additional liquid PAM gel. As in the ECM phantoms, approximately 100-200 µL of saturated 1-butanol was carefully pipetted on top of the cast PAM gel liquid to provide an anaerobic seal. After forty minutes, the plates were removed from the gel assembly system and separated. Specimens were cut from the gel sheet and stored in cold deionized water until tested.

For the discontinuous scaffold-ECM composites, fragmentation of scaffold was performed using a Thomas Wiley Mini-Mill (Thomas Scientific, Swedesboro, NJ, USA) with a screen of 60 mesh in place to filter fragments under 251 µm. This size was chosen both to be within the range of the fragmented sizes determined in section 2.3.3 and also due to limitations of the milling machine. For a given PAM gel volume of 10 ml, 0.126 grams of fragmented scaffold were added prior to casting to produce a scaffold volume fraction of 7%. This was selected as it represented the upper limit to scaffold volume fraction observed in the intact scaffold specimens. Approximately 100-200 µL of saturated 1-butanol was carefully pipetted on top of the cast PAM gel liquid to provide an anaerobic seal. After forty minutes of setting, the scaffold-PAM gel sheets were gently removed from between the glass slides and cut into either 4.5 mm wide by 10 mm long strips (uniaxial extension experiments) or 20 mm wide by 2 mm long strips (pure shear experiments). Specimens were kept in deionized water and tested within two hours of setting.

4.2.4 Biaxial tensile testing of continuous scaffold system

Biaxial tensile mechanical testing was performed on segments of continuous scaffold-embedded PAM gel (Table 4.1); as in the pure PAM gel property study, it was not possible to test discontinuous scaffold-PAM gel composites using biaxial testing due to poor hook retention. Tested PAM gel concentrations were the same as those used in the extension/pure shear uniaxial experiments, as in Table 4.1. Additionally, virgin scaffold was tested. A total of five specimens per PAM gel modulus group (including the virgin scaffold group) were evaluated. Following previously published methods for biaxial mechanical testing [30], specimens were cut to 15 mm per side, and thickness measurements were taken using a micrometer at six locations and averaged. Stainless steel 0.016 inch diameter hooks tied to both ends of 10cm long silk suture line were attached to specimens with four hooks per side forming two loops of suture. A total of sixteen hooks were placed creating four pairs of sutures. Four small cut portions of polyproline suture were attached to the middle region of the specimen in a square pattern using cyanoacrylate glue to serve as fiducial markers for strain tracking. The specimen was then placed in the biaxial testing device chamber filled with deionized water, and the silk suture loops were attached to stainless steel dowels on actuator arms. The preferred direction of the scaffold was aligned with the device X_1 axis.

Using custom-written control software, load control biaxial mechanical testing was performed. Free-floating (no-load) reference states were taken before preconditioning, after preconditioning, and after full protocol testing. A 0.2 gram tare load was applied to the specimen to enable proper device operation. Tare reference states before preconditioning, after preconditioning, and after full protocol testing were also taken. Preconditioning was performed for ten cycles with a fifteen second half cycle time. In all specimens it was found that ten cycles of preconditioning was adequate to ensure consistent loading results from subsequent tests. A seven protocol testing regime was used with peak X_1:X_2 stress ratios of 15:50, 25:50, 37.5:50, 50:50, 50:37.5, 50:25, and 50:15 kPa. Tests were performed for ten cycles with a fifteen second half cycle time. For scaffold-embedded PAM gel specimens, additional equistretch testing protocols were employed to permit the determination of extensional scaffold-ECM interaction effects. Following testing, specimens were discarded.

4.2.5 Biaxial tensile testing analysis

A finite-element based surface interpolation technique using a four-node linear Lagrangian element was employed to determine the two-dimensional in-surface Eulerian strain tensor at each time point [30]. In order to reference the deformed state configuration and calculate the strain tensor, a convective, in-surface coordinate system was used in which the axes were aligned to the local longitudinal and circumferential directions of the conduit. In this analysis, the Eulerian strain tensor components were computed at each load iteration. Additionally, the first and second Piola-Kirchhoff stresses were computed using the deformation gradient tensor. In all analyses, the post-preconditioned free-floating condition was used as the reference state.

4.2.6 Uniaxial testing of discontinuous scaffold system

For PAM gel specimens embedded with fragmented scaffold, uniaxial testing was performed to 30% strain. As previously described for pure PAM gel specimens, pure shear experiments were performed as well, and both sets of data from specimens cut from adjacent regions of the gel sheet were fit simultaneously to neo-hookean model relationships between stretch λ_1 and first Piola-Kirchhoff stress P_{11}. Five samples per group (two groups per each of six matrix shear modulus values) were tested, and the resultant shear moduli for PAM gel and PAM gel with fragmented scaffold were compared.

4.2.7 Continuous scaffold fiber constitutive model parameter estimation and validation

As shown in eq. (3.21) from section 3.3.3, the current continuous scaffold fiber constitutive model separates the composite response into scaffold, matrix, and interaction terms. To determine the effective scaffold fiber stiffness, a single equistretch data set was used to compute fiber ensemble first Piola-Kirchhoff stress and stretch in the virgin scaffold. Used by Lanir [97] and later Sacks [79], this technique provides total ensemble stress as the summation of stress from both axes; stretch is the same in both directions by nature of the test. A linear fit to the stress-stretch data was performed using a least-squares regression technique built into Mathcad to provide the effective scaffold fiber stiffness.

For scaffold-ECM interaction, this same procedure was performed on single equistretch data sets from scaffold-embedded PAM gel at various PAM gel shear modulus values. A linear fit to the first Piola-Kirchhoff stress-stretch data using a least-squares regression technique provided the effective fiber stiffness as a function of matrix shear modulus, quantifying the scaffold-matrix interactions due to extension.

To validate the model, biaxial mechanical data described in section 4.2.4 was used. Due to large permanent set effects observed in the most extreme testing protocols (15:50, 25:50, 50:25, and 50:15 kPa), only the middle three protocols were used. A total of five data sets per PAM gel modulus group were fit; four data sets from the virgin scaffold were used. A custom-written Mathcad program was used to fit the biaxial data to the model using a squared error minimization approach using the Levenberg-Marquardt algorithm. As the scaffold-matrix interaction term was expressed as a function of matrix shear modulus, the matrix shear modulus and scaffold orientation parameter (φ_{scaf}) were estimated in the fitting procedure. The standard deviation of the scaffold orientation was set to 31 degrees as reported in previous work [9]. Parameters for each specimen fit were outputted along with quality of fit assessments (r^2) for both directions. Since the shear modulus of the matrix (PAM gel) was independently determined from the uniaxial extension/pure shear experiments, this procedure served as a means to evaluate the validity of the model by comparing the estimated shear modulus (model) from the known shear modulus.

4.2.8 Long implant duration constitutive model validation

To validate the assumption that the discontinuous scaffold could not play a role in the mechanical response of the composites, the uniaxial extension/pure shear experiments on fragmented scaffold-embedded PAM gel were used to compute the overall composite shear modulus as in section 4.2.2. Fragmented scaffold-PAM gel composites for both uniaxial extension and pure shear experiments at each PAM gel shear modulus value (six to ten specimens per group) were used. The pure PAM gel shear modulus and fragmented scaffold-PAM gel shear modulus values for each shear modulus group was compared.

4.2.9 Statistical analysis

All results are presented as mean +/- standard error of the mean. For statistical analyses performed in this work, one-way ANOVA was utilized with the built in functionality of SigmaPlot 11 (Systat Software Inc., San Jose, CA), except for the fragmented-embedded/non-embedded PAM gel experiments where student t-tests were performed. An alpha value of 0.05

was used so that statistical significance was assumed if $p < 0.05$. Post-hoc testing was performed using the Student-Newman-Keuls method.

4.3 RESULTS

4.3.1 PAM gel mechanical properties

Figure 4.1 shows a representative PAM gel sheet. A fragmented scaffold fiber-embedded PAM gel sheet is shown alongside for comparison. Sheets maintained shape and were robust enough to handle for testing. Using the computed shear modulus from the combined pure shear and uniaxial extension experiments, Figure 4.2 shows how the mechanical properties of PAM gel changes with increasing monomer concentration. At each monomer concentration data point, shear modulus values are presented as mean +/- standard error of the mean. For this particular system, 22% represents the maximum achievable monomer concentration using the gel casting procedure previously detailed which resulted in a maximum gel shear modulus of 56.14 kPa +/- 0.608 kPa. A quadratic function was fit to the mean shear modulus values (SigmaPlot) to yield the following relationship between PAM gel monomer concentration (x, as monomer volume/total volume) and shear modulus μ:

$$\mu_{PAM} = a_1 x^2 + a_2 x \qquad (4.5).$$

Note that the function intercept was fixed at zero, so at zero monomer concentration, the shear modulus would be zero. Relation constants are shown in Table 4.2. The quality of fit was good, with an r^2 of 0.9904.

Table 4.2. PAM gel shear modulus , scaffold effective fiber modulus, and shear interaction correction relationship constants and quality of fits.

Relation	Model Constants		r^2
PAM Gel Shear modulus	a_1	995.91	0.9904
	a_2	54.985	
Scaffold Effective Modulus	b_1	96.100	0.9941
	b_2	1953.0	
	b_3	52070	
Matrix-Scaffold Shear Correction	c_1	0.0008	0.9584
	c_2	-0.0744	
	c_3	2.7412	

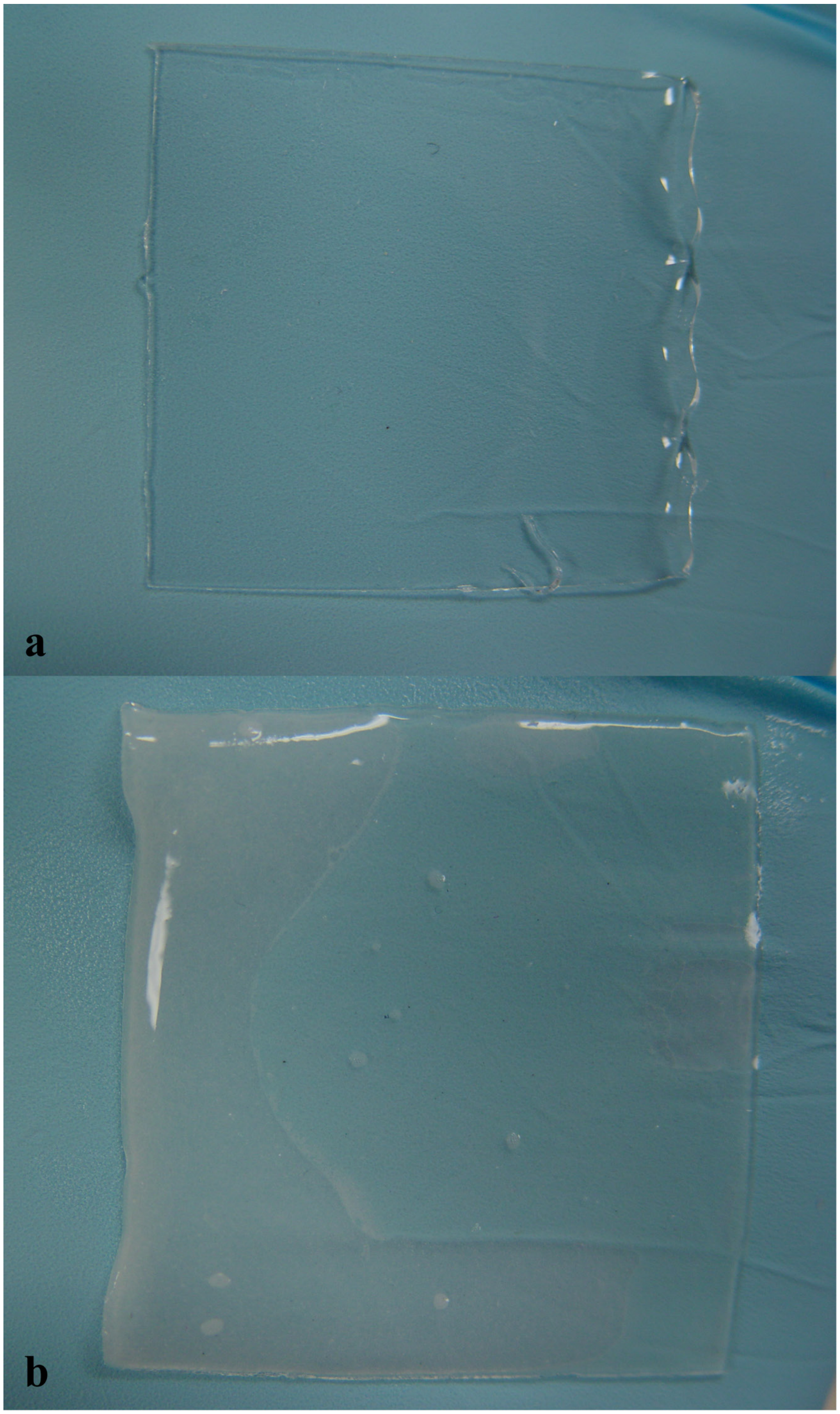

Figure 4.1. PAM gel sheets. Plain PAM gel (a) and fragmented scaffold-embedded PAM gel show differences in translucency.

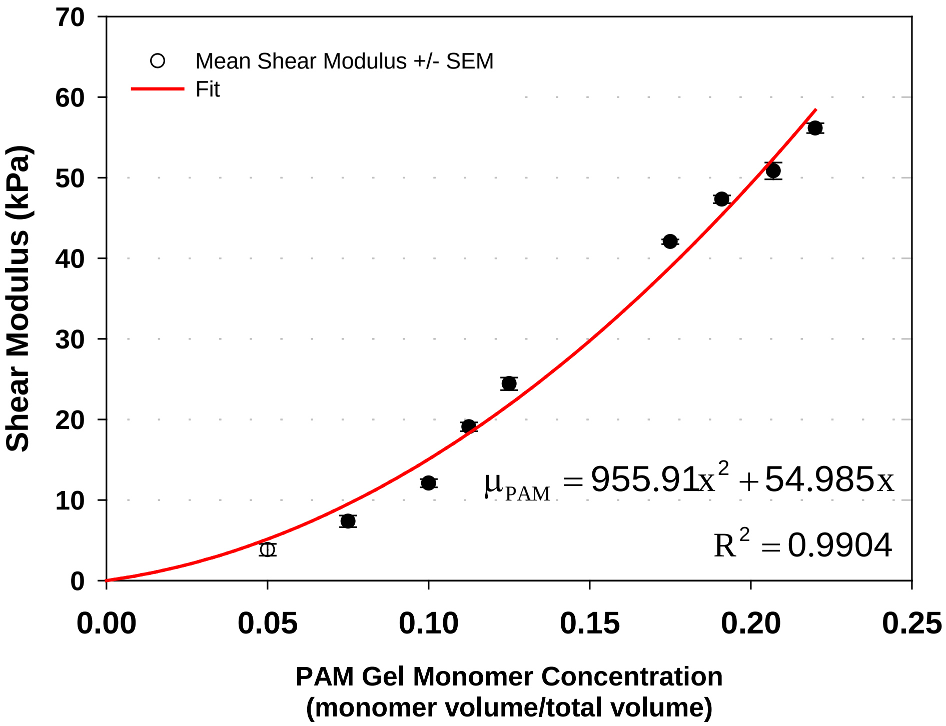

Figure 4.2. PAM gel monomer concentration vs. shear modulus as determined from uniaxial extension and pure shear. Red line is a quadratic fit to the data with equation and R^2 shown.

4.3.2 Continuous scaffold fiber constitutive model parameter estimation

In Figure 4.3, the mean biaxial stretches at peak equibiaxial stress (50 kPa) are shown for increasing PAM gel shear modulus. Values for virgin scaffold are included in the figure denoted as zero PAM gel shear modulus. The cross-preferred direction of the composites shown a marked decreased in mean stretch between 3.8 kPa gel-scaffold and 24 kPa gel-scaffold composites further differences much less with increasing PAM gel shear moduli above 24 kPa. The preferred direction shows little change in mean stretch with increased PAM gel shear modulus.

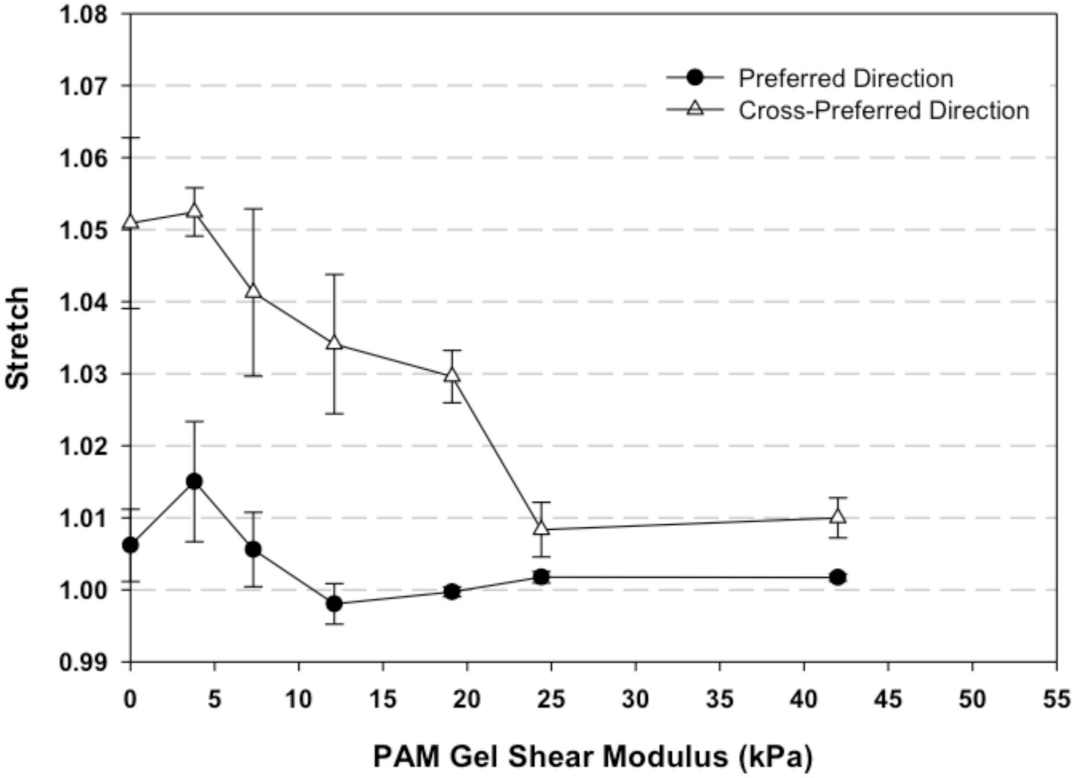

Figure 4.3. Equibiaxial stress of PGA:PLLA embedded PAM gel for increasing PAM gel shear modulus.

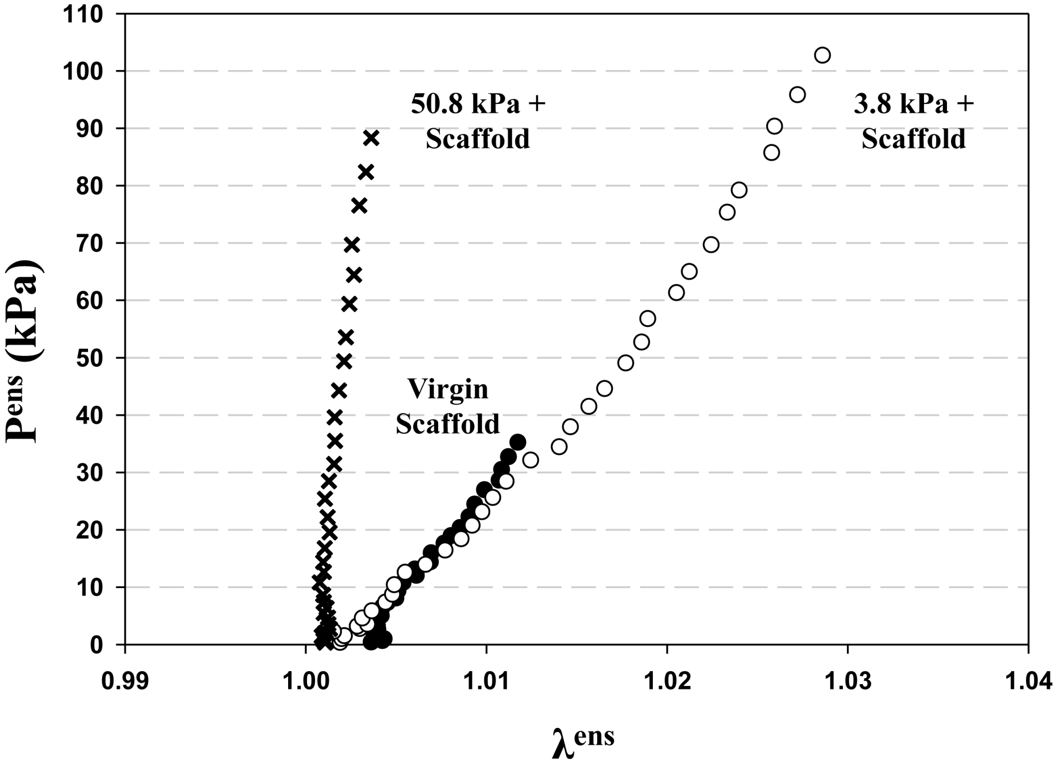

Figure 4.4. Equibiaxial stretch data for PGA:PLLA embedded PAM gel for PAM gel shear modulus minimum and maximum values. Data is plotted as $\mathbf{P}^{ens}$ vs. $\boldsymbol{\lambda}^{ens}$.

Figure 4.4 displays ensemble first Piola-Kirchhoff stress versus ensemble stretch for scaffold-embedded PAM gel composites at both extremes of gel modulus (smallest and largest values obtainable). Virgin scaffold is included as the lower limit of the PAM gel modulus (zero shear modulus). The results of the linear fits to stress-strain data are shown in Figure 4.5 illustrating how the scaffold effective stiffness changes with increasing PAM gel modulus. In all linear fits from these groups, r^2 values were above 0.95. Again, zero shear modulus represents the lower limit from the virgin scaffold material. At all shear gel modulus data points, the reported effective scaffold fiber stiffness was corrected for volume fraction based on the previously reported value of 0.0702. This scaled all values to a scaffold volume fraction of 1.0

so that the full model form could make use of the actual measured scaffold fiber volume fraction at a particular implant timepoint. A quadratic polynomial was fit to the experimental data to yield a relationship between matrix shear gel modulus (kPa) and resultant effective scaffold fiber modulus (kPa) of the composite as:

$$K_{eff} = b_1\mu^2 + b_2\mu + b_3 \tag{4.6}$$

Table 4.2 shows the relation constants. This fit had an r^2 value of 0.9941, indicating good agreement between the experimental data and fit. The results of Figure 4.5 also provide the homogenized scaffold fiber modulus as 52,070 kPa. This is represented as the y-intercept to the effective modulus-shear modulus relationship in eq. (4.6).

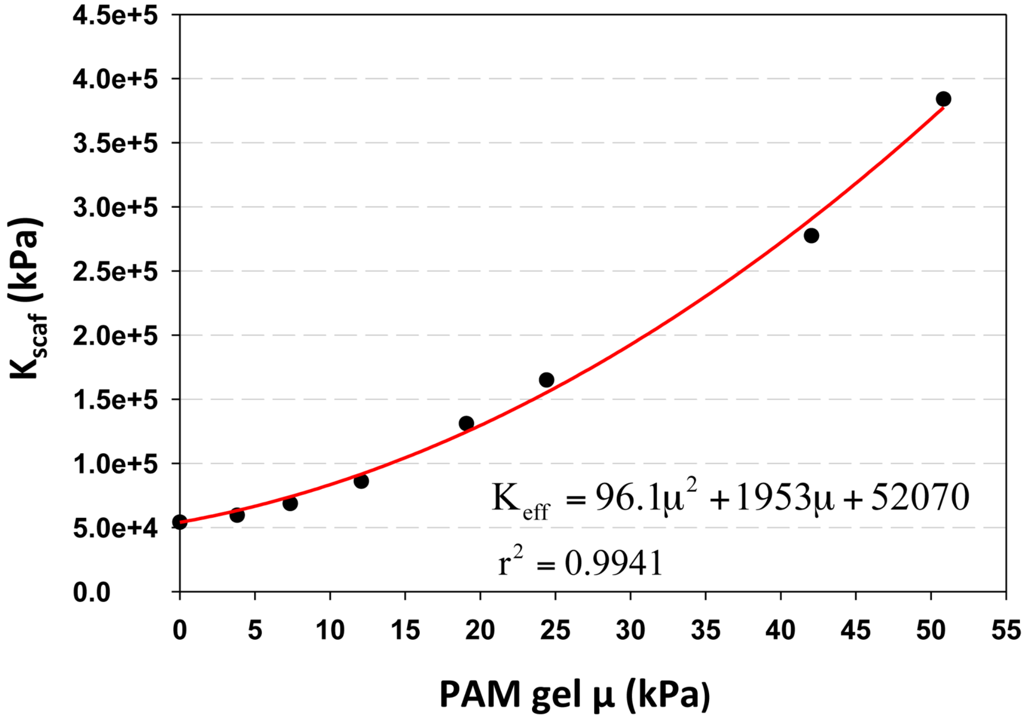

Figure 4.5. Effective PGA:PLLA fiber stiffness vs. PAM gel shear modulus. The effective fiber stiffness is volume fraction corrected. The red line represents a quadratic fit to the data.

4.3.3 Validation of continuous scaffold fiber constitutive model

Using the biaxial mechanical data of continuous scaffold fibers embedded in PAM gels of known shear modulus values, the continuous scaffold model was used to estimate the matrix shear modulus. In this manner, the estimated matrix shear modulus could be compared directly with the known shear modulus value to assess the predictive capability of the model.

Figure 4.6 shows the estimated matrix shear modulus plotted against the known shear modulus for a given group of scaffold-PAM gel composites. Note that the estimated shear modulus values are presented as mean +/- SEM for all groups. A line with a slope of unity is also plotted, indicating perfect agreement between estimated and actual results.

Table 4.3 also shows the model parameters and quality of fit for each tested specimen. For the smaller matrix shear modulus values (7.35, 12, and 24 kPa), the model predicts shear modulus values of 1.85 kPa +/- 0.51 kPa, 16.2 kPa +/- 4.96 kPa, and 20.3 kPa +/- 2.04 kPa for the three groups, respectively. For the larger matrix shear values of 42 kPa and 50.8 kPa, the model predicts values of 39.2 kPa +/- 2.96 kPa and 50.5 kPa +/- 3.81 kPa. To address the discrepancy between estimated and actual shear modulus values, a cubic polynomial fit to the estimated data was performed yielding a relationship of:

$$\mu_{\text{pred}} = c_1\mu^3 + c_2\mu^2 + c_3\mu . \tag{4.7}$$

With this relationship, it was possible to more accurately predict the matrix shear modulus in the current model form (i.e. not considering matrix-scaffold shearing interactions).

Table 4.3. Estimated shear modulus values and model parameters using discontinuous scaffold model.

Implant Length	ID	μ (kPa)	ϕ_1 (deg)	Shear (deg)	Rotation (deg)	k_{eff} (kPa)	SSE	R^2_{11}	R^2_{22}
3.8 kPa	1	1.834	11.00	0.28	0.84	4070	2748	0.8394	0.9801
3.8 kPa	2	1.241	10.54	0.47	0.62	3972	3286	0.8683	0.9676
3.8 kPa	3	3.291	-11.00	1.39	0.06	4329	3249	0.8835	0.9602
3.8 kPa	4	1.036	11.00	1.49	1.09	3939	5318	0.7364	0.9606
	MEAN	**1.851**	**5.39**	**0.91**	**0.65**	**4078**	---	---	---
	SEM	**0.509**	**5.46**	**0.31**	**0.22**	**88**	---	---	---
7.35 kPa	1	16.014	8.76	1.13	1.55	7687	2615	0.8894	0.9717
7.35 kPa	2	24.887	11.53	0.45	1.69	11080	3586	0.8433	0.9589
7.35 kPa	3	7.720	11.00	0.14	2.01	5268	1951	0.9094	0.9755
	MEAN	**16.207**	**10.43**	**0.57**	**1.75**	**8012**	---	---	---
	SEM	**4.957**	**0.85**	**0.29**	**0.14**	**1686**	---	---	---
12.1 kPa	1	21.832	-6.78	0.79	0.89	9793	2921	0.8449	0.9733
12.1 kPa	2	13.123	-10.54	0.93	0.75	6724	2062	0.9081	0.9728
12.1 kPa	3	18.689	9.32	0.28	0.69	8583	1199	0.9319	0.9919
12.1 kPa	4	23.953	-11.51	0.15	0.82	10675	2146	0.8907	0.9827
12.1 kPa	5	23.967	11.00	0.07	0.75	10681	4002	0.7652	0.9875
	MEAN	**20.313**	**-1.70**	**0.45**	**0.78**	**9291**	---	---	---
	SEM	**2.040**	**4.91**	**0.17**	**0.04**	**748**	---	---	---
24.4 kPa	1	31.303	7.74	0.13	0.54	14140	3275	0.8949	0.9257
24.4 kPa	2	34.340	-9.93	0.38	0.64	15757	1843	0.9501	0.9723
24.4 kPa	3	34.439	8.05	0.06	0.02	15812	6359	0.7297	0.9109
	MEAN	**33.361**	**1.95**	**0.19**	**0.40**	**15236**	---	---	---
	SEM	**1.029**	**5.94**	**0.10**	**0.19**	**548**	---	---	---
42.0 kPa	1	47.859	-11.00	0.18	0.30	24267	7277	0.8291	0.8881
42.0 kPa	2	35.228	-8.23	0.31	1.98	16250	1102	0.9640	0.9814
42.0 kPa	3	38.201	10.22	0.10	1.86	17986	3308	0.8972	0.9321
42.0 kPa	4	35.514	-9.57	0.31	0.61	16411	3854	0.8946	0.9218
	MEAN	**39.200**	**-4.65**	**0.23**	**1.19**	**18729**	---	---	---
	SEM	**2.963**	**4.99**	**0.05**	**0.43**	**1887**	---	---	---
50.8 kPa	1	57.866	11.00	0.08	0.14	32724	3441	0.8249	0.9971
50.8 kPa	2	48.690	7.43	0.20	0.86	25322	4586	0.7769	0.9553
50.8 kPa	3	45.059	-9.51	0.26	1.71	22687	3921	0.8442	0.9386
	MEAN	**50.538**	**2.97**	**0.18**	**0.90**	**26911**	---	---	---
	SEM	**3.811**	**6.33**	**0.05**	**0.45**	**3004**	---	---	---

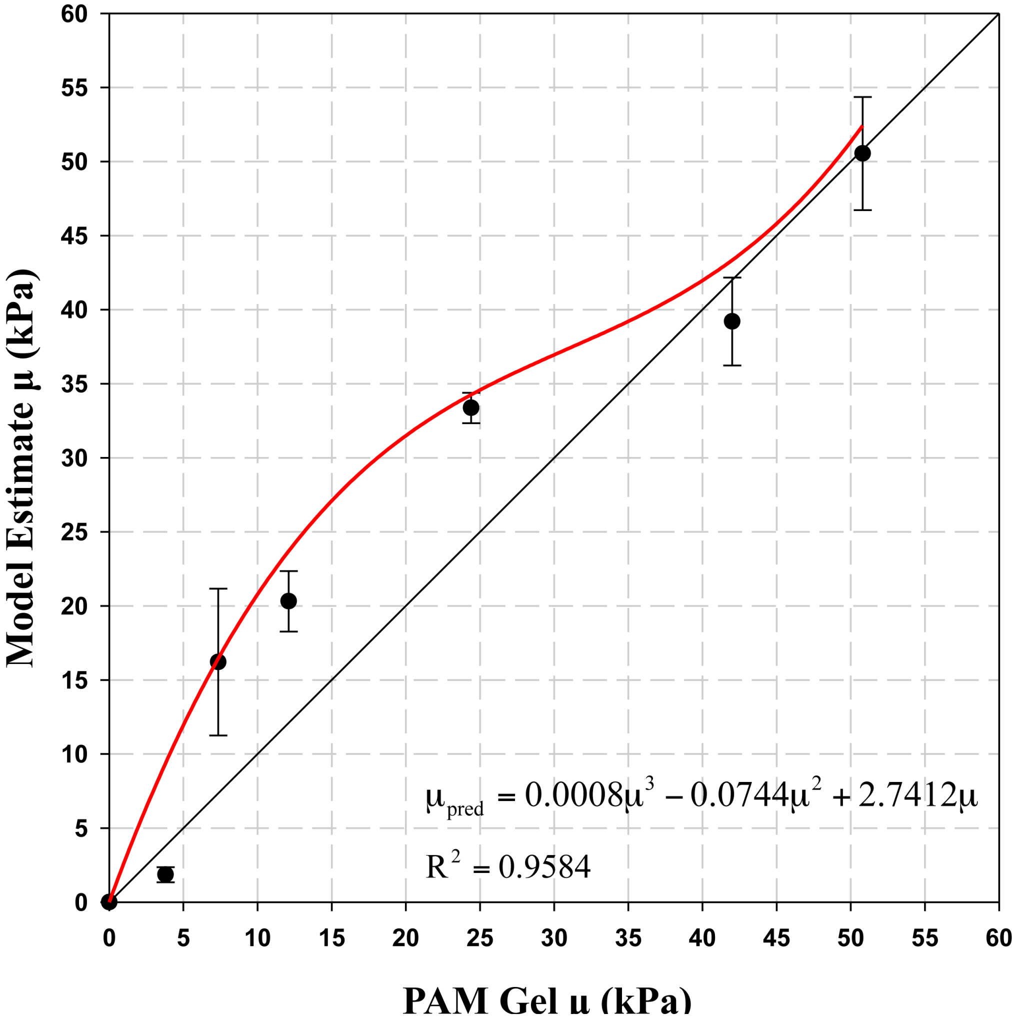

Figure 4.6. Mean +/- SEM model predicted matrix shear modulus versus actual shear modulus for scaffold-embedded PAM gel. N=3 for groups. Red line indicates fit to model predicted data to estimate matrix-scaffold shearing effects.

4.3.4 Validation of long implant duration (discontinuous scaffold fiber) constitutive model

The milling process was able to produce short fibers from intact PGA:PLLA scaffold efficiently and without issues. Observations using a stereomicroscope (not shown) showed fairly uniform fiber lengths that maintained a cylindrical geometry. Embedding fragments into PAM gels did not pose any issues. Figure 4.7 shows a bar plot of mean +/- standard error of the mean shear modulus values computed for each monomer concentration with and without the addition of fragmented gel. In all cases, no statistical difference existed between pairs of embedded/unembedded PAM gels. PAM gel shear modulus as a function of monomer concentration followed the same trend shown in section 4.3.1 and Figure 4.2.

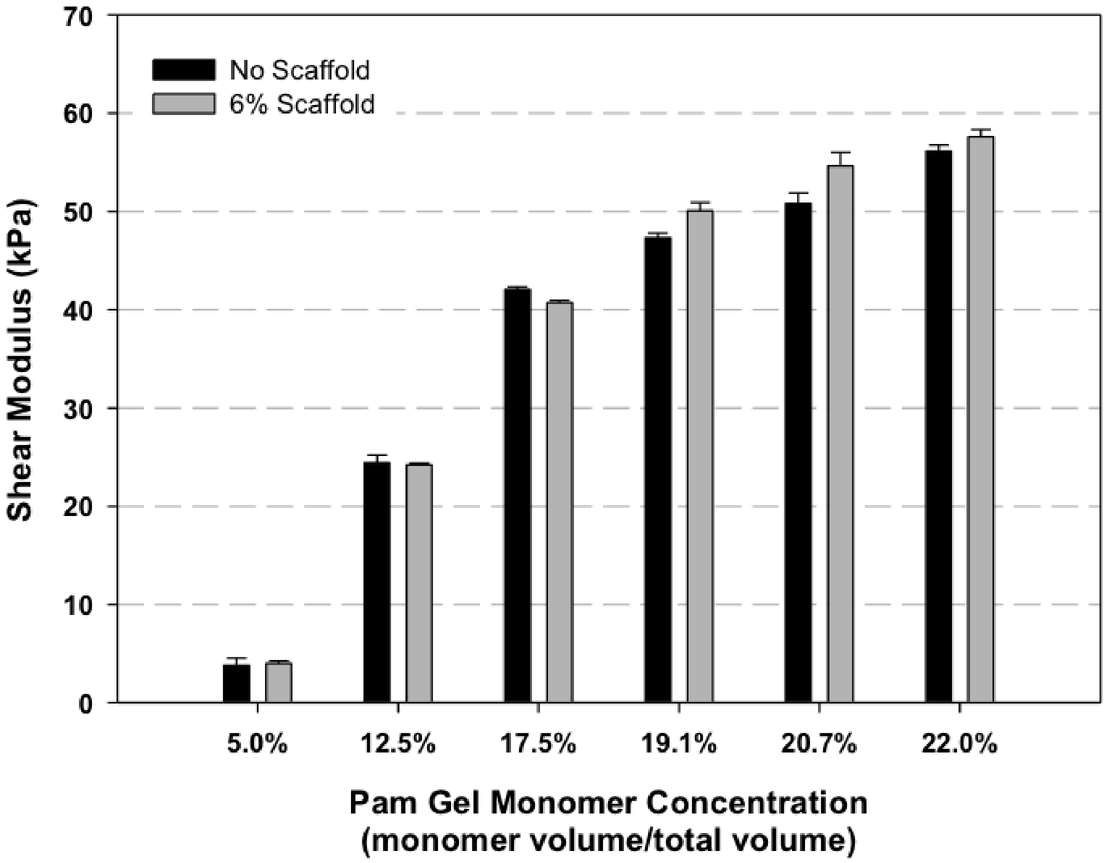

Figure 4.7. PAM gel shear modulus with and without randomly oriented embedded PGA:PLLA scaffold fragments. N=5 for each group, mean +/- SEM.

4.4 DISCUSSION

4.4.1 Use of PAM gel as tunable system analog

Although PAM gel has been used previously as a tissue analog on continuous scaffolds [23], this is the first known work to use PAM gel for both continuous and discontinuous scaffold systems. In all of the experiments, the PAM gel was exceptionally consistent in mechanical properties and exhibited very little variance between samples in particular groups. During testing, no visible signs of decoupling were observed between the PAM gel and scaffold; in fact, when the composites were trimmed, the interface remained intact at the boundaries. The range of shear modulus properties (~4 kPa to ~55 kPa) was adequate for simulating forming and remodeling tissue. Using conservative estimates from traditional linear continuum theory, the approximate elastic modulus range is ~12 kPa to 165 kPa, which is within the range of formed tissue on PGA:PLLA scaffolds shown by Engelmayr and Sacks [23]. Based on ease of fabrication, ability to form a coherent and intact matrix around PGA:PLLA scaffold, and tunable native-like mechanical properties, the PAM gel tissue analog serves as a valuable tool in understanding how tissues form and remodel on scaffold materials.

4.4.2 Validation of the constitutive models

For the continuous model form presented in section 3.3.3, the experimental results using PAM gel and intact continuous PGA:PLLA scaffold provided a means to both estimate matrix-scaffold interaction parameters and validate the model form. Overall, the correlation between the model-estimated and known matrix shear modulus values was strong, notably at larger matrix shear modulus values. Further, the model was able to fit the data with a large quality of fit value for nearly all data sets, indicating that both good quality fits could be achieved that provided accurate shear modulus values. In the fitting process, the matrix shear modulus and two fiber orientation parameters (the orientation mean and rigid-body rotation offset) were allowed to vary. Since alignment of the preferred direction with the X_1 axis in the biaxial testing device may have had some error associated with it (alignment was approximate, not exact), it was felt such freedom should be permitted in the model fitting to accommodate ~10 degree changes in the mean. Additionally, the offset parameter allows for any workless rigid-body rotation of the scaffold occurring during tare load application. It should be noted that this current work extends the original observations from Engelmayr and Sacks to a fully generalized finite deformation framework that is more realistic to soft tissues that tissue engineering aims to emulate. With this, it is felt greater applicability to different scaffold systems can be accommodated with this model form.

For validation of the discontinuous model, the current work has illustrated the insignificant role the fragmented scaffold phase has on the overall composite mechanical properties. Importantly, the theoretical and experimental framework in section 3.4.5 and section 3.4.6 should be performed to ensure such assumptions are valid when the scaffold geometry or material significantly changes. In these cases, it is possible that the scaffold phase may contribute to the overall composite.

4.4.3 Scaffold-ECM interactions in continuous scaffold fiber model

In the continuous scaffold model, the effective fiber stiffness and matrix shear modulus displayed a strong quadratic relationship with small increases in matrix shear modulus having a profound impact on the overall effective scaffold fiber properties. Previously, Engelmayr and Sacks showed a similar relationship between matrix elastic modulus and scaffold elastic modulus undergoing small deformations during flexure [9]. In this work, a structural constitutive model was developed and used to show that decreased fiber-fiber bond distance as facilitated by matrix depositions was a possible means of this reinforcement. The use of equistrain data in this work helps isolate the effects of fiber extension (and hence effective stiffness) as a function of matrix shear modulus. Further, the mathematical framework of the model form allows for additional interaction terms to be easily added as additional work on the model or as dictated by the particular scaffold in use.

The overestimation of the matrix shear modulus in the lower PAM gel shear modulus groups suggests that additional interaction terms exist for which the model currently does not encompass. Likely, these effects are due to shearing between the matrix and fiber via fiber rotation as shown in similar work on the native annular disc [98]. At slightly larger matrix shear modulus values, the correlation between estimated and actual matrix shear modulus is nearly unity, indicating that any additional interaction effects are secondary to the extensional interaction effects characterized in the current formulation.

4.4.4 Scaffold-ECM interactions in long implant duration model

Both the theoretical “best case” critical length estimate from section 3.4.4 and the PAM gel with embedded fragmented scaffold experiments reveal that the scaffold fibers, even at lengths double what were observed in vivo (section 2.3.3), are not capable of having the composite stresses transferred to them. The substantial mismatch between scaffold modulus and tissue modulus plays a role in this process. Even with a relatively stiff tissue phases, the fiber can still be over

100 times stiffer than matrix. This forces a longer critical length, which is beyond those lengths measured in section 2.3.3. Further, the fiber-matrix interface stress plays a substantial role in stress transfer is likely the limiting factor. If stiffer matrix materials are not fully bonded to the fiber phase, they will still be unable to transfer stress and hence be reinforced by the fiber phase. It is important to consider the non-negligible fiber volume fraction that could exist in specimens of interest. Despite the inability of the short fibers to contribute to the overall mechanical properties, they do represent a distinguishable phase within the composite and produce the opportunity to underestimate the mechanical contributions of the tissue phase if such values are not accounted for (the presence of scaffold reduces the overall volume fraction of tissue).

4.4.5 Limitations

A possible limitation in this work is the use of PAM gel to simulate the full range of native soft tissue properties. Though not claimed to encompass all tissues encountered in tissue engineering, it should be noted that PAM gel is not applicable to every tissue system. Despite this, the range of properties used in this study fell within the range determined from similar previous work on tissue engineered cardiovascular tissue using PGA:PLLA scaffolds and was deemed appropriate for this work. Additionally, the other constraints imposed in developing a tissue analog system (tunable mechanical properties, ability to embed scaffold without degrading it, relatively low safety concerns) helped drive the selection of PAM gel. Another limitation is the discrepancy between estimated and known matrix shear modulus values at low ranges. From the mathematical framework described in section 3.3.3, it is anticipated that such discrepancies are due to additional interaction terms between the scaffold and matrix. In the current work, it was not feasible to explore all of the interactions. The strong effect of increased matrix shear modulus on the effective scaffold fiber modulus is likely the dominant effect, with additional interactions secondary. These effects cannot be entirely ignored, however, and are the focus of future modeling work.

Finally, the discontinuous model form was simplified due to the decoupling between scaffold and matrix phases as shown theoretically and experimentally. Though this was convenient in the current work, it is expected that this may not be the case in every scaffold-matrix system encountered. Again, as expressed previously, it will be necessary to work through the theoretical framework established in section 3.4.4 and perform validation experiments as in section 4.2.8 to confirm the insignificant role of the discontinuous scaffold phase in the overall composite response in other systems.

4.5 CONCLUSION

In this work, the structural constitutive models developed in chapter 3 were applied to a tunable tissue analog system using PAM gel. In both models, the effects of the continuous and discontinuous scaffold phases were explored. The strong relationship between effective scaffold fiber stiffness and matrix shear modulus was shown in the continuous model formulation. Additionally, the model was shown to estimate the matrix shear modulus accurately. In this discontinuous model, the theoretically-based assumptions were confirmed experimentally using fragmented PGA:PLLA scaffold embedded in PAM gel. In summary, the underlying assumptions guiding both models were validated using the PAM gel tunable tissue analog system.

5.0 TISSUE FORMATION AND REMODELING IN TISSUE ENGINEERED PULMONARY CONDUITS

5.1 INTRODUCTION

As the clinical drive for the development of the structural constitutive model formulations in chapter 3, improved means of understanding tissue formation and remodeling in engineered tissues is necessary to further the field and ultimately develop functionally-equivalent tissues. Tissue engineering of the pulmonary conduit is chosen as a system of study in this work, as it presents a definite clinical need and a established platform of study within our laboratory.

Each year, nearly 30,000 children are born in the United States with congenital heart defects [32]. Such defects can manifest in a variety of manners, including tetralogy of Fallot, hypoplastic left heart syndrome, tricuspic atresia, pulmonary stenosis, and pulmonary atresia. Slightly less than half of patients require surgical correction via partial or full reconstruction of the pulmonary artery/right ventricular outflow tract to establish normal anatomy and restore proper blood flow [33, 34]. Unfortunately, current options for conduit grafts are limited, suffer from thrombogenesis, infection, and calcification [37-40], and are rendered inert and are thus unable to repair, remodel or somatically grow with the patient (requiring additional operations as the patient grows). It is clear that a clinical need exists to develop better conduit therapies for PA/RVOT reconstruction.

There exists a paucity of published research on tissue engineered conduits (TECs), and within the limited work, variation exists among cell types, scaffold materials, culturing techniques, and subsequent analysis, making efforts to understand the overall functional equivalency of TECs and the factors that prominently influence results less clear. Often, little mechanical testing is performed with only bulk assays (collagen, calcium), geometric measurements, and histology used to evaluate the TECs [42, 43]. Though some long-term results have been encouraging, most TEC work is empirically based, limited in scope, and has not elucidated time course changes in structure and mechanical behavior necessary to properly evaluate tissue formation and remodeling. It is the intent of this work to make use of the developed structural constitutive models from chapter 3 (guided from quantitative structural information from chapter 2) and the validation/parameter estimation information from chapter 4 to elucidate how tissue forms and remodels in TECs.

5.2 METHODS

5.2.1 Tissue engineered conduit fabrication and implantation

As part of an existing study [45], all in vitro and in vivo specimens were supplied by the Mayer Laboratory, stored and frozen in PBS, shipped overnight, and stored in a -80^{o}C freezer until use. Cell isolation, culturing, and seeding, along with scaffold preparation and implantation was performed as described in previous work [45]. For these specific specimens, bone marrow was obtained at five and six week age timepoints from female Dorset sheep (approximately four weeks of age at 10 kg) from the iliac crest of the animals. Animals were cared for as per the "Guide for the Care and Use of Laboratory Animals," and the Institutional Animal Care and Use

Committee of Children's Hospital approved the protocol. The bone marrow was centrifuged and the mononuclear fraction was plated in medium containing DMEM with high glucose, 10% fetal bovine serum, 10% autologous serum, 10 mM HEPES buffer, and 1x antibiotic/antimycotic solution. Based on adherence to tissue culture plates, Mesenchymal stem cells were isolated, passaged, and expanded in basal medium supplemented with DMEM with high glucose, 10% fetal bovine serum, 10 mM HEPES buffer, and 1x antibiotic/antimycotic solution. Cells were expanded and passaged every three days until approximately 1 billion cells were available per each specimen planned.

Sheets of non-woven 50:50% PGA:PLLA co-polymer (Concordia Medical) were manually assembled into a valved conduit based on normal ovine RVOT dimensions. The valved conduits were then mounted onto gaskets and sewn circumferentially into a custom-built tension device to maintain conduit geometry during culturing. Scaffold assemblies were sterilized with ethylene oxide gas, pre-wet with 70% ethanol, washed with PBS three times, and immersed in a 90% fetal bovine serum / 10% antibiotic/antimycotic solution for 1-2 hours. Cells were then seeded on the approximately 80 cm^2 scaffold at a density of 0.5-1.7x 10^7 cells/cm^2 by adding the cells into the mounted scaffold assemblies. The scaffold was rotated at 1rpm in 60ml of medium containing DMEM high glucose, 20% fetal bovine solution, 10% autologous sheep serum, 2x antibiotic/antimycotic solution, 10 mM HEPES buffer, 82 μg/ml ascorbic acid-2-phosphate, and 2 ng/ml of bFGF. After 72 hours, the assembly was removed from the glass bottle and placed in a 850 cm2 roller bottle containing 500ml of medium (as described above without sheep serum). For 1 month, the medium was changed every three days.

A total of 21 valved pulmonary conduit assemblies were created using the procedure described above. For implantation, anesthesia was induced with intramuscular ketamine (50 mg/kg) and continued with inhalational isoflurane. A left thoracotomy at the fourth intercostal space was performed, and under cardiopulmonary bypass, the native PV and a 1-2 cm segment of the main pulmonary artery were excised. The seeded valve and conduit assembly was sewn into place. Epicardial echocardiography was performed to evaluate valve function during implantation. The chest was closed, and the animal was transferred to a recovery sling, allowed to recover until hemodynamically stable, woken from anesthesia, extubated, and returned to its cage.

At each experimental endpoint (1,7,42,84, and 140 days), the same methods used for implantation were employed. The animals were exsanguinated, and the heart and lungs were removed after cardiac arrest. The conduit assemblies were explanted; each assembly was cut into three equal-sized radial strips that included portions of the associated conduit, resulting in a total of 63 specimens. Three strips per conduit were stored and frozen in PBS and shipped to our laboratory for further analysis. A total of 17 animals were involved in this study (five with 1 day implants and three each with 7,42,84, and 140 day implants), and two non-implanted (0 day implant) specimens were made available. Based on sectioning into strips, a total of four 0 day implant, eleven 1 day implant, eight 7 day implant, three 42 day implant, five 84 day implant, and six 140 day implant conduit specimens were available (not all specimen strips could be utilized due to geometry). Note that because conduits were created from three separate seeded panels, strips from each panel were considered unique specimens.

5.2.2 Biaxial tensile testing protocol

Biaxial tensile mechanical testing was performed on segments of specimen conduit from short implant durations (Table 5.1) and long implant durations (Table 5.2). Since leaflet-conduit portions were cut into thirds, some specimens were too small (less than 4 mm per side) to be biaxially tested. In some specimens, leaflets were fused to the conduits. In these cases, regions of conduit beyond the fused leaflets were used for mechanical testing. Following previously published methods for biaxial mechanical testing [30], tissue specimens were cut to provide maximum size, often rectangular in shape ranging from 5-7 mm per side. Thickness measurements were taken using a micrometer at six locations on specimens and averaged. Stainless steel 0.016 inch diameter hooks tied to both ends of 10 cm long silk suture line were attached to specimens with four hooks per side forming two loops of suture. A total of sixteen hooks were placed creating four pairs of sutures. Four small cut portions of polyproline suture were attached to the middle region of the specimen in a square pattern using cyanoacrylate glue to serve as fiducial markers for strain tracking. The specimen was then placed in the PBS-filled (tissue) biaxial testing device chamber, and the silk suture loops were attached to stainless steel dowels on actuator arms. The circumferential direction was aligned with the X_1 axis on the device to maintain consistency between tests.

Table 5.1. Early implant duration TEC specimen database for biaxial and uniaxial mechanical testing.

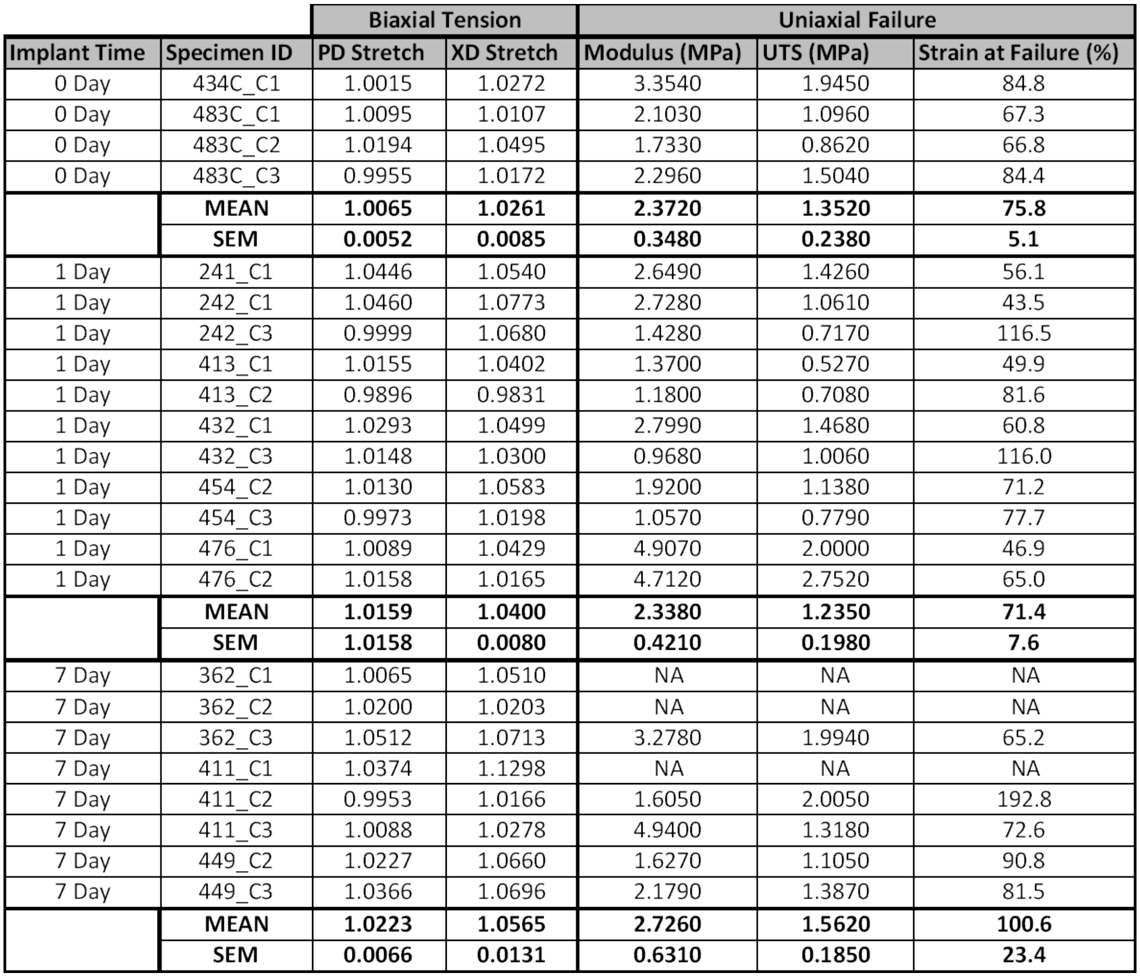

		Biaxial Tension		Uniaxial Failure		
Implant Time	**Specimen ID**	**PD Stretch**	**XD Stretch**	**Modulus (MPa)**	**UTS (MPa)**	**Strain at Failure (%)**
0 Day	434C_C1	1.0015	1.0272	3.3540	1.9450	84.8
0 Day	483C_C1	1.0095	1.0107	2.1030	1.0960	67.3
0 Day	483C_C2	1.0194	1.0495	1.7330	0.8620	66.8
0 Day	483C_C3	0.9955	1.0172	2.2960	1.5040	84.4
	MEAN	**1.0065**	**1.0261**	**2.3720**	**1.3520**	**75.8**
	SEM	**0.0052**	**0.0085**	**0.3480**	**0.2380**	**5.1**
1 Day	241_C1	1.0446	1.0540	2.6490	1.4260	56.1
1 Day	242_C1	1.0460	1.0773	2.7280	1.0610	43.5
1 Day	242_C3	0.9999	1.0680	1.4280	0.7170	116.5
1 Day	413_C1	1.0155	1.0402	1.3700	0.5270	49.9
1 Day	413_C2	0.9896	0.9831	1.1800	0.7080	81.6
1 Day	432_C1	1.0293	1.0499	2.7990	1.4680	60.8
1 Day	432_C3	1.0148	1.0300	0.9680	1.0060	116.0
1 Day	454_C2	1.0130	1.0583	1.9200	1.1380	71.2
1 Day	454_C3	0.9973	1.0198	1.0570	0.7790	77.7
1 Day	476_C1	1.0089	1.0429	4.9070	2.0000	46.9
1 Day	476_C2	1.0158	1.0165	4.7120	2.7520	65.0
	MEAN	**1.0159**	**1.0400**	**2.3380**	**1.2350**	**71.4**
	SEM	**1.0158**	**0.0080**	**0.4210**	**0.1980**	**7.6**
7 Day	362_C1	1.0065	1.0510	NA	NA	NA
7 Day	362_C2	1.0200	1.0203	NA	NA	NA
7 Day	362_C3	1.0512	1.0713	3.2780	1.9940	65.2
7 Day	411_C1	1.0374	1.1298	NA	NA	NA
7 Day	411_C2	0.9953	1.0166	1.6050	2.0050	192.8
7 Day	411_C3	1.0088	1.0278	4.9400	1.3180	72.6
7 Day	449_C2	1.0227	1.0660	1.6270	1.1050	90.8
7 Day	449_C3	1.0366	1.0696	2.1790	1.3870	81.5
	MEAN	**1.0223**	**1.0565**	**2.7260**	**1.5620**	**100.6**
	SEM	**0.0066**	**0.0131**	**0.6310**	**0.1850**	**23.4**

Table 5.2. Long implant duration TEC specimen database for biaxial and uniaxial mechanical testing.

		Biaxial Tension		Uniaxial Failure		
Implant Time	**Specimen ID**	**PD Stretch**	**XD Stretch**	**Modulus (Mpa)**	**UTS (MPa)**	**Strain at Failure (%)**
42 Days	434_C2	1.0430	1.0696	0.621	0.858	59.30
42 Days	448_C3	1.0036	1.0482	0.714	0.805	60.32
42 Days	483_C2	0.9781	1.0839	0.508	0.881	39.01
	MEAN	**1.0082**	**1.0672**	**0.614**	**0.848**	**52.88**
	SEM	**0.0189**	**0.0104**	**0.060**	**0.023**	**6.94**
84 Days	376_C1	1.0072	1.0225	3.448	2.462	107.1
84 Days	376_C3	1.0268	1.0371	NA	NA	NA
84 Days	418_C1	0.9837	1.0352	NA	NA	NA
84 Days	418_C2	1.0058	1.1179	3.760	3.197	208.7
84 Days	418_C3	1.0128	1.0666	3.564	2.378	98.6
	MEAN	**1.0073**	**1.0559**	**3.591**	**2.679**	**138.1**
	SEM	**0.0070**	**0.0171**	**0.091**	**0.260**	**35.35**
140 Days	253_C1	1.0325	1.0636	NA	NA	NA
140 Days	347_C1	1.0061	1.0372	2.699	2.470	177.0
140 Days	347_C2	1.0553	1.0721	NA	NA	NA
140 Days	347_C3	1.0302	1.0552	3.558	4.380	150.4
140 Days	361_C1	1.0420	1.0723	5.970	4.135	107.6
140 Days	361_C2	1.0201	1.0293	NA	NA	NA
	MEAN	**1.0310**	**1.0550**	**4.076**	**3.662**	**145.0**
	SEM	**0.0070**	**0.0074**	**0.979**	**0.600**	**20.21**

Using custom-written control software, load control biaxial mechanical testing was performed. Free-floating (no-load) reference states were taken before preconditioning, after preconditioning, and after full protocol testing. A 0.2 gram tare load was applied to the specimen to enable proper device operation. Tare reference states before preconditioning, after preconditioning, and after full protocol testing were also taken. Preconditioning was performed for ten cycles with a fifteen second half cycle time. In all specimens it was found that ten cycles of preconditioning was adequate to ensure consistent loading results from subsequent tests. A seven protocol testing regime was used with peak X_1:X_2 stress ratios of 15:50, 25:50, 37.5:50, 50:50, 50:37.5, 50:25, and 50:15 kPa. Tests were performed for ten cycles with a fifteen second half cycle time. Following testing, tissue specimens were removed, placed in PBS, and frozen.

5.2.3 Biaxial tensile testing data analysis

A described in section 4.2.5, a finite-element based surface interpolation technique using a four-node linear Lagrangian element was employed to determine the two-dimensional in-surface Eulerian strain tensor at each time point [30]. In order to reference the deformed state configuration and calculate the strain tensor, a convective, in-surface coordinate system was used in which the axes were aligned to the local longitudinal and circumferential directions of the conduit. In this analysis, the Eulerian strain tensor components were computed at each load iteration. Additionally, the first and second Piola-Kirchhoff stresses were computed using the deformation gradient tensor. In all analyses, the post-preconditioned free-floating condition was used as the reference state

5.2.4 Uniaxial failure testing protocol

As shown in Table 5.1 and Table 5.2, conduit portions of specimens were tested to uniaxial failure. Though not physiological, such testing provides a means to evaluate ultimate tensile strength and compare results to other published data. For uniaxial testing, radial strips of specimens were cut to 3 mm wide by 4-6 mm long. Thickness measurements were taken at six points on the specimen and averaged. Using the MTS Triton 2500 testing device, specimens were loaded between sandpaper-coated grips on the device. A small preload of 0.05 N was applied to the specimens to provide a uniform starting point for all specimens. The gage length (distance between grips) was recorded. Specimens were cyclically loaded for five cycles to 5% strain and then loaded to failure.

5.2.5 Uniaxial failure testing data analysis

A custom-written Mathcad analysis program was used to compute the ultimate tensile strength (UTS) and linear elastic modulus for each specimen. Specimen dimensions were manually entered into the program to determine specimen cross-sectional area based on a rectangular geometry. From this, the average stress was determined as:

$$\sigma_{avg} = \frac{F}{A} \quad , \tag{5.1}$$

where F is the applied instantaneous load and A is the initial cross-sectional area. The average linear strain was found as:

$$e_{avg} = \frac{D_g - D_{g0}}{D_{g0}} \quad , \tag{5.2}$$

where D_g is the instantaneous grip-to-grip distance (gage length) and D_{g0} is the initial gage length. A first-order polynomial was fit to the linear region of the average stress – average linear strain data between onset of loading and prior to the peak loading point, and the first derivative of this polynomial was outputted as the linear elastic modulus. The UTS was taken as the peak stress prior to specimen failure and outputted as well.

5.2.6 Histology

For the short implantation duration TECs, histology was performed to evaluate the overall structure of the composites at the pre-implant, 1 day, and 7 day timepoints. Specimens were embedded in paraffin and cut along the tissue longitudinal direction to approximately 7-10 μm thick. These transmural sections were mounted on glass slides and stained with H&E to reveal non-specific ECM, cell nuclei, and scaffold. Photoshop CS5 (Adobe Systems Incorporated, San

Jose, CA) was used to segment out scaffold and selectively mask tissue from non-tissue regions. Pixel area was computed for tissue and scaffold components across a uniform cross-section of each imaged specimen. For 7 day specimens, sections were taken in 10 μm intervals as per the results from section 2.3.5 to determine if scaffold area was preserved through the volume and thus potentially permit area fraction to provide a reasonable approximation of volume fraction as in the pre-implant and 1 day specimens.

To assess important structural details such as scaffold volume fraction and constituent orientation in the long implant duration TECs, both en face and transmural sections were cut from conduit specimens. All specimens at 42, 84, and 140 days post-implant were used for en face sectioning, with sections taken at three locations within the specimen: within 50 μm from the inner surface, approximate middle region, and within 50 μm from the outer surface. A section of 30 μm was taken for small angle light scattering (SALS) analysis at all regions for all specimens. Additionally at each regional location in two specimens from each timepoint group, two 5 μm sections were taken and stained with either H&E or picrosirius red. Transmurally-cut H&E stained sections for specimens at 42, 84, and 140 days post-implant timepoints were provided by the Mayer laboratory for scaffold volume fraction analysis. As per the sectioning frequency study in section 2.3.5, collagen area fraction was computed for each en face picrosirius red stained specimen slice. As collagen was the predominant constituent stained by the picrosirius, a simple thresholding procedure in Photoshop CS5 was used on the intensity distribution of each imaged section and used to compute the number of non-background intensity pixels. A ratio between non-background intensity pixels and overall image pixels yielded an area fraction. Since little variation was seen in collagen concentration in the circumferential and radial directions in section 2.3.5, the area fractions were assumed equivalent to volume fractions.

Additionally, polarized light microscopy was performed on picrosirius red stained en face sections of 42, 84, and 140 implant duration specimens. With the use of polarized light, collagen fiber crimp appears as distinct bands.

On the 30 μm thick sections, SALS was used to determine the orientation of structural components within the specimens as described in previous work. The details of the SALS device have been described previously, including its application with fibrous polymer scaffold materials [99, 100]. Briefly, tissue sections were scanned at discrete points along a rectilinear grid using a 255 μm diameter helium-neon laser beam (wavelength of 632.8 nm). All structural information within the light beam envelope was represented by the spatial intensity distribution of the resulting scattered light. From this data, the angular distribution of scattered light pattern (representing the distribution of fiber angles within the light beam envelope) was obtained. A custom written post-processing C++ computer program was used to extract the scattered light intensity distribution from between 150 and 200 random points from the mid regions of scanned specimens. These distributions were averaged over an 180^o angular range (distributions were symmetric about the preferred direction over the full 360^o range) to produce mean intensity distributions. The mean centroid from each specimen's region of interest were computed directly from the averaged intensity distributions providing alignment information, such as how well aligned the structural components were to the preferred directions (given by the centroid). An orientation index was also computed, represented as the width necessary to encompass 50% of all structural components and was normalized based on a 90^o range to provide a normalized orientation index (NOI) as percentage value.

5.2.7 Constitutive model fitting procedure

In the continuous scaffold model, a custom-written Mathcad program (PTC, Needham, MA) was used to fit the biaxial data using a squared error minimization approach using the Levenberg-Marquardt algorithm. As the scaffold-matrix interaction term was expressed as a function of matrix shear modulus, the matrix shear modulus and two scaffold orientation parameters (mean c1 and offset c3) were estimated in the fitting procedure. The standard deviation of the scaffold orientation was set to 31 degrees as reported in previous work and in chapter 3 [9]. Parameters for each specimen fit were outputted along with quality of fit assessments (R^2) for both directions.

In the discontinuous scaffold model, a custom-written fitting code in Mathcad was used to determine the model parameters from the experimental data sets. Parameter bounds were provided for the collagen fiber orientation standard deviation (based on SALS data). Additionally, the upper bound stretch was bounded by a maximum value for each specimen, determined as the ensemble stretch at an angle two standard deviations from the mean (based on SALS data) using eq. (3.39). This way, the upper bound stretch was restricted to a maximum ensemble value encompassing approximately 95% of all collagen fibers. For all data sets, fitting was performed in stages to assist in determining unique parameters sets representing absolute (and no local) minimums. All fitting was performed with respect to the 2nd Piola-Kirchhoff stress with a sum of squared error minimization approach using the Levenberg-Marquardt algorithm. Due to variations within the extreme loading protocols (15:50, 15:50 kPa), only the first five protocols were used for fitting. Parameters for each specimen fit were outputted along with the sum of squared errors from the combined directions.

5.2.8 Statistical analysis

All results are presented as mean +/- standard error of the mean. For statistical analyses performed in this work, one-way ANOVA was utilized with the built in functionality of SigmaPlot 11 (Systat Software Inc., San Jose, CA. An alpha value of 0.05 was used so that statistical significance was assumed if $p < 0.05$. Post-hoc testing was performed using the Student-Newman-Keuls method.

5.3 RESULTS

5.3.1 Biaxial mechanical results of short and long implant duration TECs

Figure 5.1 shows representative biaxial mechanical data for the continuous scaffold fiber TECs plotted alongside representative data from the discontinuous scaffold fiber TEC group. The equibiaxial stress protocol is shown, though the other protocols were acquired with the same level of fidelity. Table 5.1 shows individual specimen and group mean +/-SEM stretch at peak equibiaxial stress (50 kPa) data. Figure 5.2 graphically represents the tabulated data. In the preferred direction, mean +/- SEM stretch at peak equibiaxial stress changed from 1.0065 +/- 0.0052 to 1.0159 +/- 0.0054 to 1.0223 +/- 0.0066 for the 0, 1, and 7 day groups respectively, while mean +/- SEM stretch changed from 1.0261 +/- 0.0085 to 1.0400 +/- 0.0080 to 1.0565 +/- 0.0131 in the cross-preferred direction for the same groups. There were not statistically significant differences between the three groups, though each timepoint showed a statistically significant difference between the preferred and cross-preferred directions.

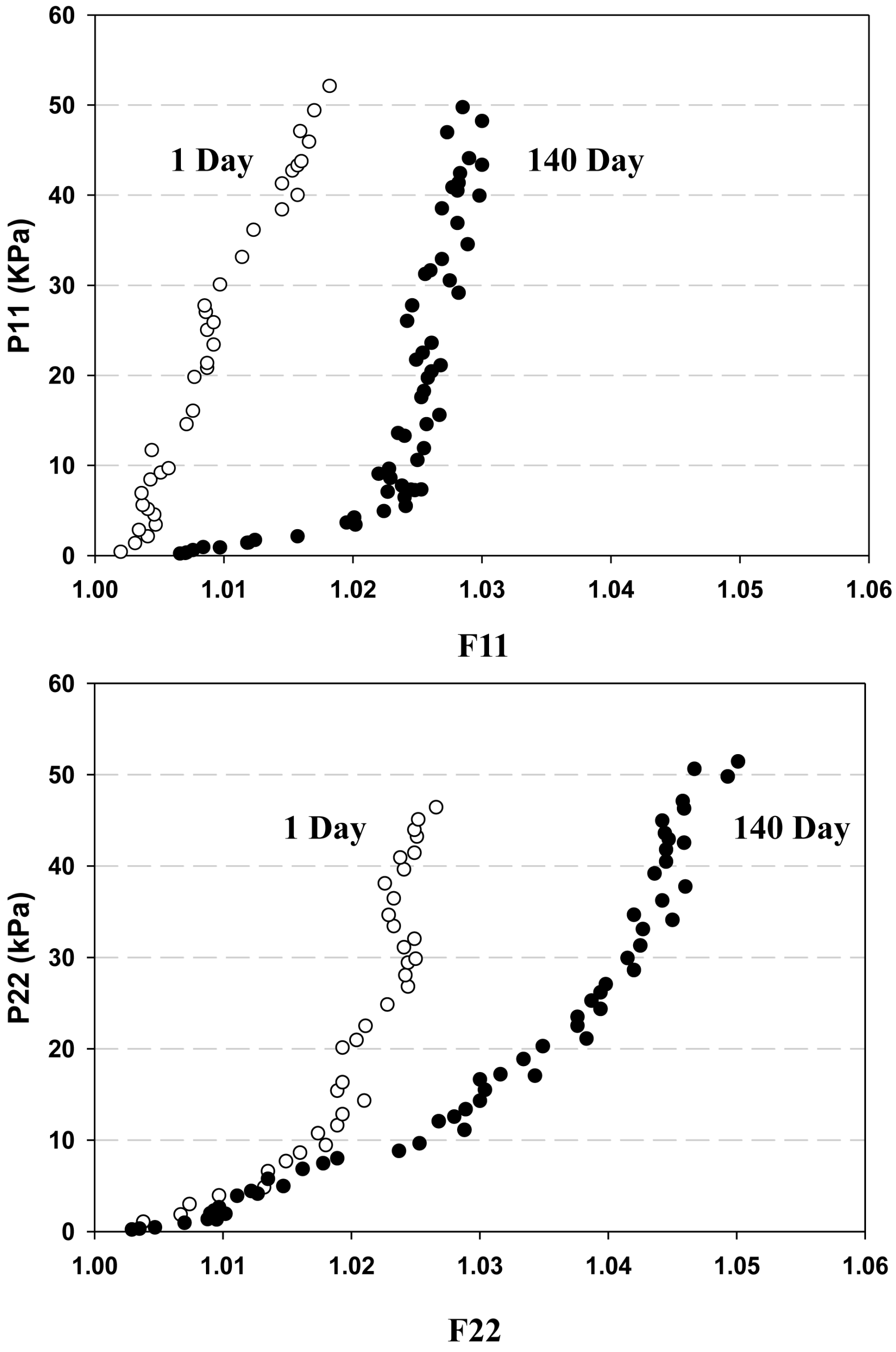

Figure 5.1. Representative equibiaxial stress data from short and long implant duration groups (1 and 140 day). Shown are preferred (PD) and cross-preferred (XD) directions.

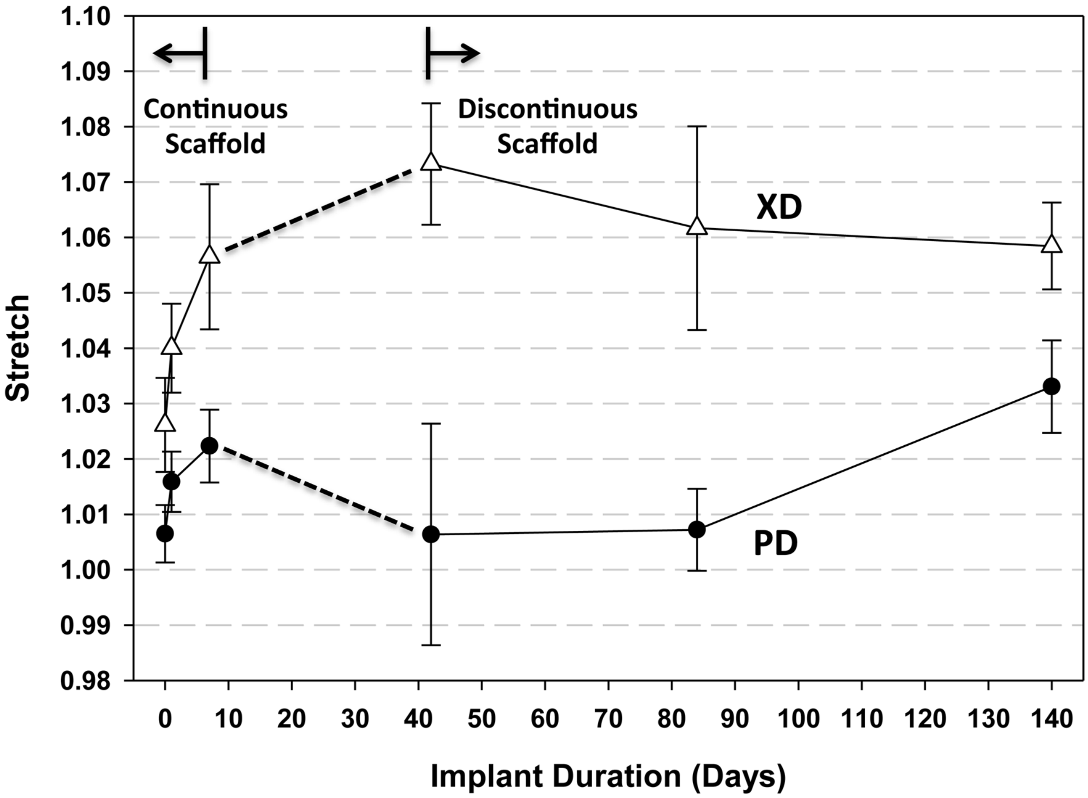

Figure 5.2. Mean +/- SEM stretch at peak equibiaxial stress data for short and long implant duration specimens. PD and XD denote the preferred and cross-preferred directions, respectively.

For the long implant duration TECs, a representative equibiaxial stress data set can be seen in Figure 5.1. Stretch at peak equibiaxial stress (50 kPa) was averaged, tabulated (Table 5.2), and plotted as mean +/- standard error of the mean for both axes for all three implant duration groups (Figure 5.2). Though there was not statistical significance between groups, a general trend can be observed in Figure 5.2. Specifically, a trend towards less anisotropic behavior exists with implant time as the mean stretch in the preferred direction changes from 1.0064 +/- 0.0200 to 1.0072 +/- 0.0007 to 1.0330 +/- 0.0008 with increasing implant time. Mean stretch in the cross-preferred direction changes little with implant time.

5.3.2 Uniaxial failure results of short and long implant duration TECs

A representative uniaxial failure test data is shown in Figure 5.3 for the TECs, displaying a defined linear modulus region and failure stress (ultimate tensile strength). Uniaxial extension data is displayed in Figure 5.4 as three separate subplots showing mean +/- standard error of the mean tangent modulus, strain at failure, and ultimate tensile strength for each of the implant duration groups. Additionally, native pulmonary artery and comparable 140 day timepoint properties from Hoerstrup et al. [31] have been added. For the 0, 1, and 7 day implant durations, the mean tangent modulus show little change from 2.371 MPa +/- 0.348 MPa to 2.281 MPa +/- 0.330 MPa to 2.665 MPa +/- 0.519 MPa. Ultimate tensile strength values of 1.352 MPa +/- 0.238 MPa (0 day), 1.153 +/- 0.161 MPa (1 day), and 1.475 MPa +/- 0.174 MPa (7 day) as well as strain at failure values of 75.8% +/- 5.08% (0 day), 67.3% +/- 6.78% (1 day), and 93.2% +/- 20.5% (7 day) show similar trends of little change in the 0-1 day time period with slight differences by 7 days. No measures have statistically significant differences. For the long duration implants, values increase from 0.614 MPa +/- 0.060 MPa to 3.591 MPa +/- 0.091 MPa and 4.076 MPa +/- 0.979 MPa for the long implant duration groups. A similar trend is observed in the ultimate tensile strength subplot, with values of 0.848 MPa +/- 0.023 MPa, 2.679 MPa +/- 0.260 MPa, and 3.662 MPa +/- 1.450 MPa for the 42, 84, and 140 timepoints. For strain at failure, values change from 52.9% +/-6.94%, 138% +/- 35.4%, and 145% +/- 20.2% for 42, 84, and 140 days post implant.

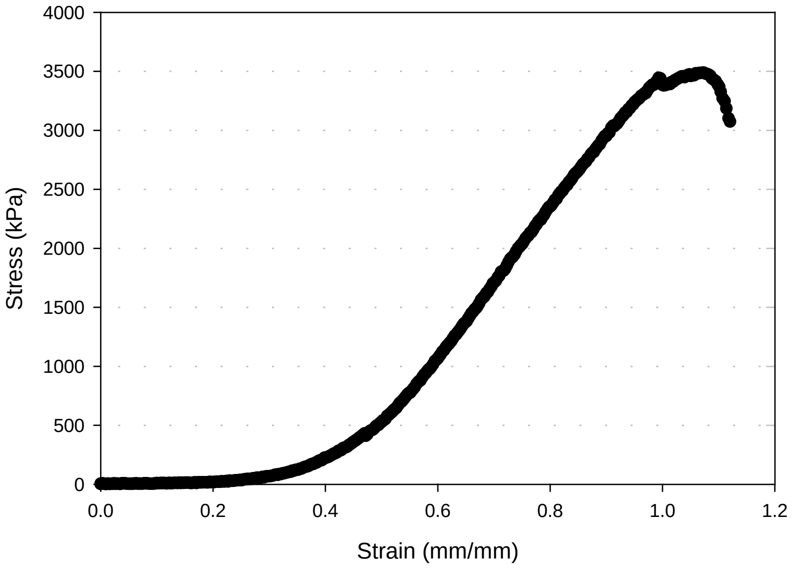

Figure 5.3. Representative uniaxial failure data for TECs.

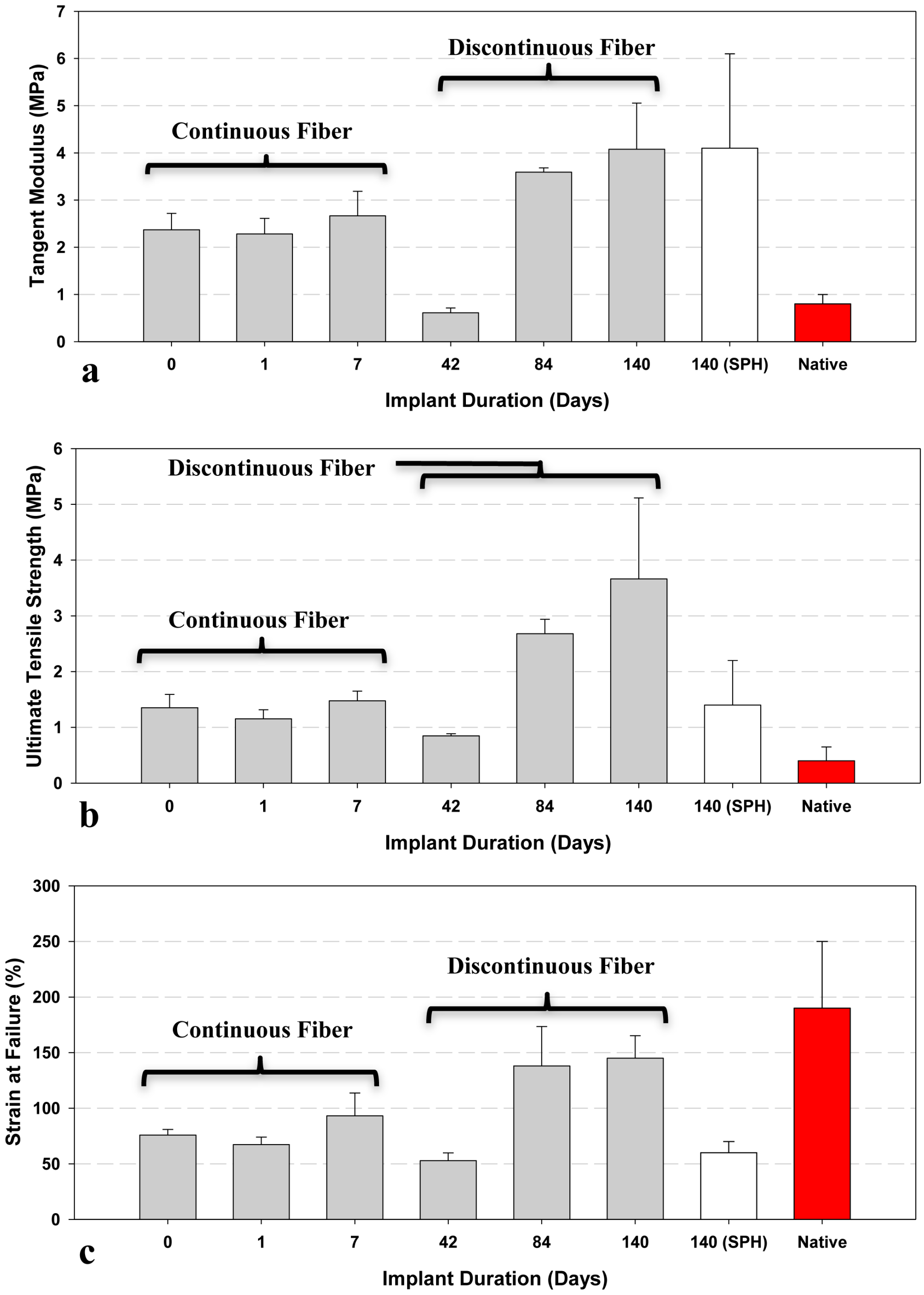

Figure 5.4. Mean uniaxial failure test results for long timepoint TECs. Shown is tangent modulus (a), strain at failure (b), and ultimate tensile strength (c) for short and long timepoint TECs of implant durations of 0 day (N=4), 1 day (N=11), 1 day (N=9), 42 days (N=6), 84 days (N=6), and 140 days (N=6). Native and additional 140 day timepoint data from Hoerstrup et al. [31].

5.3.3 Histology and structural analysis

Scaffold volume fraction was computed from transmural H&E stained sections from four 0 day implants, five 1 day implants, five 7 day implants, three 42 day implants, five 84 day implants, and five 140 day implants. Figure 5.5 shows mean +/- SEM scaffold volume fraction for each experimental timepoint. A sharp decrease can be seen between the virgin scaffold state (0.0702 +/ 0.0102) and the 0 day (0.0460 +/- 0.00404) and 1 day (0.0397 +/- 0.00639) implants. A second sharp decrease can be observed between the 0/1 day implants and 7 day implants (0.0298 +/- 0.00461). Overall, the long implant timepoint specimens showed a change in volume fraction from 0.015 +/- 0.0017 to 0.012 +/- 0.0008 to 0.0033 +/- 0.0003 with implant time. A double exponential was fit to the complete data as:

$$\phi_f = a_1\left(e^{a_2 t} + e^{a_3 t}\right), \tag{5.3}$$

with t as time (days), allowing a means to predict remaining scaffold volume fraction at additional implant timepoints (constant values in Table 5.3). The fit has an r^2 of 0.9988.

Table 5.3. Constant values for data fit of scaffold and collagen volume fraction versus time.

Volume Fraction	**Model Constants**		**r^2**
Scaffold	**a_1**	0.022410	0.9988
	a_2	-0.143600	
	a_3	-0.009797	
Collagen	**b_1**	0.832000	0.8794
	b_2	-0.048900	

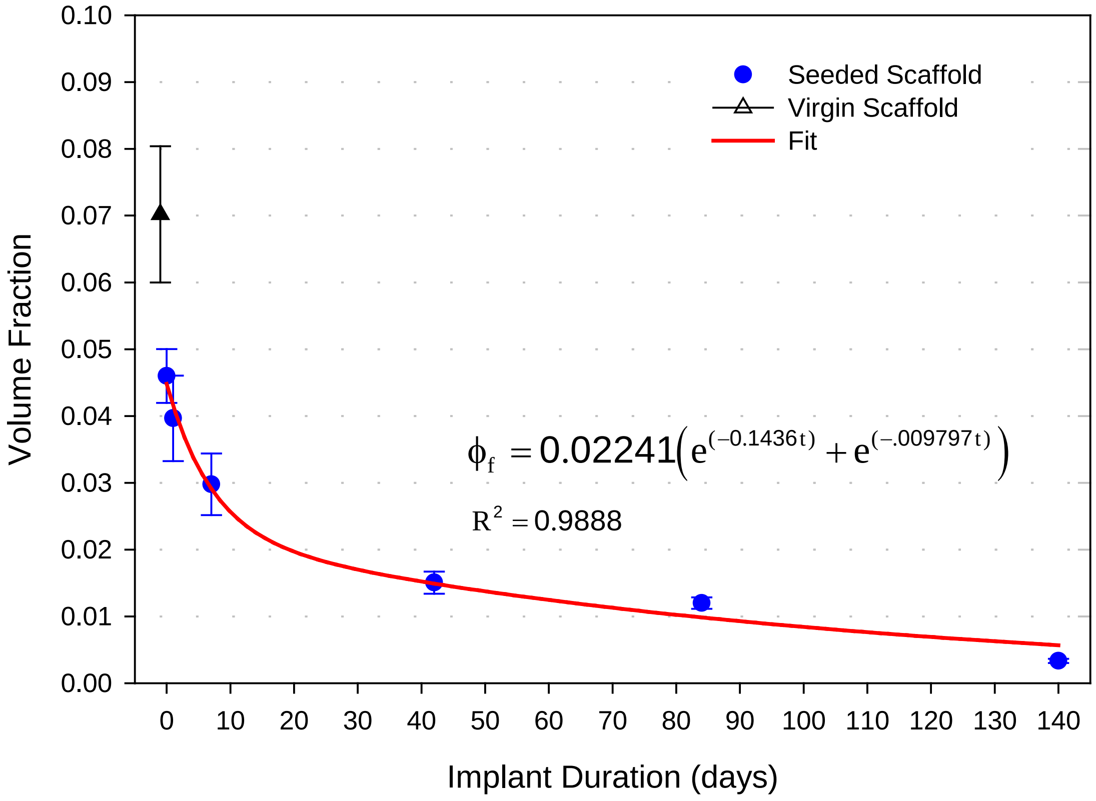

Figure 5.5. Mean +/- SEM scaffold volume fraction vs. implant duration.

In Figure 5.6, representative transmural H&E histology images are shown for all three short implant duration groups with significant scaffold present. Representative transmural images from the three later timepoints are shown in Figure 5.7 with much less scaffold present. In all images, the luminal side of the conduit is shown. Scaffold remnants are distinguishable, and void spaces are present between scaffold remnants and tissue, though much less void space is present in the later timepoints.

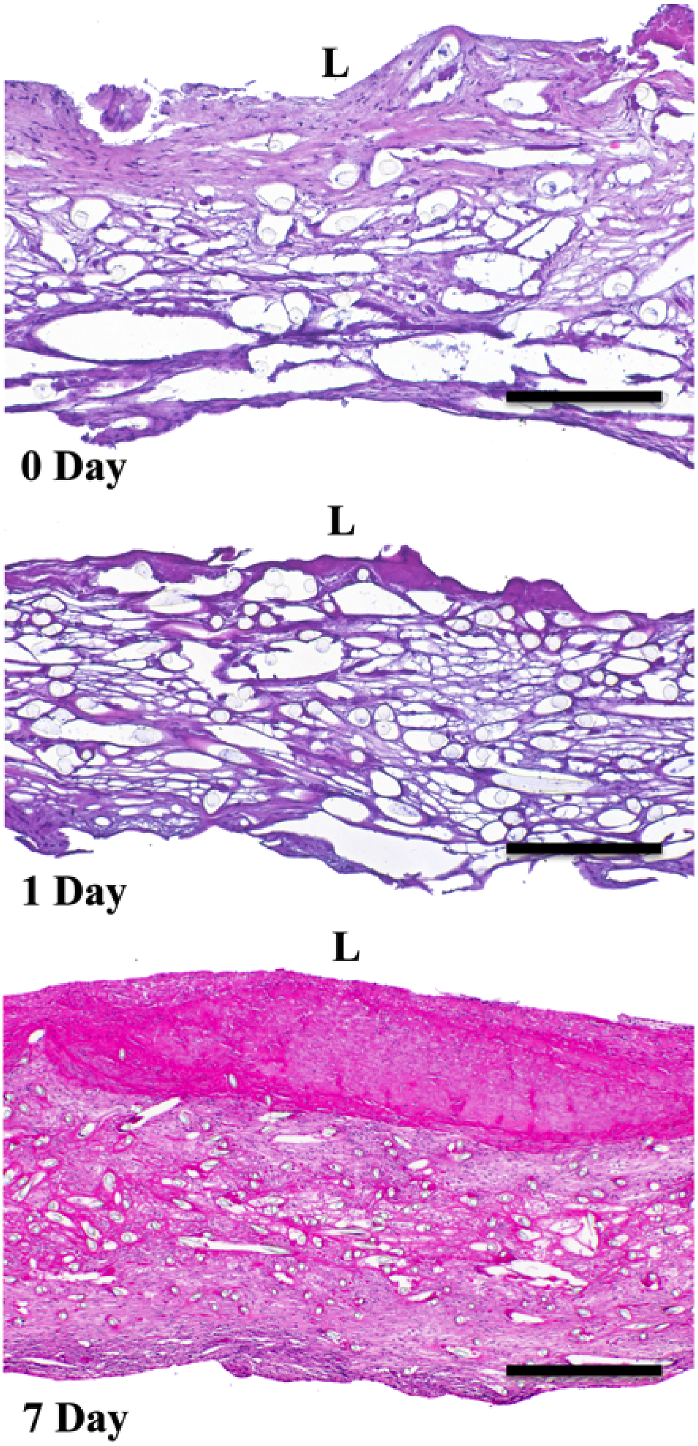

Figure 5.6. Representative transmural H&E histology for short timepoint TECs. Black scale bar represents 300 μm; L denotes luminal side.

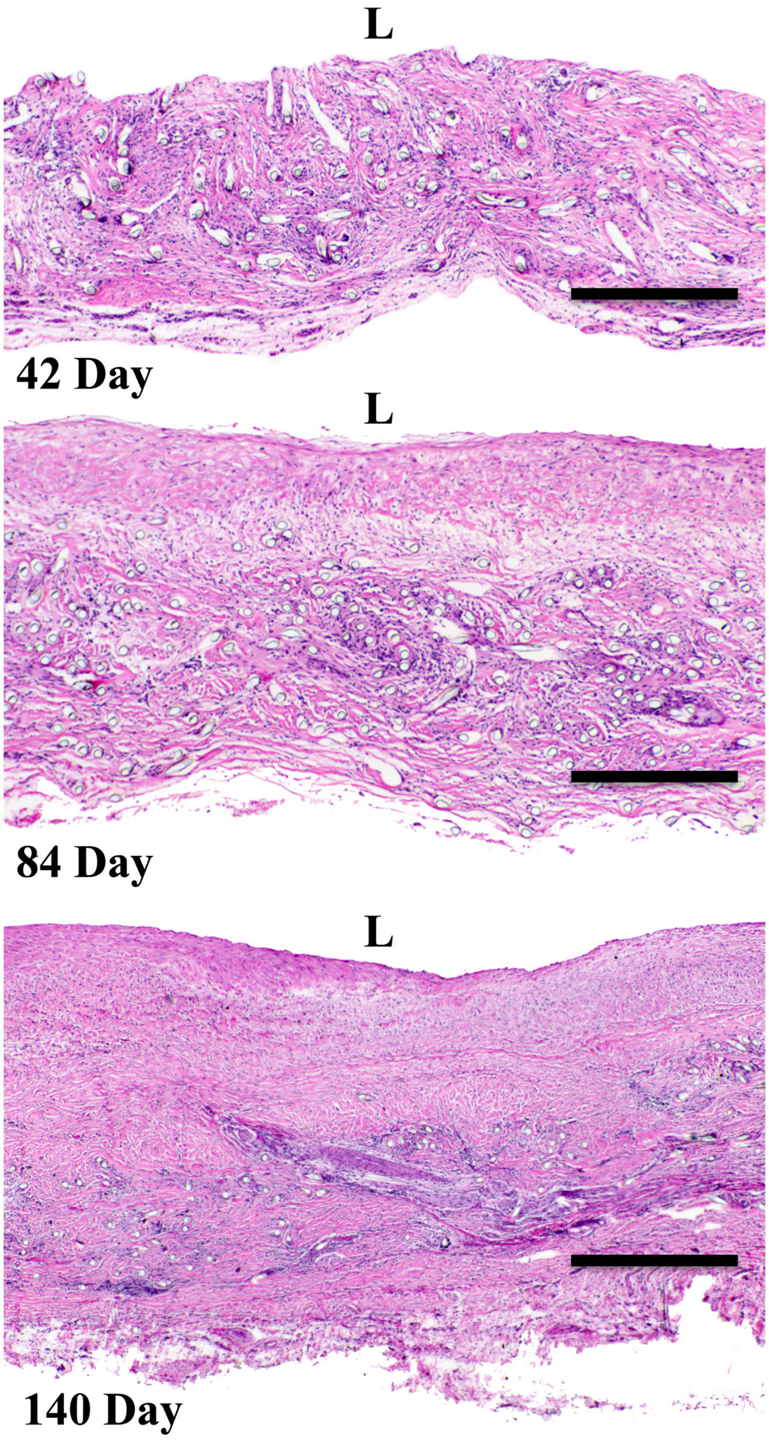

Figure 5.7. Representative transmural H&E histology for long timepoint TECs. Black scale bar represents 300 µm; L denotes luminal side.

In Figure 5.8, representative raw SALS scattered light intensity distribution data is shown for each of the three long implant timepoints groups. As the intensity was symmetrical over the full 360 degrees, only a single peak is shown for a 180 degree range. Generally, data was exceptionally smooth and showed defined single peaks for each 0-180 degree range. Figure 5.9 shows representative en face SALS scans with vector directions and NOI values overlayed. Note that hues towards red and pink indicate more alignment. H&E and picrosirius red histology images are also shown, taken from within the middle region of the specimens. Table 5.4 shows NOI values for each of three specimen depths for two specimens in the three long timepoint groups. Although some variation can be seen between layers in a group, they were not statistically significant from one another and the middle layer was taken as representative for the other specimens.

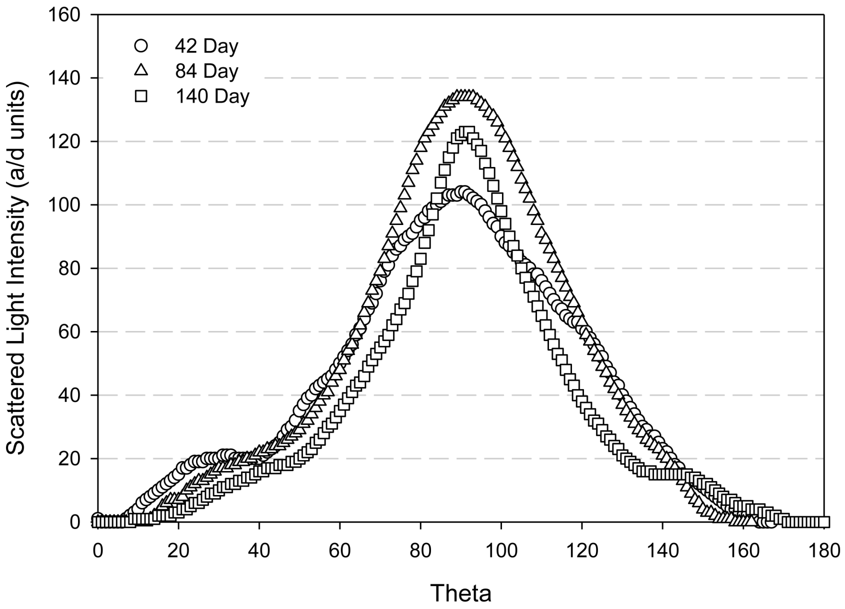

Figure 5.8. Representative scattered light intensity data from SALS for the 42, 84, and 140 day implant groups.

Table 5.4. NOI values from different specimen depths for long timepoint TECs.

Implant Time	Specimen ID	Layer	MEAN NOI (%)	ST. DEV. NOI (%)
42 Days	448_C3	Luminal	52.39	6.77
42 Days	448_C3	Middle	46.53	4.68
42 Days	448_C3	Outer Wall	51.40	5.38
42 Days	483_C2	Luminal	53.22	5.81
42 Days	483_C2	Middle	53.31	8.26
42 Days	483_C2	Outer Wall	51.70	7.16
84 Days	376_C1	Luminal	46.38	7.64
84 Days	376_C1	Middle	46.32	9.85
84 Days	376_C1	Outer Wall	46.49	6.98
84 Days	418_C3	Luminal	45.47	8.25
84 Days	418_C3	Middle	48.88	7.42
84 Days	418_C3	Outer Wall	49.29	7.02
140 Days	347_C1	Luminal	47.22	6.85
140 Days	347_C1	Middle	46.01	8.07
140 Days	347_C1	Outer Wall	47.36	6.52
140 Days	361_C1	Luminal	58.62	5.45
140 Days	361_C1	Middle	57.92	5.20
140 Days	361_C1	Outer Wall	50.53	5.19

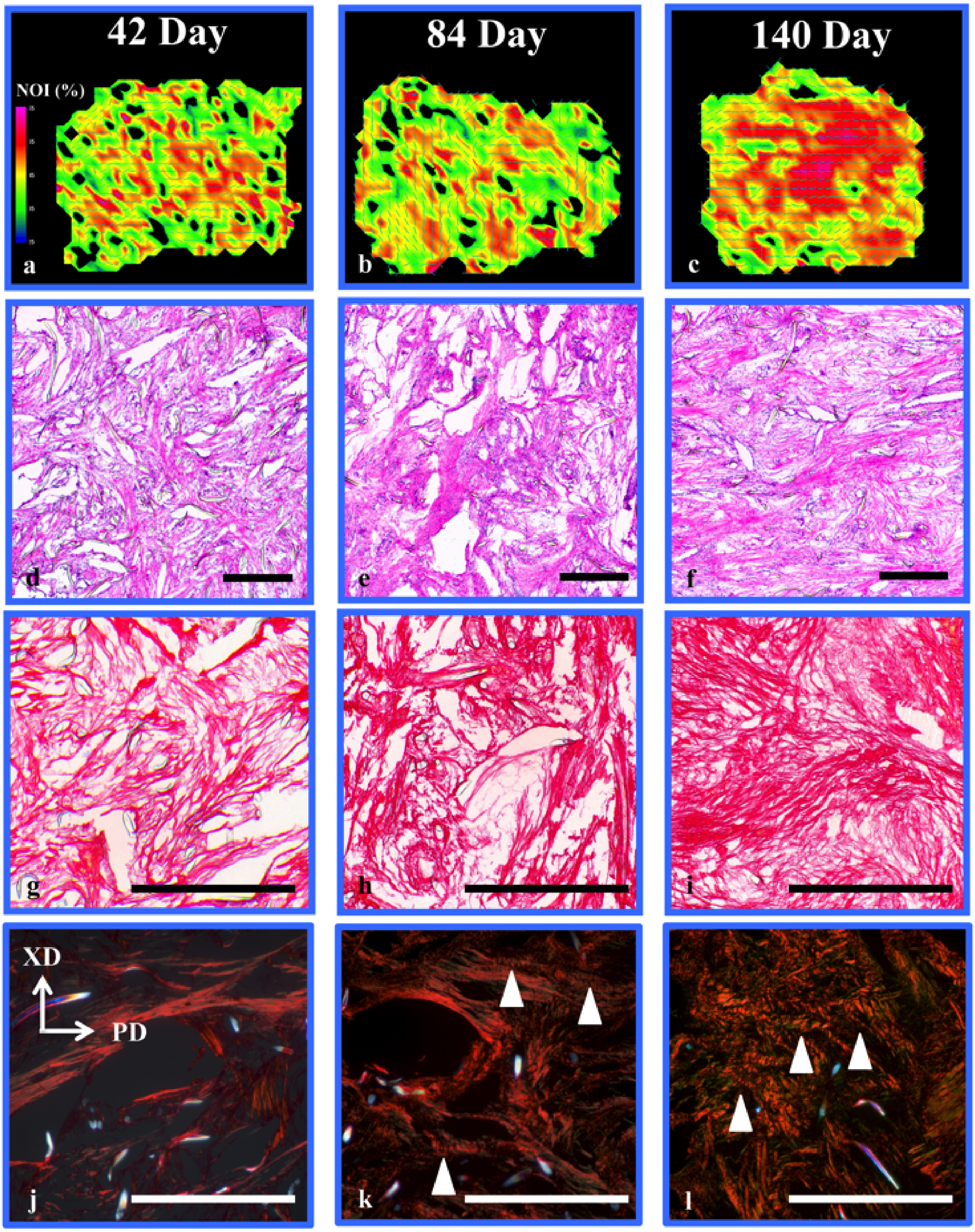

Figure 5.9. Representative en face SALS scans, H&E histology, picrosirius red histology, and picrosirius red histology under polarized light for long timepoint TECs. Vertical groupings are at the same timepoint. (a-c) SALS scans, (d-f) H&E histology, (g-i) picrosirius red histology, and (j-l) polarized light picrosirius red histology. Bars represent 600 microns; white triangles indicate crimped collagen.

Though indications of some improved alignment with time can be observed in regions of specimens, mean NOI values for the three groups, as shown in Figure 5.10, show little difference (no statically significance difference) from one another. Virgin scaffold NOI is also shown, with no difference between the other groups. In the histology images, decreased scaffold can be observed in both H&E and picrosirius red stained sections as implant time increases. Qualitatively, tissue appears to become denser as implant time increased. Picrosirius red stain shows aligned collagen fibers with some crimping in fibers, but this has not been quantified in this study.

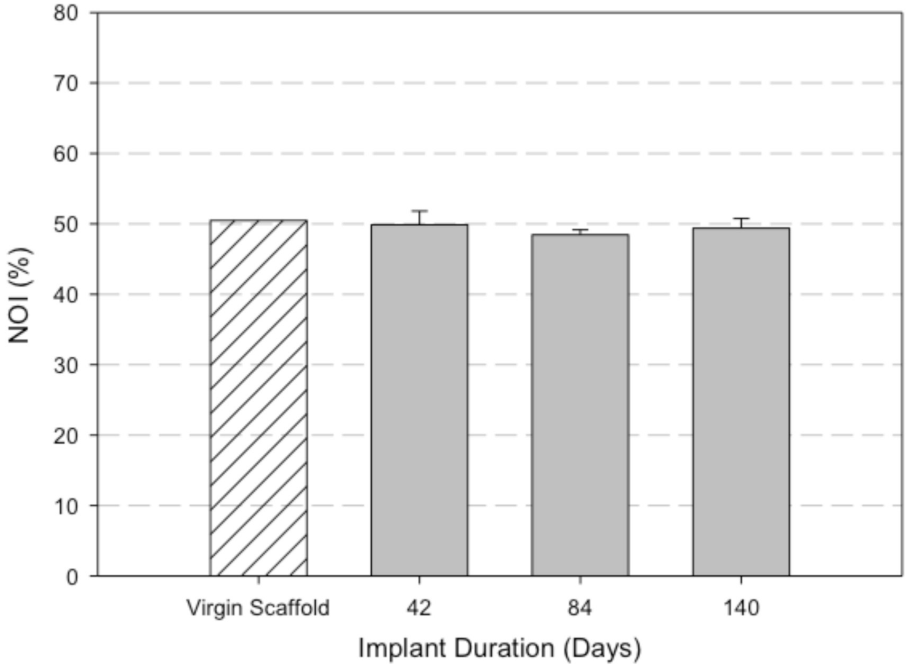

Figure 5.10. NOI vs. implant duration for long timepoint TECs. Virgin scaffold data is also presented.

For the long implant duration groups (42, 84, and 140 days), approximate collagen volume fractions were computed using the picrosirius red en face histology images. Mean +/- SEM values for each group (n=2 per group) are shown in Figure 5.11. Note that collagen volume fraction has been averaged at three depth locations (top surface, middle, bottom surface) for each specimen, yielding n=6 measured regions per implant group. Collagen volume fraction shows little variation, changing from 0.7304 +/- 0.0175 (42 day) to 0.7957 +/- 0.0307 (84 day), to 0.8487 +/- 0.0164 (140 day). An exponential rise to maximum function has been fit to the data as

$$\phi_c = b_1\left(1-e^{b_2 t}\right), \tag{5.4}$$

with t as time (days), with a good quality of fit (r^2 of 0.8794) and suggesting an approach to maximum collagen volume fraction (constant values in Table 5.3). Additionally, representative polarized light microscopy images of 42, 84, and 140 implant duration specimens are shown in Figure 5.9. Overall, limited banding and striations, characteristic of collagen crimp, can not be observed in the 42 day implant specimen, while crimp can be seen (white arrows) in both the 84 and 140 day specimens.

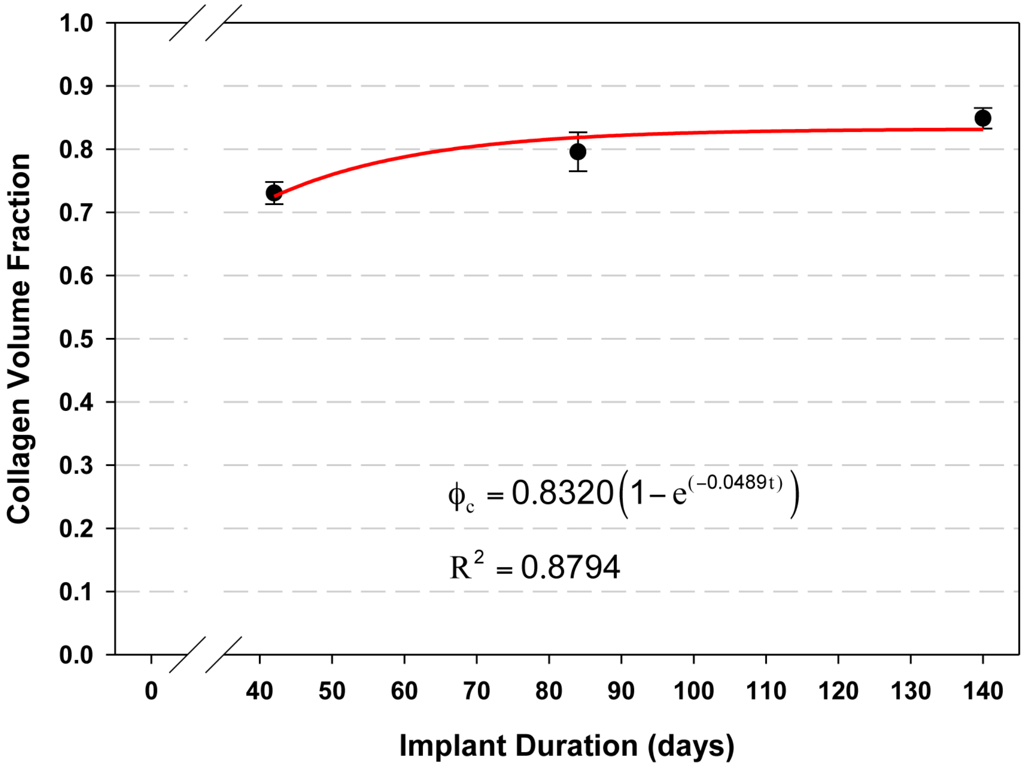

Figure 5.11. Mean +/- SEM collagen volume fraction for 42, 84, and 140 day implant duration TECs.

Thickness values for specimens undergoing biaxial testing have been averaged and plotted in Figure 5.12 versus implant duration. At the early timepoint implants, little variation in thickness is seen with values of 0.694 mm +/- 0.030 mm (0 day) and 0.700 mm +/- 0.028 mm (1 day), though a small rise to 0.970 mm +/- 0.056 mm is seen in the 7 day implant duration group. By the 42 day implant duration group, however, a large jump to 1.507 mm +/- 0.170 mm is observed, followed by a decrease to 0.980 mm +/- 0.179 mm in the 84 day implant group and 1.046 mm +/- 0.103 in the 140 day implant group. Only the 42 day group showed statistically significant differences from any other group over the implant duration.

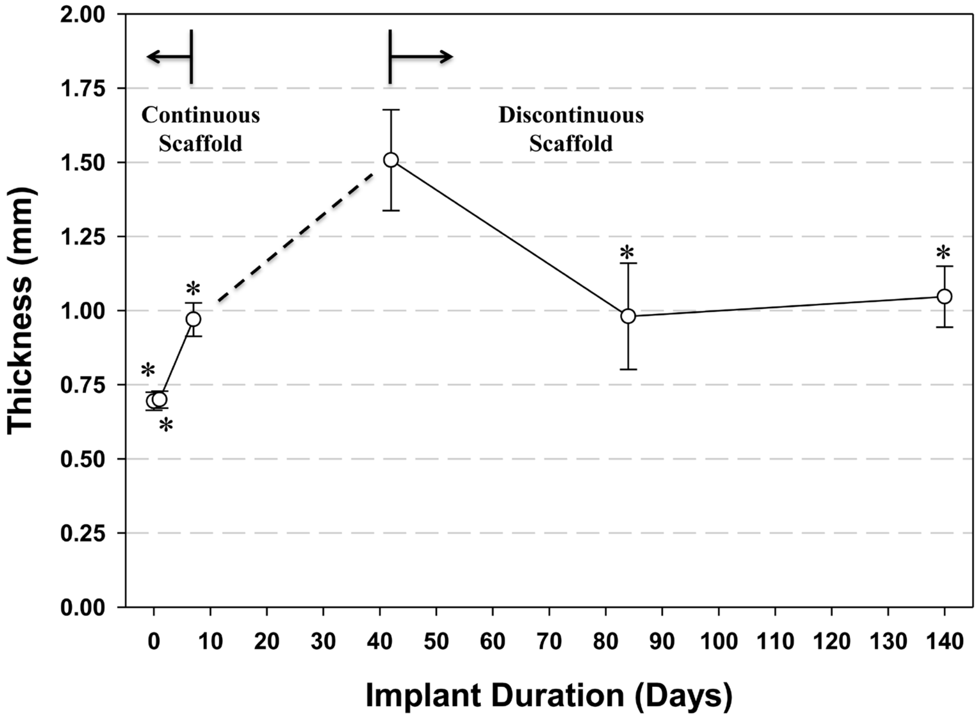

Figure 5.12. Mean +/- SEM TEC specimen thickness vs. implant duration. Asterisk denotes statistically significant difference from the 42 day implant duration group, $p < 0.05$.

5.3.4 Continuous scaffold fiber constitutive model results

With the constitutive model form and reinforcing relationship between effective scaffold stiffness and matrix shear modulus established in chapter 4, the tissue phase shear modulus in the continuous scaffold fiber TECs was estimated from the 0, 1, and 7 day data sets. A total of three loading protocols were fit simultaneously for each data set, and parameters of shear modulus and scaffold orientation mean were estimated. Table 5.5 shows parameter values for all evaluated data sets, as well as quality of fit assessments. Highlighted rows indicate those specimens not included in averaging due to unreasonably poor model fits ($r^2 < 0.55$).

Table 5.5. Continuous scaffold fiber model fit parameters for 0, 1, and 7 day implant duration groups.

Implant Length	ID	μ (kPa)	μ (corr.) (kPa)	ϕ_1 (deg)	k_{eff} (kPa)	R^2_{11}	R^2_{22}
0 Day	434C_C1	26.60	14.55	9.00	9659	0.7180	0.8168
0 Day	483C_C1	4.49	1.76	8.55	2996	0.8671	0.7586
0 Day	483C_C2	6.96	2.74	8.55	3344	0.7884	0.8880
0 Day	483C_C3	14.47	6.28	16.50	4692	0.3749	0.8268
	MEAN	**12.68**	**6.35**	**8.70**	**3677**	---	---
	SEM	**7.00**	**4.11**	**0.15**	**517**	---	---
1 Day	241_C1	1.57	0.58	8.55	2284	0.9165	0.9302
1 Day	242_C1	0.15	0.05	0.21	2156	0.7537	0.8890
1 Day	242_C3	8.11	3.23	7.58	3041	0.8639	0.9233
1 Day	413_C1	11.27	4.67	8.32	3702	0.7888	0.8037
1 Day	413_C2	-4.80	---	0.46	1819	-1.8100	-1.7090
1 Day	432_C1	0.92	0.34	10.01	2224	0.7862	0.8797
1 Day	432_C3	8.52	3.41	-12.48	3097	0.8828	0.7325
1 Day	454_C2	14.96	6.53	8.70	4257	0.9660	0.9346
1 Day	454_C3	40.29	37.37	6.89	10910	0.5218	0.8715
1 Day	476_C1	21.07	10.20	8.68	6089	0.9275	0.9017
1 Day	476_C3	21.14	10.25	9.75	6088	0.9141	0.8313
	MEAN	**9.75**	**4.36**	**5.48**	**3660**	---	---
	SEM	**2.71**	**1.32**	**2.45**	**515**	---	---
7 Day	362_C1	11.92	4.99	-8.55	2225	0.8442	0.7762
7 Day	362_C2	19.06	8.89	7.34	3711	0.9126	0.7793
7 Day	362_C3	11.76	4.91	8.55	1634	0.8048	0.8990
7 Day	411_C1	10.48	4.30	-8.06	1629	0.8060	0.8669
7 Day	411_C2	59.96	55.65	-8.55	14348	0.5778	0.9421
7 Day	411_C3	26.65	14.60	14.88	5055	0.9219	0.9425
7 Day	449_C2	10.67	4.39	-0.41	1679	0.9042	0.7834
7 Day	449_C3	12.64	5.34	8.99	2294	0.8324	0.9205
	MEAN	**14.74**	**6.77**	**1.77**	**4072**	---	---
	SEM	**2.27**	**1.43**	**3.31**	**1529**	---	---

Figure 5.13 shows mean and standard error of the mean for tissue shear modulus in each of the three groups. Note that these values have been adjusted (listed as corr. in the table) from the fit shear modulus value based on the matrix-scaffold shear interaction term in chapter 4. Mean shear modulus values of 6.35 kPa +/- 4.11 kPa, 4.36 kPa +/- 1.32 kPa, and 6.77 kPa +/- 1.43 kPa were computed for the 0, 1, and 7 day TEC specimens, respectively. There was no statistically

significant difference between the groups. The mean values were used to estimate tissue stress using average stretch values from the 42 day specimen group (Figure 5.14). The maximum stress value changed little between the groups, with values of 1.482 kPa, 1.019 kPa, and 1.582 kPa in the preferred direction and of 1.746 kPa, 1.201 kPa, and 1.863 kPa in the cross preferred direction for the 0, 1, and 7 day groups, respectively. In Figure 5.15, biaxial stress responses are shown for representative 7 and 42 day implant groups to show the substantial difference in peak stress.

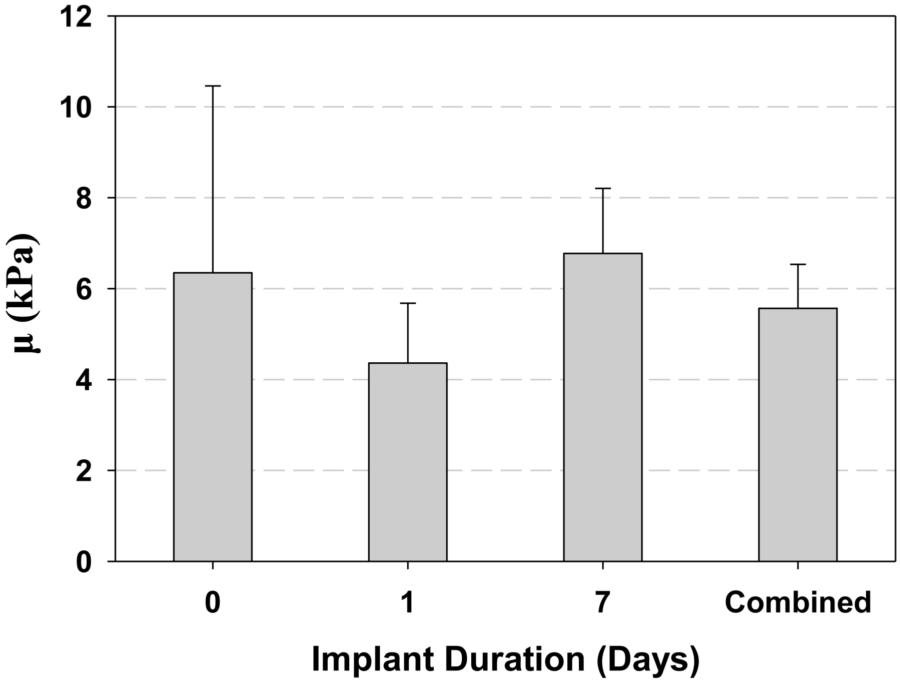

Figure 5.13. Tissue shear modulus (mean +/- SEM) for short implant duration TECs. Values are not statistically different from one another.

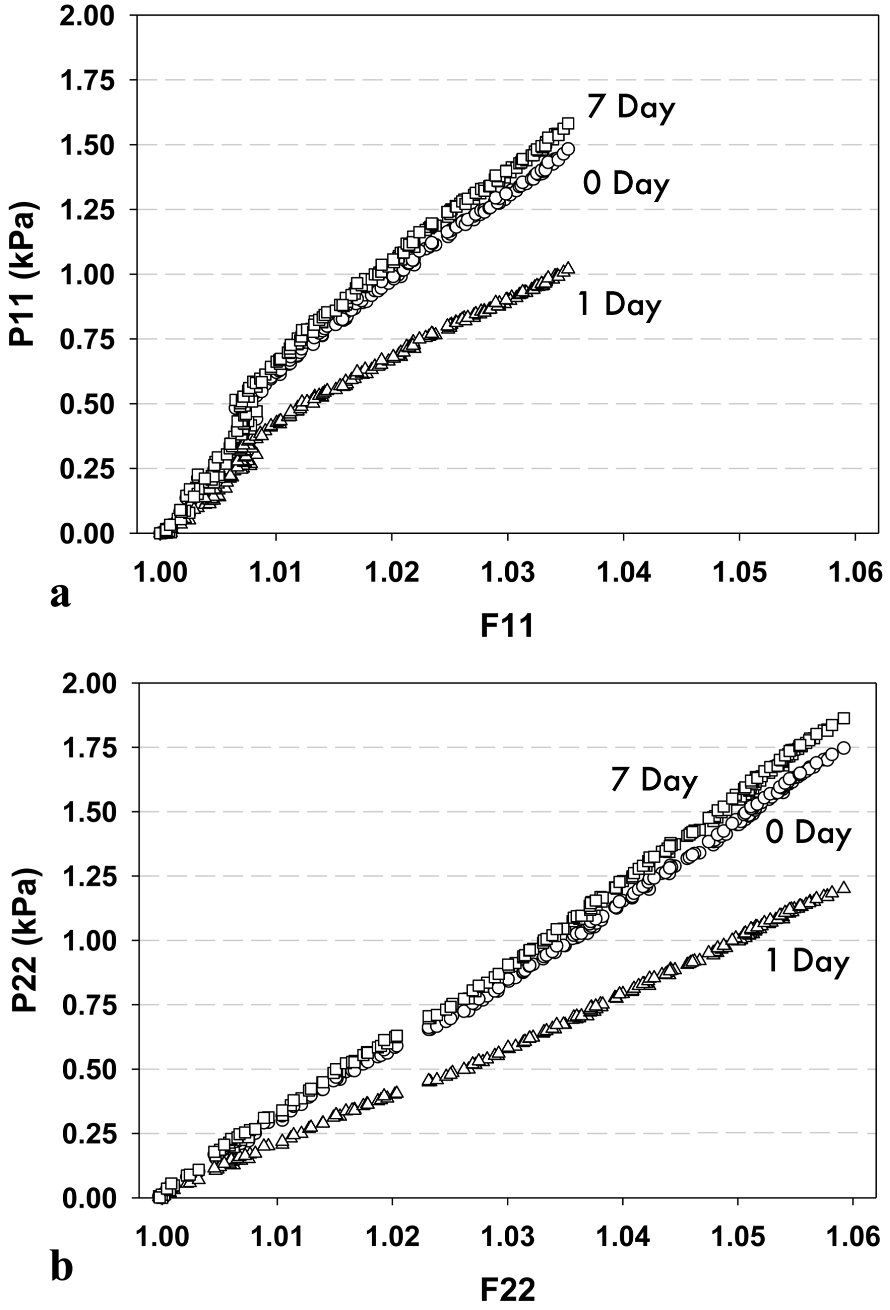

Figure 5.14. Biaxial stress response of 0- 7 day TECs using 42 day TEC deformation data. (a) Preferred and (b) cross-preferred directions show some difference in stress due to differences in stretch. Circles, triangles, and squares represent 0, 1, and 7 day groups respectively.

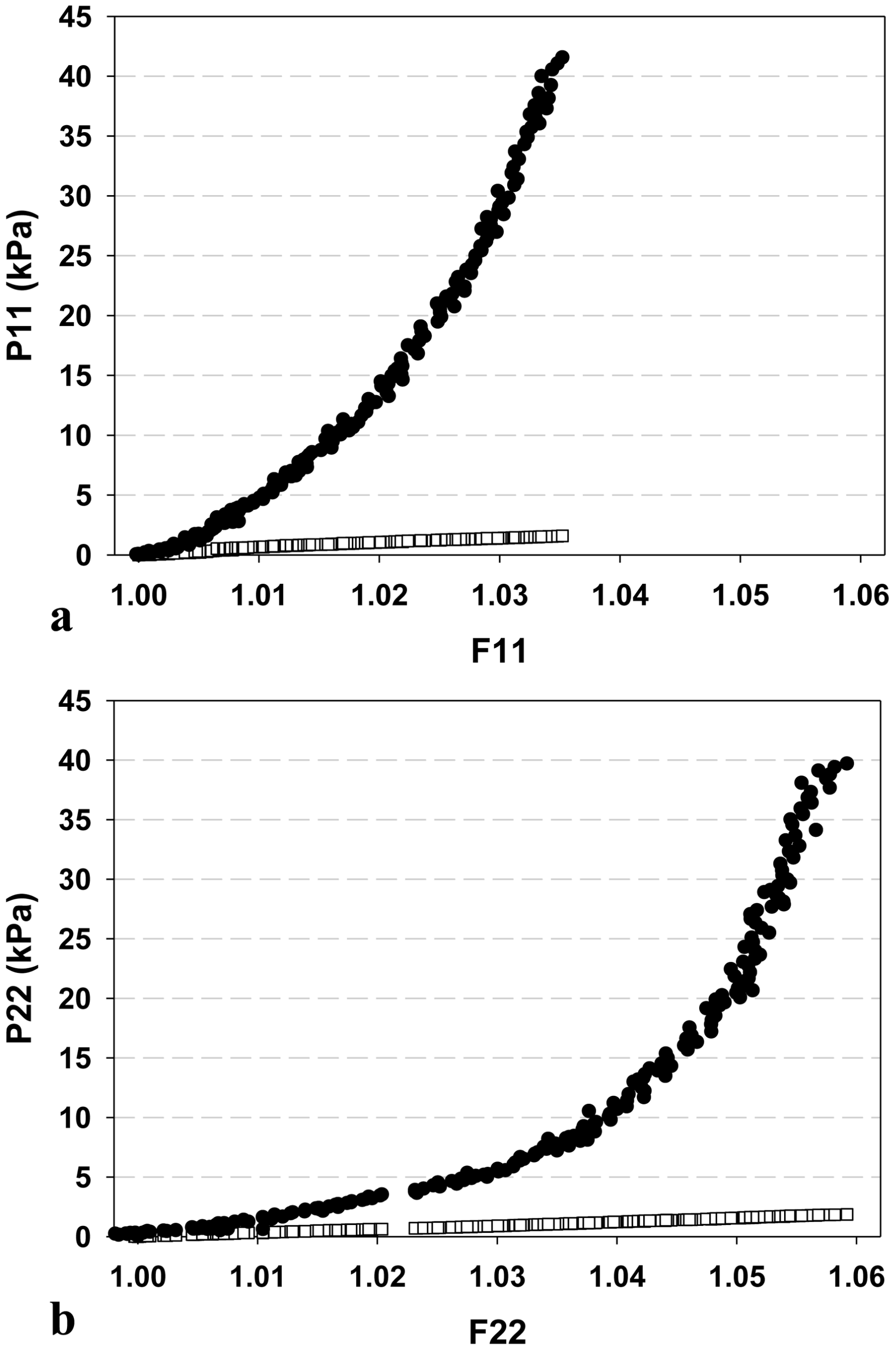

Figure 5.15. Biaxial stress response of 7 and 42 day TECs. (a) Preferred and (b) cross-preferred directions show little difference in 7 day tissue stress when scaled to realized composite stress values (50 kPa).

5.3.5 Long implant duration constitutive model results

Because a reinforcing effect of the fragmented scaffold fiber phase was not observed (section 4.3.4), the fiber strain energy contribution was assumed to be zero. This confirmed the theoretically based assumptions and simplified the full constitutive model form. Volume fraction was still accounted for, however, though the contribution from the fiber phase was assumed zero (and the volume fraction of the tissue was adjusted accordingly). Table 5.6 and Table 5.7 show parameters and quality of fit (R^2) values for all test groups (42 day, 84 day, and 140 day post implant). Note tables were split based on recruitment distribution parameters (Table 5.6) and orientation distribution parameters (Table 5.7) for simplicity. Mean parameters were computed by averaging the functions' responses (i.e. the ensemble stress or the probability distribution) for each parameter set and then fitting the response function to the averaged values. Since the parameters relate to the function in a non-linear manner, significant errors could be introduced by simply performing a mathematical mean to the parameter values themselves. Figure 5.16 shows a representative plot of fitted data in both directions. In most tested specimens, R^2 values over 0.85 for both axes were obtained. Initial values for the orientation distribution parameters were provided based on data from the SALS experiments. Subsequent fitting stage orientation standard deviation values were bounded by 1.5 the measured standard deviation to prevent unguided model minimization. The distribution means were permitted to move within larger bounds because of potential differences between orientation in the biaxial testing device and SALS device.

Table 5.6. Best-fit model recruitment model parameters for all long timepoint TECs. For mean and SEM calculations, all specimens were used except 376_C1.

Implant Length	ID	P^{ens} slope (kPa)	K (kPa)	μ (scaled)	σ (scaled)	μ	σ	LB λ	UB λ	UB λ (est)
42 Days	434_C2	7187	7744	0.7055	0.2223	1.0462	0.0149	1.0000	1.0649	1.0680
42 Days	448_C3	8388	8645	0.5496	0.2200	1.0170	0.0065	1.0008	1.0300	1.0430
42 Days	483_C2	8042	8482	0.5258	0.2730	1.0165	0.0086	1.0000	1.0312	1.0840
	MEAN	**7872**	**8290**	**0.5936**	**0.2384**	**1.0266**	**0.0100**	**1.0003**	**1.0420**	**1.0650**
	SEM	**276**	**285**	**0.0564**	**0.0173**	**0.0098**	**0.0025**	**0.0003**	**0.0143**	**0.0079**
	AVG FIT	**---**	**---**	***0.5930***	***0.2520***	***1.0250***	***0.0105***	**---**	**---**	**---**
84 days	376_C1	12930	15080	0.8402	0.0993	1.0177	0.0021	1.0000	1.0210	1.0210
84 days	376_C3	13098	15120	0.8300	0.1300	1.0283	0.0045	1.0000	1.0340	1.0340
84 days	418_C1	17660	18000	0.7602	0.1007	1.0069	0.0019	1.0000	1.0190	1.0280
84 days	418_C2	17120	18008	0.6897	0.2198	1.0517	0.0167	1.0007	1.0739	1.1090
84 days	418_C3	20070	21134	0.7466	0.1609	1.0400	0.0088	1.0000	1.0532	1.0640
	MEAN	**16174**	**17468**	**0.7733**	**0.1421**	**1.0289**	**0.0068**	**1.0001**	**1.0402**	**1.0512**
	SEM	**1384**	**1114**	**0.0279**	**0.0225**	**0.0079**	**0.0028**	**0.0001**	**0.0114**	**0.0183**
	AVG FIT	**---**	**---**	***0.7800***	***0.1450***	***1.0314***	***0.0058***	**---**	**---**	**---**
140 Days	253_C1	33430	36000	0.8302	0.1100	1.0501	0.0068	1.0000	1.0600	1.0600
140 Days	347_C1	34010	35000	0.8039	0.1300	1.0248	0.0041	1.0000	1.0308	1.0370
140 Days	347_C2	1865	2000	0.8003	0.1900	1.0588	0.0120	1.0100	1.0707	1.0720
140 Days	347_C3	33210	38000	0.8204	0.1200	1.0404	0.0060	1.0000	1.0490	1.0490
140 Days	361_C1	23980	30000	0.8550	0.1486	1.0550	0.0098	1.0000	1.0640	1.0640
140 Days	361_C2	24640	29000	0.8603	0.1000	1.0241	0.0028	1.0000	1.0280	1.0280
	MEAN	**29854**	**33600**	**0.8339**	**0.1217**	**1.0389**	**0.0059**	**1.0000**	**1.0464**	**1.0517**
	SEM	**2269**	**7461**	**0.0106**	**0.0084**	**0.0063**	**0.0012**	**0.0022**	**0.0041**	**0.0056**
	AVG FIT	**---**	**---**	***0.8310***	***0.1250***	***1.0385***	***0.0058***	**---**	**---**	**---**

Table 5.7. Best-fit model fiber orientation parameters for all long timepoint TECs. For mean and SEM calculations, all specimens were used except 376_C1.

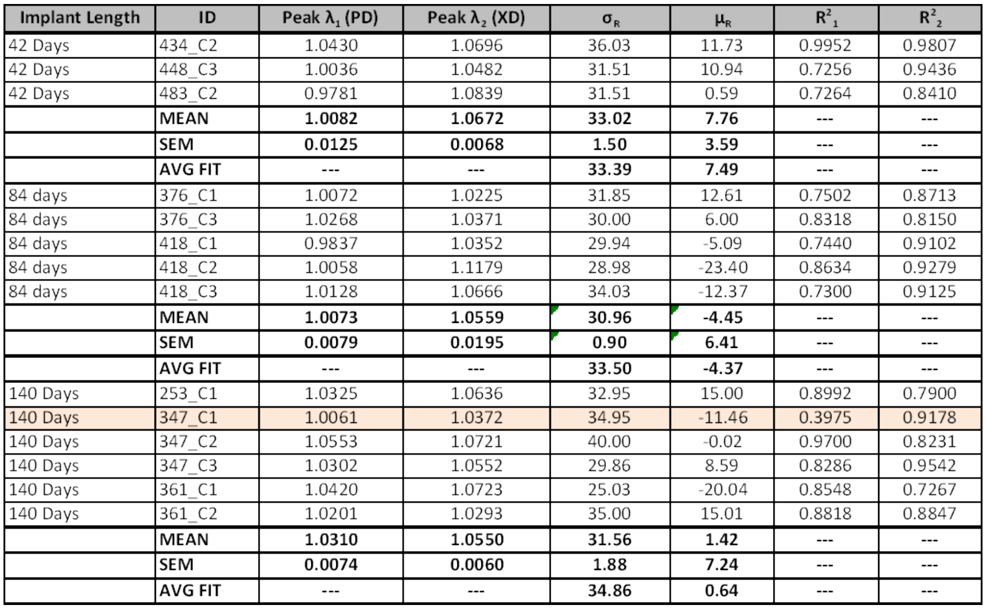

Implant Length	ID	Peak λ_1 (PD)	Peak λ_2 (XD)	σ_R	μ_R	R^2_1	R^2_2
42 Days	434_C2	1.0430	1.0696	36.03	11.73	0.9952	0.9807
42 Days	448_C3	1.0036	1.0482	31.51	10.94	0.7256	0.9436
42 Days	483_C2	0.9781	1.0839	31.51	0.59	0.7264	0.8410
	MEAN	**1.0082**	**1.0672**	**33.02**	**7.76**	**---**	**---**
	SEM	**0.0125**	**0.0068**	**1.50**	**3.59**	**---**	**---**
	AVG FIT	**---**	**---**	**33.39**	**7.49**	**---**	**---**
84 days	376_C1	1.0072	1.0225	31.85	12.61	0.7502	0.8713
84 days	376_C3	1.0268	1.0371	30.00	6.00	0.8318	0.8150
84 days	418_C1	0.9837	1.0352	29.94	-5.09	0.7440	0.9102
84 days	418_C2	1.0058	1.1179	28.98	-23.40	0.8634	0.9279
84 days	418_C3	1.0128	1.0666	34.03	-12.37	0.7300	0.9125
	MEAN	**1.0073**	**1.0559**	**30.96**	**-4.45**	**---**	**---**
	SEM	**0.0079**	**0.0195**	**0.90**	**6.41**	**---**	**---**
	AVG FIT	**---**	**---**	**33.50**	**-4.37**	**---**	**---**
140 Days	253_C1	1.0325	1.0636	32.95	15.00	0.8992	0.7900
140 Days	347_C1	1.0061	1.0372	34.95	-11.46	0.3975	0.9178
140 Days	347_C2	1.0553	1.0721	40.00	-0.02	0.9700	0.8231
140 Days	347_C3	1.0302	1.0552	29.86	8.59	0.8286	0.9542
140 Days	361_C1	1.0420	1.0723	25.03	-20.04	0.8548	0.7267
140 Days	361_C2	1.0201	1.0293	35.00	15.01	0.8818	0.8847
	MEAN	**1.0310**	**1.0550**	**31.56**	**1.42**	**---**	**---**
	SEM	**0.0074**	**0.0060**	**1.88**	**7.24**	**---**	**---**
	AVG FIT	**---**	**---**	**34.86**	**0.64**	**---**	**---**

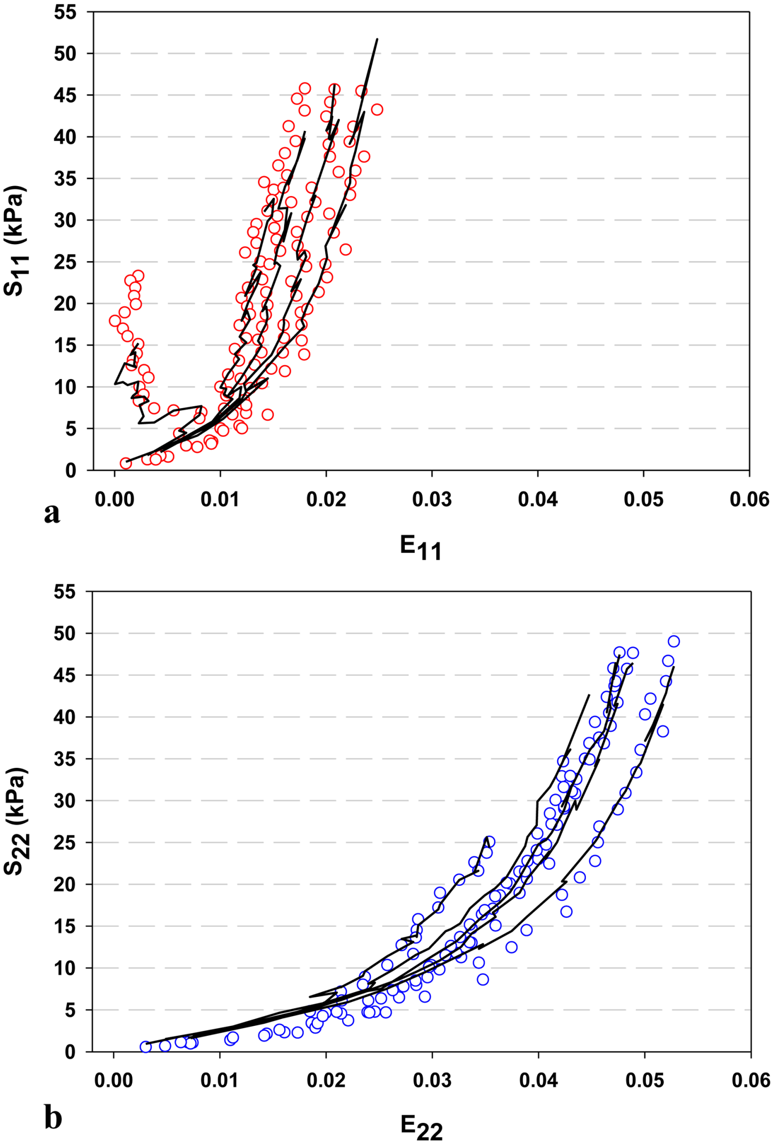

Figure 5.16. Model fit to representative biaxial data for long timepoint TECs. Data is shown for (a) preferred and (b) cross-preferred directions.

The mean +/- SEM collagen ensemble stress vs. stretch for all three long implant duration groups is shown in Figure 5.17. At stretch values of 1.05 and larger, a significant different exists between collagen ensemble stress in the 42 day implant duration group compared to the other two timepoints. No difference exists between the 84 and 140 day implant durations. Ultimately at a stretch of 1.064 (picked as the largest mean peak biaxial stretch observed), collagen ensemble stress values reach 307.3 kPa +/- 54.67 kPa, 588.1 kPa +/- 113.0 kPa, and 816.4 kPa +/- 176.8 kPa for the 42, 84, and 140 day implant duration groups. Mean orientation distribution and recruitment distributions responses are shown in Figure 5.18 for the three long implant duration groups. The orientation distribution was plotted over the full 180^o range, while the ensemble collagen response was graphed over an average ensemble strain range. The orientation distributions did not show significant difference from one another at any orientation angle for the three groups. Orientation distribution standard deviations maintained fairly constant at 33.39 degrees, 33.50 degrees, and 34.86 degrees for the three groups, while distribution mean values changed slightly from 7.49 degrees, -4.37 degrees, and 0.64 degrees for the 42, 84, and 140 day implant duration groups (note that these are fits to the mean parameters, so no SEM values are computed). The mean recruitment distribution for each of the three long implant duration groups is shown in Figure 5.18. It should be noted that the recruitment function is scaled to the lower and upper bound stretch values for each specimen. Initially broad with a mean of 0.5930 and standard deviation of 0.2520 (42 days), the ensemble fiber recruitment shifted towards the upper bound stretch with a mean and standard deviation of 0.7800 and 0.1450 at 84 days and 0.8310 and 0.1250 at 140 days. Compared to the 42 day group, statistically significant differences were observed from 0.1 to 0.5 and 0.8 to 0.9 in the 84 and 140 day implant duration groups.

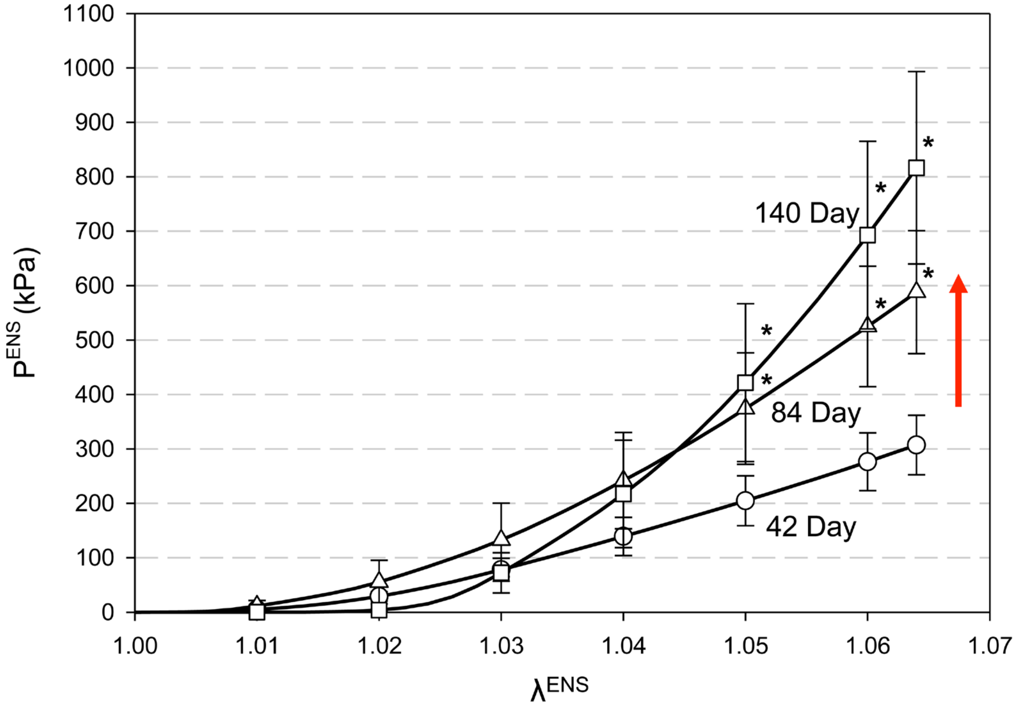

42 Day (n=3), 84 Day (n=5), 140 Day (n=5)   * Indicates statistically significant difference from 42 Day, $p<0.05$

Figure 5.17. Mean +/- SEM ensemble stress response for 42, 84, and 140 day implant duration groups.

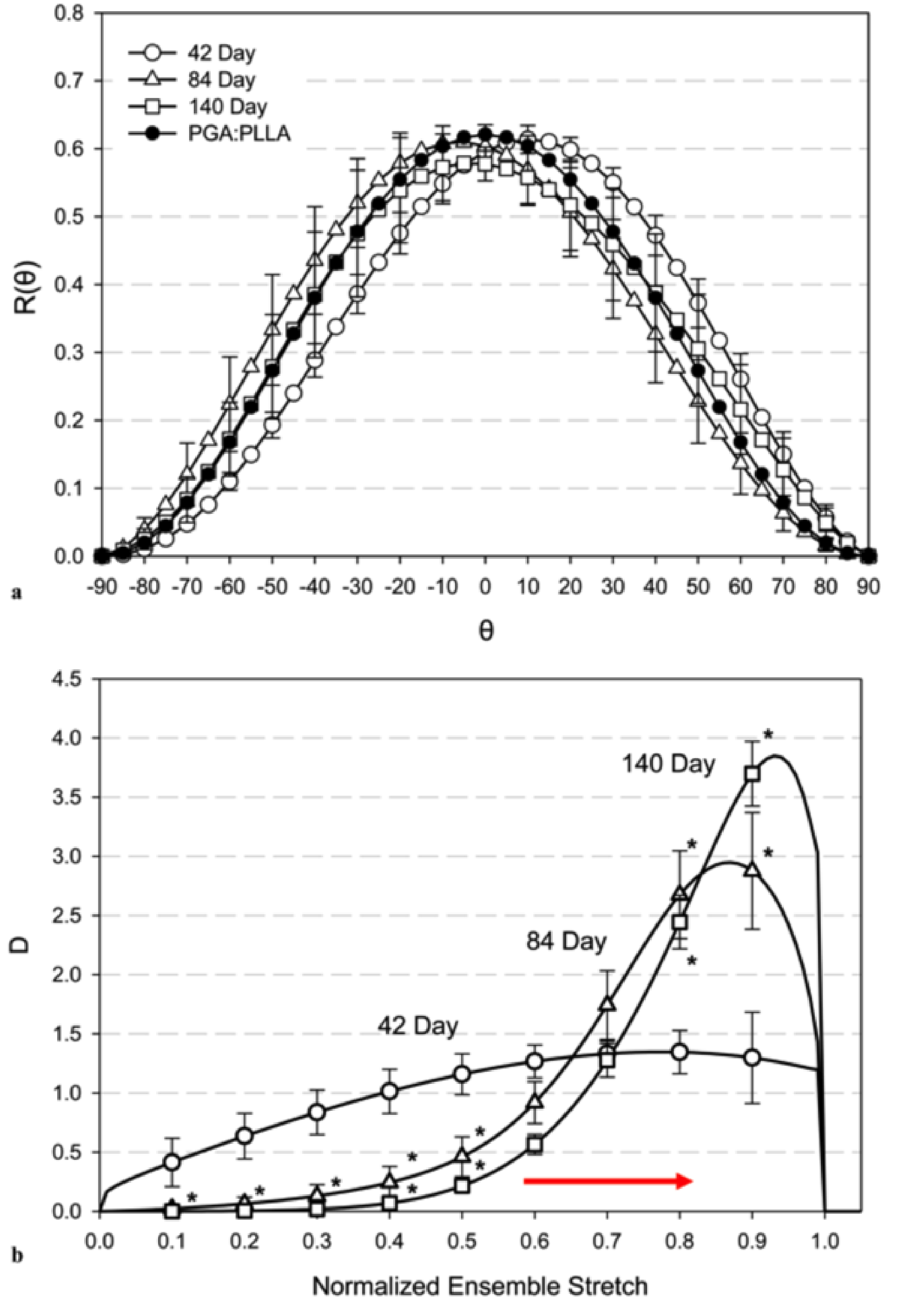

42 Day (n=3), 84 Day (n=5), 140 Day (n=5) * Indicates statistically significant difference from 42 Day, $p<0.05$

Figure 5.18. Mean collagen ensemble orientation and recruitment distributions for long timepoint TECs. (a) Mean collagen ensemble orientation and (b) mean collagen ensemble recruitment long timepoint TECs, shown as mean +/- SEM.

In Figure 5.19, the mean effective collagen fiber stiffness is plotted as a function of implant duration for the 42 day, 84 day, and 140 day groups. It can be seen that the effective collagen stiffness increases from 8,290 kPa +/- 175 kPa to 17,490 kPa +/- 996 kPa and 33,600 kPa +/- 1,560 kPa in the 42, 84, and 140 day implant duration groups; all three are statistically significant from one another. When normalized by collagen volume fraction, a similar trend is evident in collagen fiber stiffness, with values of 11,350 kPa +/- 379 kPa, 21,950 kPa +/- 1,410 kPa, and 39,590 kPa +/- 2,060 kPa in the three groups (not plotted). As in the effective fiber stiffness plot, all collagen fiber stiffness values are statistically significant from one another.

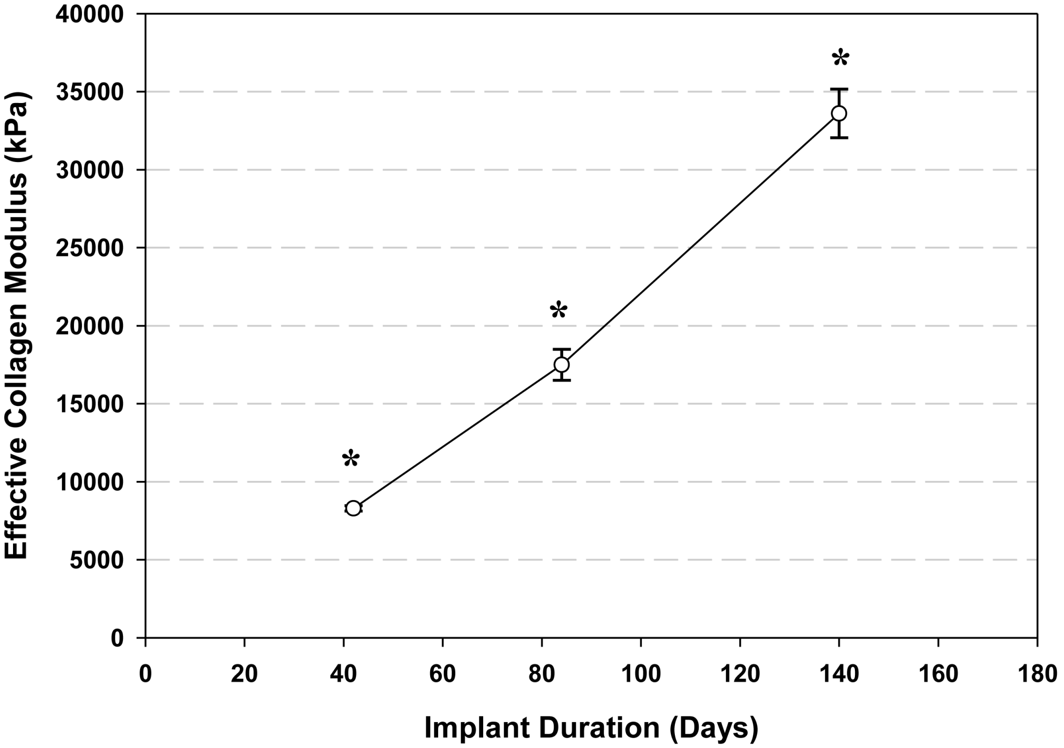

Figure 5.19. Mean collagen ensemble stiffness and collagen fiber stiffness for the 42, 84, and 140 day implant duration groups. Values are plotted as mean +/- SEM and are statistically different from one another (p<0.05).

5.4 DISCUSSION

To our knowledge, this is the first published study to consider the effects of intact and fragmented polymeric scaffold fibers on the mechanical properties of in vivo engineered tissue, making use of detailed 3D structural information on the scaffold phase. Although degradable polymeric scaffolds such as PGA:PLLA nonwoven copolymers have been used extensively for tissue engineering applications [9, 23, 31, 33, 54, 58, 61, 62], almost all studies consider the scaffold fully degraded by after three to four weeks after in vitro culturing and offer no additional insight. In previous work (section 2.3.3), fragmented scaffold was observed in engineered heart valve tissue up to twelve weeks post implant, clearly indicating that scaffold does remain and requires consideration in relation to experimentally determined mechanical properties. Further, this is the first known work to utilize a structural constitutive modeling approach to fully investigate how ECM in TECs remodel post implant.

5.4.1 Mechanical and structural evidence of tissue remodeling in TECs

Both sets of mechanical data reveal interesting insights into the remodeling process of TECs. Uniaxial extension tangent modulus and ultimate tensile strength values both increase with implant time but appear to taper as if remodeling towards a point. In the same manner, strain at failure appears to approach a limit similar to native properties after 140 days. The sharp contrast between early timepoints (0 to 7 days) and longer timepoints (42 to 140 days) reaffirms the substantial role intact scaffolds play on the overall mechanical response of composites. Though the transitional period (that which occurs as the intact scaffold degrades sufficiently to a discontinuous short fiber) seems to occur between 7 and 42 days and represents a range of timepoints that explants were not obtained from in vivo experiments, the properties observed before (intact scaffold) and after (fragmented short fibers) present clear evidence that the 7 to 42 day timepoint warrants further experimental analyses.

The biaxial mechanical data shows small changes with early implant duration; both the preferred and cross-preferred directions show an increase in stretch at peak stress. Values are not statistically significant from one another, but the trend suggests the change in response is likely due to scaffold volume fraction decrease instead of significant tissue accretion. Though not statistically significant, a trend is evident in the long timepoint TEC stretch at peak equibiaxial stress, showing an increase in stretch in the preferred direction towards the cross-preferred direction mean stretch by the 140 day timepoint. This suggests that the tissue is reorganizing in a manner to distribute stresses in both directions equally while increasing overall compliance in the tissue. Uniaxial failure experiments show strain at failure to be exceptionally similar between the TECs and native tissues.

Overall, the formed tissue at all timepoints appeared coherent and substantiate. Histology both en face and transmural displayed signs of granulation with macrophage infiltration, though foreign body giant cells were minimal, if at all, in the three timepoints. In the long timepoint TECs, a qualitative comparison between H&E and picrosirius stained slides provides compelling evidence for more mature granulation with increased collagen at longer implant durations. Importantly, inflammation and macrophage localization seemed to appear around remaining scaffold remnants and not the overall composite, suggesting that the tissue constituent of the composite integrated into the host reasonably well by these later timepoints.

From a structural standpoint, overall collagen alignment does not seem to change with implant time. It is assumed that the scaffold phase still dominates the overall orientation at the short implant TECs, but SALS data suggests this orientation is preserved at the later timepoints as well. While scaffold degrades rapidly during the initial implant time, it does not change as rapidly from 42 days on. From the picrosirius red histology, substantial collagen accretion was not observed in the longer timepoint TECs. This suggests that structural changes (i.e. crimping, cross linking) are occurring in the collagen in order to produce the observed changes in the mechanical properties. With the use of polarized light microscopy, evidence of collagen crimp was observed in the 84 and 140 day implant duration specimens, contrasting with the 42 day group which did not show signs of crimp. Though not quantified in this study, the presence of crimp in the later timepoint implant groups, coupled with the changes in mechanical properties further reinforces the structure-function relationship and provides qualitative evidence of changing structural properties.

5.4.2 Insights into tissue remodeling through structural constitutive models

The results from the continuous scaffold fiber constitutive modeling work suggest that little remodeling is taking place at the early time point. Scaffold volume fraction decreases during the initial period, but the tissue shear modulus does not change substantially between the 0 and 7 day implant durations. Even at a relatively low volume fraction, the scaffold phase still produces the dominant stress response in the composite. Using average deformations from the 42 day implant group, the 0, 1, and 7 day implant groups showed very low peak equibiaxial stress values, and were less than 5% of the peak equibiaxial stress value in the 42 day implant group. As such, it is clear that the selection of the appropriate material and quantity of scaffold is important in controlling much of the composite response during the initial implant duration.

In the long implant duration constitutive model, two distinct changes can be observed in the tissue. First, the effective fiber stiffness is increasing with implant duration. When normalized by collagen volume fraction, the changes are still evident. This suggests that collagen at later duration implants (84 and 140 days) is intrinsically stiffer and not the result of increased collaged accretion. Collagen cross-linking could be a mechanism by which the effective stiffness is increasing; it is well known in the literature that collagen maturation often manifests in increased cross-linking [101, 102].

Second, the recruitment function changes substantially between the three groups, notably the 42 and 84/140 day implant durations. In the 42 day TEC group, the recruitment function takes on a relatively broad form, which from a structural standpoint could be from a large range of fiber crimp values. As a result, fibers are “activated” to bear load in a very broad manner across the strain bounds. At full recruitment, this results in a wide range of fiber stresses. In the later implant duration groups (84 and 140 day), the recruitment function takes on a very different form, displaying a long “toe” region or limited collagen “activation” followed by a large peak near the upper bound strain. At full recruitment, such a response shows a tighter stress distribution. At the early timepoints, such a distribution of collagen crimp could be from increased collagen accretion without much collagen organization (crimp). Although this study did not investigate TECs in the 7-42 day implant range and comments on events occurring in this range are speculative, it is possible that a substantial increase in collagen deposition occurred across this time without substantial organization. After the large collagen deposition, collagen appears to have increased in stiffness and reorganized to a more uniform fiber crimp distribution, favoring recruitment at larger strain values.

5.4.3 Relation to vascular tissue remodeling

Over the past thirty years, a substantial amount of research has been undertaken to investigate remodeling of vascular tissues. In both the early work on arterial wall mechanics done by Fung and Vaishanav [103], residual stresses were shown to exist independent from external loading. It was shown that these residual stresses significantly reduced predicted large transmural wall stress gradients [104]. Such observations have led investigators like Humphrey and others to suggest a homeostatic target value of stress within arterial tissues to provide a nearly uniform and equibiaxial distribution of wall stresses at maturity [60]. Interestingly, similar observations have been made at multiple length and time scales pointing towards the existence of a "ubiquitous mechanical homeostasis in vascular biology" [60].

In the early implant duration TECs, at trend towards a homeostatic stress value was not observed as the previously described structural effects of the scaffold likely overpowered the early-deposited collagen. Though calculations to estimate average collagen fiber stress are left to be performed in future research efforts, tissue changes suggestive of trends toward homeostatic collagen stress was observed in the long implant TECs. With the majority of scaffold degraded and collagen deposited, collagen fiber orientation did not seem to change at these later points. The manner in which collagen recruited, however, did change, with later timepoints showing fiber recruitment more tightly around larger strain values. This shift would prevent many collagen fibers in the 84/140 day groups from fully straightening (and thus bearing load) at stretch values where many collagen fibers are bearing load in the 42 day group. Importantly, even with an increase in the effective collagen fiber modulus (notably in the 140 day group), the tighter recruitment distribution would reduce the fiber stress variation, even if the average value is larger in the 140 day group compared to early timepoints.

5.4.4 Comparison to published studies on tissue formation in TECs

Two studies are known to explore mechanical properties of TECs implanted in vivo. Hoerstrup et al. [31] seeded PGA scaffolds with vascular derived myofibroblasts and endothelial cells and implanted constructs into an ovine model from 140 to 700 days. Uniaxial tests were performed upon explant. At the only common timepoints (140 days), the current work showed larger values for tangent modulus and ultimate tensile strength compared to Hoerstrup's work [31], but both sets of values seem to exceed that of the native tissue. Little change in these properties was observed after 140 days in Hoerstrup's work. Interestingly, strain at failure approached native-like properties in the current study, which is a departure from the work by Hoerstrup et al. where strain at failure was substantially lower at the longer timepoints. Sodian et al. [105] performed similar ovine in vivo experiments using vascular cell-seeded polyhydroxyalkanoate scaffolds and performed uniaxial mechanical testing at 7, 35, and 91 days post-implant. Mechanical results, notably those of tangent modulus and ultimate tensile strength, paralleled those found in this present study with a sharp decrease observed between 7 and 35 days. Interestingly, tangent modulus and ultimate tensile strength continued to decrease in Sodian's work, whereas these values increased in the present study. Strain at failure, however, showed similar results at the endpoint of both studies. In both comparable studies, limited structural information was provided, especially as it related to mechanical properties, and no additional mechanical evaluation (i.e. physiological testing such as biaxial tension) was performed. It should be cautioned that uniaxial experimental data, in and of itself, may be misleading as it represents conditions at failure (and often supra-physiological).

5.4.5 Study limitations

One limitation in this work is the number of available TECs on which to perform structural and mechanical analyses, though it should be noted that few other in vivo studies have been described in literature. The 0 day and 42 day timepoints especially suffered from a small sample size of three. Experimental work from chapter 4 indicates that the scaffold fiber-ECM interactions are not limited to extensional effects but likely are impacted by scaffold-matrix shearing. Although not explored in the current work, future work will be done to fully address the shearing interactions. Due to the overall low matrix shear modulus in the 0, 1, and 7 day groups, such additional effects will likely only reduce these estimates further. Additionally, not having specific knowledge of the fiber-matrix interface shear stress raises may raise some questions, though the theoretically-based calculations and PAM gel – fragmented scaffold experiments have certainly provided much support for very limited reinforcing effects. Finally, it should be noted that different scaffolds and cell types will likely have different effects on the quantity and quality of tissue formed at specific implant durations. Though this study was limited to one cell type (BMSCs) and scaffold material (NNW PGA:PLLA), the general approach is applicable for future studies using different cell types/scaffold materials.

5.5 SUMMARY

Using structurally guided large-deformation constitutive models, changes in the tissue phase mechanical properties in in vivo TECs were investigated as a function of implant duration. The strong impact of initially scaffold orientation on “guiding” collagen deposition was observed up to 140 days post implant. Initial tissue-scaffold composite mechanical properties were dominated by the intact scaffold phase with little change in tissue shear modulus between 0 and 7 days implant duration. By 42 days, the scaffold phase was negligible, and dense collagen was observed. Model parameters suggest limited cross linking and crimping of collagen fibers. By 84 and 140 days, however, substantial increases in the effective collagen modulus and substantial shifts in the collagen ensemble recruitment function indicate increased collagen cross linking and collagen crimp. Histology showed evidence of crimping, as well as dense collagen. Importantly, the experimental and modeling results indicate that a substantial amount of remodeling occurs during the 7-42 day implant time. With this work, insights into how TECs remodel and change with implant time are discussed. Further, an important in vivo range of time for the remodeling process is shown, with future work focused on the 7-42 day time period.

6.0 SUMMARY AND CONCLUSIONS

6.1 MAIN FINDINGS OF THIS WORK

6.1.1 Overall approach to investigating tissue formation and remodeling in engineered tissues

In this work, a methodical approach to investigating tissue formation and remodeling in engineered tissues has been presented. Using high resolution 3D imaging and structural quantification techniques in chapter 2, constitutive models were developed driven by the presence of the scaffold phase in chapter 3. Unlike previous modeling efforts, the forms presented in this work were developed to have broad applicability as well as permit different deformation modalities. This was important, as the variety of scaffold materials and architectures will likely continue to increase and it is desirable to have model forms that can accommodate these varieties. Validation and model parameter estimation procedures were presented in chapter 4 using a unique "tissue analog" system. The use of PAM gel as detailed in this work provides matrix properties that are both tunable and on the order of native properties. This was crucial in determining both the matrix-scaffold interaction in the continuous scaffold model form as well as the lack of interaction in the discontinuous scaffold model form. Although the particular degree of interaction will likely change with the scaffold selection, the procedure laid out chapter 4 provides a general means to evaluate matrix-scaffold interactions. Finally, the approach developed in chapters 2-4 was applied to the clinically relevant scenario of tissue engineered pulmonary valved conduits in chapter 5. With this approach, insight was gained into how the tissue phase of the tissue-scaffold composites changed with implant duration and how the remaining scaffold had an impact on the overall mechanical properties. Further, the structurally-guided modeling form permitted the investigation of underlying structural changes (such as collagen orientation, intrinsic modulus, and crimping) and how these changes impacted the tissue properties. With the approach and clinical application detailed in this work, it is the hope that such efforts can be used to continue the understanding of tissue formation and remodeling in engineered tissues and ultimately create more functional tissues.

6.1.2 3D structural changes in engineered tissues

Structural information obtained from high-resolution 3D acquisition methods is essential for understanding both initial cell seeding conditions and intermediate states at various implant timepoints. In this study, it was shown that virgin PGA:PLLA scaffold is slightly tortuous, aligned with a preferred and cross-preferred direction, and relatively porous. Importantly, these morphological features were quantified using three-dimensional data. The time-dependent morphological change was also shown in the scaffolds. After an initial static in vitro culture, scaffold material showed volume loss while maintaining fiber continuity. This provided insight into the structural composition of the composite (tissue and scaffold). Further, it was shown that much of the original alignment seen in the virgin scaffold state was maintained after 28 days static culturing. After 84 days of in vivo implantation, however, significant changes to the scaffold morphology were observed. Specifically, the scaffold became highly fragmented, disconnected, and randomly oriented. In both timepoints, the 3D information provided guidance with how to model the mechanical properties of the tissue-scaffold composites.

Although not practical to perform on every specimen, the imaging and subsequent analysis technique discussed also provided a means to characterize the minimum number and frequency of 2D images needed to capture salient structural details in the engineered tissue. In summary, this work yielded quantitative structural information, guided model selection, and provided insight into the acquisition of further morphological information.

6.1.3 Tissue formation and remodeling in short timepoint in vivo TECs

A summary of the main experimental and modeling findings is shown in Figure 6.1. Using the structural constitutive model developed for continuous scaffold fiber-ECM composites, the biaxial mechanical data of short implant time (0, 1, and 7 day implant durations) TECs was investigated in chapter 5. Though scaffold volume fraction decreased significantly, the estimated matrix shear modulus of the formed tissue did not change. This suggests that the slight changes in biaxial mechanical properties (manifesting in increased stretch at peak stress in both directions) were due to decreased amount of scaffold (and hence decreased scaffold-ECM interactions). It is not surprising that little change to the tissue phase is evident throughout the short implant duration as the scaffold phase likely supports the bulk of the mechanical load. Further, this suggests (alongside accompanying histology) the immunogenic response of the host is minimal with the implant, as any thrombogenic/strong inflammatory response could likely increase the overall composite stiffness. The insights from this study provide opportunities for additional future work to investigate how tissue forms in vitro and with different scaffold materials (i.e. faster degradation, lower volume fraction etc.).

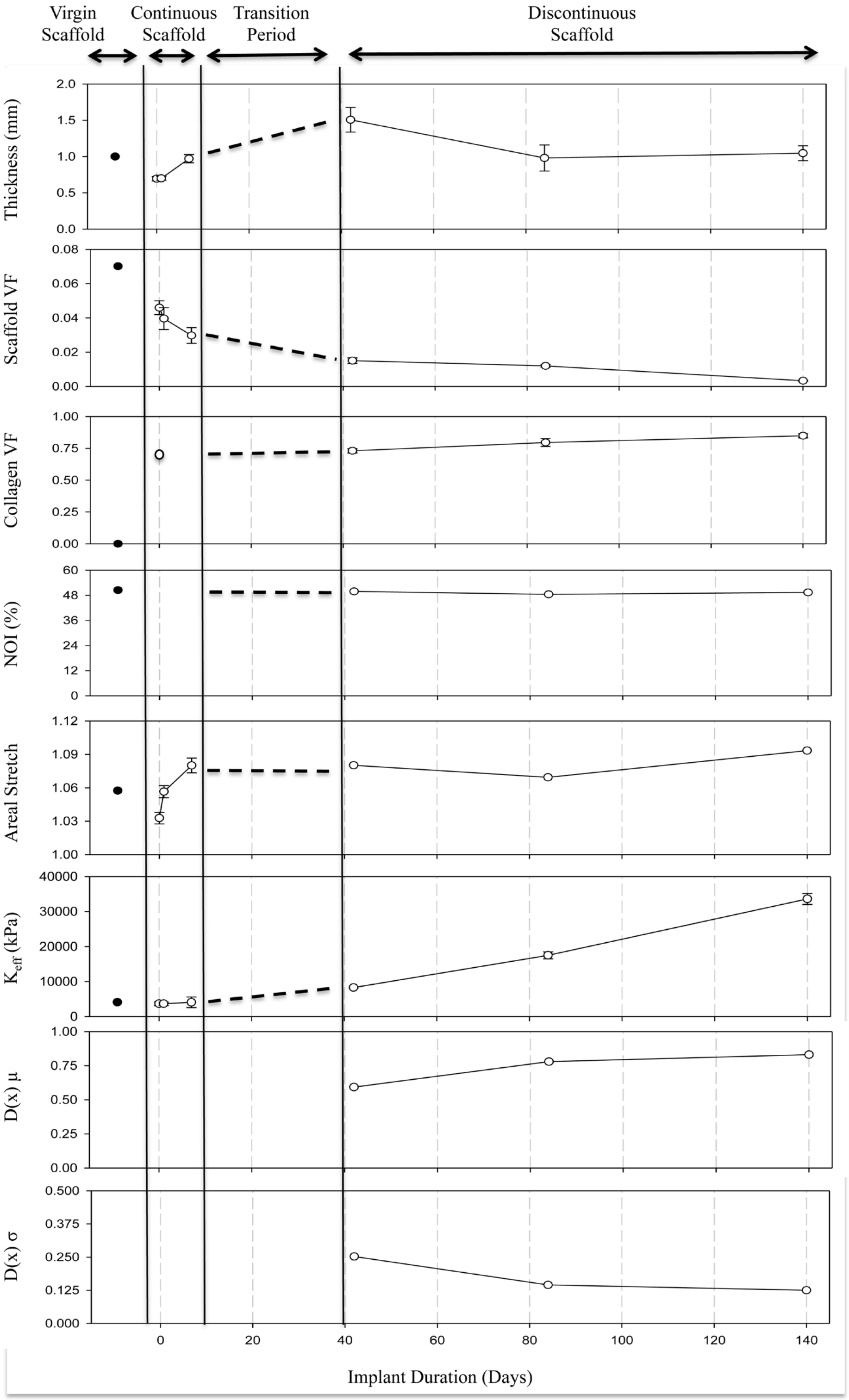

Figure 6.1. Summary plots of mechanical and structural changes to TECs with implant time. White circles indicate TECs; black circles indicate virgin scaffold material. Dotted lines represent possible transition period trend. The implant duration is broken down into virgin scaffold, continuous scaffold, transition period, and discontinuous scaffold phases.

6.1.4 Tissue formation and remodeling in long timepoint in vivo TECs

In this work, the ramifications of the 3D imaging and analysis results discussed in section 2.3.3 on long timepoint TEC implants were considered with regards to constitutive model formulation. Specifically, it was shown that additional factors must be considered when the composite structurally takes the form of a short fiber reinforced composite material. A methodical procedure was shown for addressing the short fiber (discontinuous) fiber phase in modeling, as well as theoretical and experimental evidence that such reinforcing was unlikely in the particular TEC system of interest. A constitutive model form was presented and used to decouple structural effects (constituent orientation distribution) from effective mechanical responses (effective tissue stress response) in native, 42, 84, and 140 day implants using biaxial mechanical data. Structural analyses using small angle light scattering and traditional histology (H&E and picrosirius red) was used to investigate architectural indications of remodeling. Significant scaffold volume fraction change was observed compared to the initial scaffold volume fraction, as well as a trend towards potentially more mature and crimped collagen.

Figure 6.1 shows a graphical summary of the main findings with regards to long implant TECs. Mechanical data showed an increase in tissue strength (both from uniaxial data and modeling analysis) as well as an increase in compliance in the initial loading regime with implant duration. A comparison to previous studies reveals increased tensile strength and tangent modulus in the present work, with a more native-like strain at failure (uniaxial) response. In biaxial tension, specimens tended to behave less anisotropic as the preferred direction increased compliance. Using the structural model, it was shown that little change in collagen fiber orientation occurred over the implant duration, suggesting an “imprinting” effect of the original scaffold. Thus, the intact scaffold impacted the orientation in the initially forming collagen. In an effort to reach a collagen ensemble homeostasis, intrinsic properties of collagen such as crimp and cross-linking were likely the only mechanisms available to the tissue to adapt. Investigation into the recruitment function revealed substantial changes through the 42 to 140 day implant duration, with initially uniform (mean at center with large standard deviation) recruitment distribution to a highly skewed distribution (mean towards the upper bound stretch with small standard deviation). Physically, this suggests ensembles displayed similar levels of crimp, and that the amount of crimp increased.

6.1.5 Summary of main findings

As shown in Figure 6.1, the implant timepoints from the TECs can be discretized into three time ranges based on scaffold condition: continuous scaffold (0-7 days), discontinuous scaffold (42-140 days), and the transition region (roughly 7-42 days). Virgin scaffold properties are also shown, where appropriate, to give a baseline prior to cell seeding and in vitro culturing. A list of important finds is as follows:

1. Based on high resolution 3D imaging, reconstruction, and structural quantification, the scaffold phase changes from a continuous scaffold to a discontinuous (highly fragmented scaffold) over an 84 day time period.
2. Based on experimental evidence using a tissue analog, the reinforcing impact on the continuous scaffold from matrix-scaffold interactions is substantial and greatly effects the overall mechanical properties.

3. From experimental and theoretical evidence, the discontinuous scaffold phase does not contribute mechanically to the overall composite properties in these current materials.
4. In the initial implant timepoint, TECs show tissue accretion, though the majority of mechanical strength results from the intact scaffold phase. The scaffold phase loses volume fraction but remains intact.
5. At longer implant timepoints (greater than 42 days), TECs show stable tissue accretion that maintains the orientation of the degraded and highly fragmented scaffold ("imprinting" effect).
6. TECs show a change in collagen fiber properties, as fibers increase in effective modulus (i.e. probable cross-linking) and shift in recruitment (i.e. crimp organization). Though areal stretch does not change substantially, the specimen directions display less anisotropy at the later implant timepoints, with the 140 day group approaching a nearly isotropic tissue response.

6.2 OVERALL STUDY LIMITATIONS

In the first portion of this work (chapter 2), a limitation was the lack of engineered conduit tissue on which to perform the imaging work. Unfortunately, only leaflet portions of valved conduits were available to transfer to the EV-SLCM location in New Zealand. When conduit specimens were available, logistics and cost limited the ability to return to perform additional studies. As a result, scaffold morphological information and two dimensional sectioning information was determined for engineered leaflet tissue and not conduit. At the shorter timepoints, it was assumed that the continuous scaffold fibers observed in the leaflet tissue was present in conduit tissue. Since implant times were short (up to 7 days) in the first study (chapter 3), the transition from continuous to discontinuous scaffold likely did not occur in the conduit at the early timepoints. Histological analyses showed relatively high volume fractions of scaffold at 1 to 7 days and both en face and transmural sections at 7 days showed the presence of long interacting fibers. For the long term implant studies (chapter 4), histological evidence suggested that scaffold volume fractions were no greater in the conduits than the leaflets and, in fact, were less at most timepoints than what was measured in the leaflets. As a result, it is a reasonable assumption that present scaffold existed as a discontinuous phase in the conduit since the leaflet showed highly fragmented scaffold. Most likely any differences between the continuous-discontinuous scaffold transition occurred during the 1 to six week in vivo period of which was not investigated in this study.

The sample sizes for most timepoints, especially the 42, 84, and 140 day implant durations were less than ideal. In a few instances, specimens were available but were too small for mechanical testing and could not be used. Given the difficulty and cost of large animal in vivo studies, it is anticipated that sample size may continue to be present in future studies. In the two cited studies reported mechanical data of TECs, sample sizes ranged from 1 per group [105] to 2-4 [31] per group. The present study improved upon previous work with sample sizes ranging from 3-11 per group. Still, additional implanted TECs would help to account for normal variations observed when working with soft tissues.

The use of collagen volume fraction, by itself, is not an ideal metric for evaluating changes to collagen in forming/remodeling tissues. It is possible that collagen density could change without substantial changes to the volume fraction. Though polarized picrosirius red histology does provide insight into collagen type and maturity, this may be convoluted in systems where collagen production occurs alongside collagen maturation (i.e. both effects may produce similar qualitative results with respect to polarized picrosirius red histology). Thus, this metric is insufficient to evaluate forming/remodeling tissue. With use of the structural constitutive model, however, changes to collagen properties were evident, such as increases in the effective modulus and crimp, both suggestive of collagen maturation.

Using PAM gel as a tissue analog could also create limitations in the study as it may not fully mimic forming and remodeling tissue. Often, soft tissues are nonlinear and anisotropic, and PAM gel was observed to be linear and highly isotropic. Usage of PAM gel was justified by a number of reasons. Because the scaffold phase dominated the overall mechanical response during the early implant timepoints, tissue anisotropy was likely overshadowed by scaffold anisotropy and differences from using an isotropic tissue analog likely did not significantly affect the results. In the longer implant durations, the scaffold was assumed to have a random 3D orientation which forced any observe anisotropy to be the result of tissue effects. Since the scaffold was shown to not have a reinforcing effect on tissue, no additional modeling work was required to understand the interaction. As such, a constitutive model that could handle anisotropic tissue response was utilized.

The scaffold embedded PAM gel studies (chapter 2 and 3) relied heavily on the assumption that PAM gel interacted with the scaffold in the same manner as tissue. Although differences may exist, the specific requirements for the tissue analog (able to be cast, tunable shear modulus, safe to create, no harsh solvents that could degrade scaffold, etc.) limited possible choices. Future studies could be aimed at investigating possible differences between scaffold interactions with PAM gel and tissue.

In the short implant duration study, this may have an effect on the magnitude of observed reinforcement of the scaffold. Overestimating this effect would underestimate the true mechanical response of the tissue phase, while underestimating it would have the opposite effect. Based on the ability of collagen to adhere to PGA and PLLA surfaces [6], both PAM gel and tissue adhered equally well to the scaffold. If differences did exist, they would likely manifest in a stronger reinforcing effect, which would underestimate the tissue phase. In the long implant duration study, a very conservative estimate was provided for the interface shear stress term that probably exceeds the properties of native tissue. With the large fiber modulus and small fiber aspect ratio, even larger estimates for interface shear stress would still result in exceptionally long fiber critical lengths, beyond what was measured experimentally. A smaller interface shear stress would serve to reduce reinforcing effects. Since the scaffold phase was assumed to not contribute at all to the mechanical response, a lower actual interface shear stress between the scaffold and the tissue would have only strengthened such claims.

Finally, only one cell type and scaffold material were utilized in this study. Though this consistency is important to compare and evaluate tissue formation/remodeling at different implant durations, it should be noted that the quantitative results observed in this study are likely specific to the cell type/scaffold material system utilized. Switching to a different cell source may improve collagen deposition or remodeling rates, while different scaffold materials may inhibit or promote changes to the collagen. Overall, however, the approach in the system utilized in this study is applicable to other experimental variables (cell type, conditioning, scaffold material, implant model, etc.) and provides a guide for future work.

6.3 FUTURE STUDIES

6.3.1 Further characterization of native pulmonary arteries

Important to any tissue engineering work, understanding the native properties one desires to replicate is crucial to assessing the success of the work. A significant gap exists in the literature regarding the native structural and mechanical properties of native pulmonary artery. As the present work was primarily about the experimental and theoretical approach to understanding tissue formation and remodeling, substantial effort was not expended in elucidating the properties of native pulmonary artery. Initial characterization was performed (i.e. limited mechanical studies) as a means of comparison to TECs, but further studies should not proceed without first quantifying the underlying structural architecture and overall mechanical response of such tissues. Importantly, this work should be performed over a range of developmental stages so that insight into physiological remodeling responses may be obtained. This also could provide valuable information for implant design based on patient age.

6.3.2 Investigation of seven to forty-two day implant timepoints in TECs

The results in chapters 2 and 3 corroborate with work by Sodian et al. [105], and to a lesser extent, Hoerstrup et al. [31] regarding the significant changes in TEC mechanical properties that occur between 7 and 42 days in vivo. To fully understand the process of remodeling in engineered tissues, this important phase should be investigated. Over this time course, the scaffold phase transforms from a continuous fiber network to a discontinuous system. Insight into structural and mechanical changes through this time range could permit the formulation of a single constitutive model from intact scaffold to fully degraded scaffold. Additionally, knowledge of how the structure and function change – both in the tissue and the scaffold – could lead to better functional equivalency. Since this implant time range contains the transition from a continuous to discontinuous scaffold phase, the tissue phase must also take on a changing amount of mechanical loading. How and when this mechanism occurs (notably if it happens suddenly or slowly over the time period) could influence the selection of polymer type or cell source. A rapid transition could potentially lead to premature failure of the construct if the tissue phase is not strong enough. A slow transition could excessively prolong inflammation and hinder further remodeling. Additional in vivo animal model studies would greatly further understanding of the remodeling process and could potentially serve to improve TEC performance.

6.3.3 Detailed in vitro studies on the effects of mechanical stimuli on tissue formation and remodeling

Although the in vivo phase likely provides the closest environment to native physiological conditions, it precludes the decoupling of specific mechanical stimuli on tissue formation and remodeling and serves to complicate the understanding of crucial mechanisms. In vitro studies offer the potential of investigating single mechanical loading regimes (i.e. dilation, tension, flow, etc.), though most studies found in the literature are complicated by the inconsistent use of various cell and scaffold types (sources). Using a consistent cell source and scaffold type especially as related to those used in the in vivo studies, could provide valuable insight into the remodeling process and the specific mechanical stimuli that influence it. Such a study could be useful in guiding improved scaffold selection, as the effects of specific loading regimes may require specific scaffold architectures or mechanical responses.

Importantly, investigating the effects of mechanical stimuli could lead to better in vitro culturing procedures to ensure the presence of robust and viable tissue prior to implantation.

Often, much of the in vitro work in culture has limited physiological basis and involves experimental conditions based on simplifying the experiment or device limitations [61, 62, 106, 107]. Since many tissues are required to function immediately upon implantation, the initial properties are critical to the success of the construct. Means to facilitate such tissue formation to the point of benefiting the overall functionality would prove advantageous to improving the state of TECs. Previous work has shown the importance of flexure and flow (more physiological conditions) for increasing collagen robustness and transmural distribution in engineered heart valves [108]. More recent studies by Ramaswamy et al. [109], have shown optimistic preliminary results exposing BMSC-seeded PGA:PLLA scaffolds to combined flexure/flow conditions (producing an "oscillatory shear" condition) with improved collagen deposition. Interestingly, these positive results correspond to in vitro conditions more closely replicating the in vivo state, and suggest that the most successful in vitro culturing may result from conditions most similar to the in vivo state. This is intuitive, though investigating isolated effects (flexure apart from fluid flow, pulsatile flow apart from uniaxial stretch, etc.) could provide a unique insight into what effects have the greatest impact. Obviously, despite its proliferate occurrence in literature, much works yet remains on understanding mechanical stimuli and in vitro culturing.

6.3.4 Characterization of the scaffold-tissue interface

In the model formulations, the scaffold-tissue interface was either considered perfectly bonded (continuous scaffold fiber model) or perfectly decoupled (discontinuous scaffold fiber), and such assumptions were essential to the model selection. Although experimental work provided some qualitative insight into the interface, more detailed studies could further improve modeling efforts. A fiber pullout test using a single scaffold fiber partially embedded into a matrix of known mechanical properties could provide this information. Performing such an experiment while varying matrix properties would yield a relationship between interface shear strength and matrix strength. This could be used in determining the true scaffold fiber critical length and whether embedded fibers are capable of carrying applied load for a given embedded fiber length. For continuous scaffold systems, it could help separate intrinsic reinforcing effects (evaluated using the rule of mixtures and representing perfect fiber-matrix bonding) from the increased reinforcing effects observed in chapter 2.

BIBLIOGRAPHY

1. Langer, R. and J.P. Vacanti, *Tissue Engineering.* Science, 1993. **260**: p. 920-926.

2. Badylak, S., *The extracellular matrix as a biologic scaffold material.* Biomaterials, 2007. **28**: p. 3587-3593.

3. Simon, P., et al., *Early failure of the tissue engineered porcine heart valve SYNERGRAFT in pediatric patients.* Eur J Cardiothorac Surg, 2003. **23**(6): p. 1002-6; discussion 1006.

4. Williams, C., et al., *Altered structural and mechanical properties in decellularized rabbit carotid arteries.* Acta Biomater, 2009. **5**(4): p. 993-1005.

5. Freed, L.E., et al., *Biodegradable Polymer Scaffolds for Tissue Engineering.* Nature Biotechnology, 1994. **12**: p. 689-693.

6. Ratner, B., et al., eds. *Biomaterials Science, 2nd Ed.* 2004, Elsevier Academic Press: San Diego.

7. Courtney, T., et al., *Design and analysis of tissue engineering scaffolds that mimic soft tissue mechanical anisotropy.* Biomaterials, 2006. **27**(19): p. 3631-8.

8. Stankus, J.J., J. Guan, and W.R. Wagner, *Fabrication of biodegradable elastomeric scaffolds with sub-micron morphologies.* J Biomed Mater Res, 2004. **70A**(4): p. 603-14.

9. Engelmayr, G.C. and M.S. Sacks, *A structural model for the flexural mechanics of nonwoven tissue engineering scaffolds.* J Biomech Eng, 2006. **128**: p. 610-622.

10. Hearle, J.W.S. and T.N. Choudhari, *A study of needled fabrics; part VII: the transfer of fibres through the web by needling.* Journal of the Textile Institute, 1969. **60**: p. 478-496.

11. Hearle, J.W.S. and A.T. Purdy, *The structure of needle punched fabric.* Fibre Science and Technology, 1971. **4**: p. 81-100.

12. Hearle, J.W.S. and M.A.I. Sultan, *A study of needled fabrics; part I: experimental methods and properties.* Journal of the Textile Institute, 1967. **58**: p. 251-265.

13. Fung, Y.C., *Biomechanics: Mechanical Properties of Living Tissues*1981, New York: Springer-Verlag.

14. Holzapfel, G.A., T.C. Gasser, and R.W. Ogden, *Comparison of a multi-layer structural model for arterial walls with a fung-type model, and issues of material stability.* J Biomech Eng, 2004. **126**(2): p. 264-75.

15. Lanir, Y., *Constitutive Equation for the Lung Tissue.* Journal of Biomechanical Engineering, 1983. **105**: p. 374-380.

16. Lanir, Y. and Y.C. Fung, *Two-dimensional mechanical properties of rabbit skin. II. Experimental results.* J Biomech, 1974. **7**(2): p. 171-82.

17. Sun, W., et al., *Biaxial mechanical response of bioprosthetic heart valve biomaterials to high in-plane shear.* Journal Biomechanical Engineering, 2003. **125**: p. 372-380.

18. Rodriguez, E.K., A. Hoger, and A.D. McCulloch, *Stress-dependent finite growth in soft elastic tissues.* J Biomech, 1994. **27**(4): p. 455-67.

19. Taber, L.A. and D.W. Eggers, *Theoretical study of stress-modulated growth in the aorta.* J Theor Biol, 1996. **180**(4): p. 343-57.

20. Taber, L.A., *Biomechanics of growth, remodeling, and morphogenesis.* Applied Mechanics Reviews, 1995. **48**: p. 487-545.

21. Humphrey, J.D., *An evaluation of pseudoelastic descriptors used in arterial mechanics.* J Biomech Eng, 1999. **121**(2): p. 259-62.

22. Zahalak, G.I., et al., *A cell-based constitutive relation for bio-artificial tissues.* Biophys J, 2000. **79**(5): p. 2369-81.

23. Engelmayr, G.C., Jr. and M.S. Sacks, *Prediction of extracellular matrix stiffness in engineered heart valve tissues based on nonwoven scaffolds.* Biomech Model Mechanobiol, 2008. **7**(4): p. 309-21.

24. Niskanen, K., Paper Physics. Papermaking Science and Technology; bk. 16. 1998, Helsinki; Atlanta: Published in cooperation with the Finnish Paper Engineers' Association and TAPPI. 324.

25. Sands, G.B., et al., *Automated imaging of extended tissue volumes using confocal microscopy.* Microsc Res Tech, 2005. **67**(5): p. 227-39.

26. Lee, J.M., D.R. Boughner, and D.W. Courtman, *The glutaraldehyde-stabilized porcine aortic valve xenograft. II. Effect of fixation with or without pressure on the tensile viscoelastic properties of the leaflet material.* Journal of Biomedical Materials Research, 1984. **18**: p. 79-98.

27. Lee, J.M., D.W. Courtman, and D.R. Boughner, *The glutaraldehyde-stablized porcine aortic valve xenograft. I. Tensile viscoelastic properties of the fresh leaflet material.* Journal of Biomedical Materials Research, 1984. **18**: p. 61-77.

28. Vesely, I. and R. Noseworthy, *Micromechanics of the fibrosa and the ventricularis in aortic valve leaflets.* Journal of Biomechanics, 1992. **25**(1): p. 101-113.

29. Billiar, K.L. and M.S. Sacks, *Biaxial mechanical properties of the native and glutaraldehyde-treated aortic valve cusp: Part II--A structural constitutive model.* J Biomech Eng, 2000. **122**(4): p. 327-35.

30. Billiar, K.L. and M.S. Sacks, *Biaxial mechanical properties of the natural and glutaraldehyde treated aortic valve cusp--Part I: Experimental results.* J Biomech Eng, 2000. **122**(1): p. 23-30.

31. Hoerstrup, S.P., et al., *Functional growth in tissue-engineered living, vascular grafts: follow-up at 100 weeks in a large animal model.* Circulation, 2006. **114**(1 Suppl): p. I159-66.

32. Green, A., *Outcomes of congenital heart disease: a review.* Pediatric nursing, 2004. **30**(4): p. 280-4.

33. Mayer, J.E., Jr., T. Shin'oka, and D. Shum-Tim, *Tissue engineering of cardiovascular structures.* Curr Opin Cardiol, 1997. **12**(6): p. 528-32.

34. Mirensky, T.L. and C.K. Breuer, *The development of tissue-engineered grafts for reconstructive cardiothoracic surgical applications.* Pediatric research, 2008. **63**(5): p. 559-68.

35. Yuan, S.M., et al., *Right ventricular outflow tract reconstruction: valved conduit of choice and clinical outcomes.* Journal of cardiovascular medicine, 2008. **9**(4): p. 327-37.

36. Shinoka, T., et al., *Creation of viable pulmonary artery autografts through tissue engineering.* J Thorac Cardiovasc Surg, 1998. **115**(3): p. 536-45; discussion 545-6.

37. Dearani, J.A., et al., *Late follow-up of 1095 patients undergoing operation for complex congenital heart disease utilizing pulmonary ventricle to pulmonary artery conduits.* The Annals of thoracic surgery, 2003. **75**(2): p. 399-410; discussion 410-1.

38. Deasy, B.M., Y. Li, and J. Huard, *Tissue engineering with muscle-derived stem cells.* Curr Opin Biotechnol, 2004. **15**(5): p. 419-23.

39. Tokunaga, S., et al., *Total cavopulmonary connection with an extracardiac conduit: experience with 100 patients.* The Annals of thoracic surgery, 2002. **73**(1): p. 76-80.

40. Azakie, A., et al., *Extracardiac conduit versus lateral tunnel cavopulmonary connections at a single institution: impact on outcomes.* The Journal of thoracic and cardiovascular surgery, 2001. **122**(6): p. 1219-28.

41. Leyh, R.G., et al., *Tissue engineering of viable pulmonary arteries for surgical correction of congenital heart defects.* The Annals of thoracic surgery, 2006. **81**(4): p. 1466-70; discussion 1470-1.

42. Shin'oka, T., et al., *Midterm clinical result of tissue-engineered vascular autografts seeded with autologous bone marrow cells.* J Thorac Cardiovasc Surg, 2005. **129**(6): p. 1330-8.

43. Isomatsu, Y., et al., *Extracardiac total cavopulmonary connection using a tissue-engineered graft.* The Journal of thoracic and cardiovascular surgery, 2003. **126**(6): p. 1958-62.

44. Gerneke, D.A., et al., *Surface imaging microscopy using an ultramiller for large volume 3D reconstruction of wax- and resin-embedded tissues.* Microsc Res Tech., 2007. **70**(10): p. 886-94.

45. Gottlieb, D., et al., *In vivo monitoring of function of autologous engineered pulmonary valve.* J Thorac Cardiovasc Surg, 2010. **139**(3): p. 723-31.

46. Sands, G.B., et al., *Automated Extended Volume Imaging of Tissue using Confocal and Optical Microscopy.* Conf Proc IEEE Eng Med Biol Soc, 2006. **1**: p. 133-6.

47. Mikulis, B. and R.M. Rao, *Object labeling for 3-d cross-sectional data using trajectory tracking*, in *IEEE Conference on Image Processing*2006: Atlanta, GA.

48. Advani, S.G. and C.L. Tucker III, *The use of tensors to describe and predict fiber orientation in short fiber composites.* Journal of Rheology, 1987. **31**(8): p. 751-784.
49. Chung, T.W., et al., *Preparation of alginate/galactosylated chitosan scaffold for hepatocyte attachment.* Biomaterials, 2002. **23**(14): p. 2827-2834.

50. Lee, Y., et al., *Characterization of fiber orientation in short fiber reinforced composites with an image processing technique.* Materials Research Innovations, 2002. **6**(2): p. 65-72.

51. Regnier, G., et al., *A simplified method to determine the 3D orientation of an injected molded fiber-filled polymer.* Polymer Engineering and Science, 2008. **48**(11): p. 2159-2168.

52. Robb, K., O. Wirjadi, and K. Schladitz, *Fiber orientation estimation from 3D image data: practical algorithms, visualization, and interpretation.* Seventh International Conference on Hybrid Intelligent Systems, 2007: p. 320-325.

53. Sander, E.A. and V.H. Barocas, *Comparison of 2D fiber network orientation measurement methods.* Journal of Biomedical Materials Research Part A, 2009. **88A**(2): p. 322-331.

54. Sutherland, F.W., et al., *From stem cells to viable autologous semilunar heart valve.* Circulation, 2005. **111**(21): p. 2783-91.

55. Aidulis, D., et al., *Processing of ovine cardiac valve allografts: 1. Effects of preservation method on structure and mechanical properties.* Cell Tissue Bank, 2002. **3**(2): p. 79-89.

56. Della Rocca, F., et al., *Cell composition of the human pulmonary valve: a comparative study with the aortic valve--the VESALIO Project. Vitalitate Exornatum Succedaneum Aorticum labore Ingegnoso Obtinebitur.* Annals of Thoracic Surgery, 2000. **70**(5): p. 1594-600.

57. Hinton, R.B., Jr, et al., *Extracellular Matrix Remodeling and Organization in Developing and Diseased Aortic Valves.* Circ Res, 2006. **98**(11): p. 1431-1438.

58. Hoerstrup, S.P., et al., *Functional living trileaflet heart valves grown In vitro.* Circulation, 2000. **102**(19 Suppl 3): p. III44-9.

59. Holzapfel, G.A., *Nonlinear solid mechanics : a continuum approach for engineering*2000, Chichester ; New York: Wiley. xiv, 455.

60. Humphrey, J.D., *Vascular Mechanics, Mechanobiology, and Remodeling.* J Mech Med Biol, 2009. **9**(2): p. 243-257.

61. Rubbens, M.P., et al., *Intermittent Straining Accelerates the Development of Tissue Properties in Engineered Heart Valve Tissue.* Tissue Eng Part A, 2008.

62. Rubbens, M.P., et al., *Straining Mode-Dependent Collagen Remodeling in Engineered Cardiovascular Tissue.* Tissue Eng Part A, 2008.

63. Hoerstrup, S.P., et al., *New pulsatile bioreactor for in vitro formation of tissue engineered heart valves.* Tissue Eng, 2000. **6**(1): p. 75-9.

64. Rabkin, E., et al., *Evolution of cell phenotype and extracellular matrix in tissue-engineered heart valves during in-vitro maturation and in-vivo remodeling.* Journal of Heart Valve Disease, 2002. **11**(3): p. 308-14; discussion 314.

65. Azuma, N., et al., *Endothelial cell response to different mechanical forces.* J Vasc Surg, 2000. **32**(4): p. 789-94.

66. Baaijens, F., et al., *Functional tissue engineering of the aortic heart valve.* Clin Hemorheol Microcirc, 2005. **33**(3): p. 197-9.

67. Mol, A., et al., *Tissue engineering of human heart valve leaflets: a novel bioreactor for a strain-based conditioning approach.* Ann Biomed Eng, 2005. **33**(12): p. 1778-88.

68. Gogolewski, S., *Resorbable polymers for internal fixation.* Clinical materials, 1992. **10**(1-2): p. 13-20.

69. Li, J. and A.F. Mak, *Hydraulic permeability of polyglycolic acid scaffolds as a function of biomaterial degradation.* Journal of biomaterials applications, 2005. **19**(3): p. 253-66.

70. Andriano, K.P., T. Pohjonen, and P. Tormala, *Processing and characterization of absorbable polylactide polymers for use in surgical implants.* Journal of applied biomaterials : an official journal of the Society for Biomaterials, 1994. **5**(2): p. 133-40.

71. Roby, M. and J. Kennedy, *Sutures, Biomaterials Science: An Introduction to Materials in Medicine, 2nd Ed.*, ed. B. Ratner, et al.2004: Elsevier Academic Press.

72. Gilding, D. and A. Reed, *Biodegradable polymers for use in surgery -- poly(glycolic)/poly(lactic acid) homo- and copolymers: 2: in vitro degradation.* Polymer, 1981. **22**: p. 494-498.

73. Gilding, D. and A. Reed, *Biodegradable polymers for use in surgery -- poly(glycolic)/poly(lactic acid) homo- and copolymers: 1.* Polymer, 1979. **20**: p. 1459-1464.

74. Chou, T.-W., *Microstructural Design of Fiber Composites*1992, New York: Press Syndicate of the University of Cambridge.

75. Cox, H., *The elasticity and strength of paper and other fibrous materials.* British Journal of Applied Physics, 1952. **3**(3): p. 72-79.

76. Chou, T.-W. and A. Kelly, *Mechanical properties of composites.* Annual Review of Materials Science, 1980. **10**: p. 229-259.

77. Knight, M. and H. Hahn, *Strength and elastic modulus of a randomly-distributed short fiber composite.* Journal of Composite Materials, 1975. **9**: p. 77-90.

78. Zak, G., et al., *Mechanical properties of short-fibre layered composites: prediction and experiment.* Rapid Prototyping Journal, 2000. **6**(2): p. 107-118.

79. Sacks, M.S., *Incorporation of experimentally-derived fiber orientation into a structural constitutive model for planar collagenous tissues.* J Biomech Eng, 2003. **125**(2): p. 280-7.

80. Wognum, S., D.E. Schmidt, and M.S. Sacks, *On the mechanical role of de novo synthesized elastin in the urinary bladder wall.* J Biomech Eng, 2009. **131**(10): p. 101018.

81. Cox, H.L., *The elasticity and strength of paper and other fibrous materials.* British Journal of Applied Physics, 1952. **3**(3): p. 72-79.

82. Bowyer, W. and B. MG., *On the reinforcement of themoplastics by imperfectly aligned discontinuous fibers.* Journal of Materials Science, 1972. **7**.

83. Chen, P., *Strength properties of discontinuous fiber composites.* Polymer Engineering & Science, 1971. **11**.

84. Lees, J., *Strength-composition relationships of random short glass fiber-thermoplastics composites.* Polymer Engineering & Science, 1969. **9**: p. 213-24.

85. Lees, J., *A study of the tensile strength of short fiber reinforced plastics.* Polymer Engineering & Science, 1968. **8**.

86. Blumentritt, B., B. Vu, and S. Copper, *Mechanical properties of discontinuous fiber reinforced thermoplastics, II. Random-in-plane fiber orientation.* Polymer Engineering & Science, 1975. **15**: p. 428-436.

87. Lavengood, R., *Strength of short-fiber reinforced cmposites.* Polymer Engineering & Science, 1972. **12**.

88. McNally, D., *Short fiber orientation and its effect on the properties of thermoplastic composite materials.* Polymer-Plastics Technology and Engineering, 1977. **8**: p. 101-154.

89. Fu, S.-Y. and B. Lauke, *Effects of fibre length and fibre orientation distributions on the tensile strength of short-fibre-reinforced polymers.* Composites Science and Technology, 1996. **56**: p. 1179-1190.

90. Christensen, R.M., *Mechanics of Composite Materials*1979, New York: Wiley. 348.

91. McCullough, R., G. Jarzebski, and M. SH., *The Role of Polymer Matrix in the Processing and Structural Properties of Composite Materials*, ed. J.C. Seferis and L. Nicolais1983, New York: Plenum.

92. McGee, S. and R. McCullough, Polymer Composites, 1981. **2**(4): p. 149-161.

93. Halpin, J., *Primer on Composite Materials: Analysis*1984, Lancaster: Technomic.

94. Halpin, J. and J. Kardos, Polymer Engineering & Science, 1978. **18**(6).

95. Tsarnas, A. and J. Kardos, Proceedings from the 43rd Annual Technical Conference, SPE, 1985. **31**.

96. Lavengood, R. and L. Goettler, *US Government R&D Reports, AD886372*, National Technical Information Service.

97. Lanir, Y., *A structural theory for the homogeneous biaxial stress-strain relationships in flat collagenous tissues.* J Biomech, 1979. **12**(6): p. 423-36.

98. Peng, X.Q., Z.Y. Guo, and B. Moran, *An Anisotropic Hyperelastic Constitutive Model With Fiber-Matrix Shear Interaction for the Human Annulus Fibrosus.* Journal of Applied Mechanics, 2006. **73**(5): p. 815-824.

99. Sacks, M.S., D.B. Smith, and E.D. Hiester, *A small angle light scattering device for planar connective tissue microstructural analysis.* Ann Biomed Eng, 1997. **25**(4): p. 678-89.

100. Sacks, M.S., *Small-angle light scattering methods for soft connective tissue structural analysis.* Encyclopedia of Biomaterials and Biomedical Engineering, 2004.

101. Rowe, R.W., *The structure of rat tail tendon fascicles.* Connect Tissue Res, 1985. **14**(1): p. 21-30.

102. Broom, N.D., *Further insights into the structural principles governing the function of articular cartilage.* J Anat, 1984. **139**(Pt 2): p. 275-94.

103. Fung, Y.C., *Biomechanics: Motion, Flow, Stress, and Growth.* 1990: p. 569.

104. Vasita, R. and D. Katti, *Nanofibers and their applications in tissue engineering.* International Journal of Nanomedicine, 2006. **1**(1): p. 15-30.

105. Sodian, R., et al., *Early In vivo experience with tissue-engineered trileaflet heart valves.* Circulation, 2000. **102**(19 Suppl 3): p. III22-9.

106. Engelmayr, G.C., Jr., et al., *A novel bioreactor for the dynamic flexural stimulation of tissue engineered heart valve biomaterials.* Biomaterials, 2003. **24**(14): p. 2523-32.

107. Engelmayr, G.C., Jr., et al., *Cyclic flexure and laminar flow synergistically accelerate mesenchymal stem cell-mediated engineered tissue formation: Implications for engineered heart valve tissues.* Biomaterials, 2006. **27**(36): p. 6083-95.

108. Engelmayr, G.C., Jr., et al., *A novel flex-stretch-flow bioreactor for the study of engineered heart valve tissue mechanobiology.* Ann Biomed Eng, 2008. **36**(5): p. 700-12.

109. Ramaswamy, S., et al., *The role of organ level conditioning on the promotion of engineered heart valve tissue development in-vitro using mesenchymal stem cells.* Biomaterials, 2010. **31**(6): p. 1114-25.